Konrad Johannes Birkmeier

Time Resolved Microscopy of Exciton Dynamics in Nanoscopic Objects

2024

Dissertation zur Erlangung des Doktorgrades
der Fakultät für Chemie und Pharmazie
der Ludwig-Maximilians-Universität München

Time Resolved Microscopy of Exciton Dynamics in Nanoscopic Objects

Konrad Johannes Birkmeier
aus
Landshut, Deutschland

2024

Erklärung

Diese Dissertation wurde im Sinne von § 7 der Promotionsordnung vom 28. November 2011 von Herrn Prof. Dr. Achim Hartschuh betreut.

Eidesstattliche Versicherung

Diese Dissertation wurde eigenständig und ohne unerlaubte Hilfe erarbeitet.

München, 26.04.2024

Konrad Birkmeier

Dissertation eingereicht am	19.01.2024
1. Gutachter:	Prof. Dr. Achim Hartschuh
2. Gutachter:	Prof. Dr. Alexander Högele
Mündliche Prüfung am	19.04.2024

Blessed are they
who see beautiful things in humble places
where other people see nothing.

CAMILLE PISSARRO

Abstract

In the course of this work the initial excited state dynamics of single nanoobjects on the example of single-walled carbon nanotubes and transition metal dichalcogenides were studied. Whereas the common time resolved photoluminescence (PL) measurement comprises a unrivaled detection sensitivity it lacks of the temporal resolution necessary to reveal the initial decay dynamics on the sub-ps scale. In this work, this was achieved by the combination of the temporal resolution of a pump-probe scheme with the sensitivity of an interferometric scattering technique resulting in *transient interferometric scattering* (TiSCAT) microscopy. This technique is capable of measurements on single nanoobjects which are particularly challenging due to their low photostability, and thus, small applicable pump and probe fluences.
Two different pulsed laser systems where used in the scope of the measurements: The existing Ti:Sa setup utilized a supercontinuum generation to supply probe pulses over a broad spectral range but with a considerable amount of intensity noise. Therefore, for measurements with highest sensitivity, alignment stability and ease of use, a novel pulsed wavelength-tunable two-arm fiber laser system was developed acting as a low-noise excitation source. The continuous wavelength tunability of the laser system was achieved by the soliton self-frequency shift (SSFS) and enabled the measurement setup of the investigation of specific excited states.
Measurements on single (6,5) SWCNTs were carried out utilizing PL and TiSCAT microscopy revealing tube-to-tube variations of the decay dynamics attributed to variations in the environment or caused by defects. A model including the fast initial decay arising from exciton-exciton annihilation (EEA) and the slower intrinsic decay of the single excitons was applied to the data obtained from PL and TiSCAT measurements. The data sets could be described by the same model giving a unified picture of both measurement techniques for the first time. With this experimental approach it was possible to investigate EEA down to few excitons in the excited nanotube. EEA reaching time scales below 200 fs at highest densities was observed. The influence of the exciton density on the EEA process could be validated by theoretical calculations. Monte-Carlo simulations underlined the influence of spatial variations on the decay dynamics giving an explanation for the tube-to-tube variations observed. TiSCAT measurements on single-layer $MoSe_2$ were carried out revealing different signal contributions as photobleaching and photoinduced absorption. The measurements were used to determine the sensitivity of the system which was shown to be $\Delta I/I = 2.4 \cdot 10^{-6}$ which is on the order of the fundamental shot noise limit. Utilizing this high sensitivity, the absorption spectrum of a single (6,4) SWCNT was determined and compared to its emission spectrum.

Table of contents

Chapter 1

Introduction

Modern life is eminently influenced by all kinds of electronic devices - ranging from individual telecommunication electronics, energy storage in the field of e-mobility to energy harvesting in the sense of renewable energies. All application fields comprise their own demands in material performance and properties which often cannot be fulfilled by the commonly known elements like silicon - the material which has paved the way of today's electronics. Recent developments require more advanced kinds of components which cannot be built from the present state of research. Primary demands are an easy up-scaling of the production process[1], environmentally friendly and sustainable products[2], reduction of power consumption[3], an increase in the speed of the devices[4] or shrinking of the size of components, maintaining Moore's law[5].

Low dimensional materials that are limited to one or two dimensions in extent have drawn an increasing focus of research in the last years latest since the discovery of 2D-graphite which is better known as *graphene*. This discovery, which was awarded with the Nobel prize in physics in 2010[6], revealed a variety of unique physical properties of this material and led to the intensification of research in the field of low dimensional materials and their potential application fields. However, due to its semi-metal character graphene lacks of a direct bandgap which is fundamental for a variety of applications such as energy harvesting, flexible electronic devices and optoelectronics. This gap was filled by the material class of 2D *transition metal dichalcogenides* which can be fabricated in form of single-layers of molecular thin sheets similar to graphene. Promising candidates of this class are MoS_2 and $MoSe_2$ which exhibit a direct band gap when thinned down to single layer.

Strong confinement effects and a reduced shielding of electrical fields, which are typical for 1D and 2D materials, lead to the formation of strongly bound electron-hole pairs so called *excitons* with binding energies up to the eV-level.

The optoelectronic properties of transition metal dichalcogenides are mainly governed by the dynamics of excitons such as optical absorption and the lifetime of excited states.

Although lacking a band gap, graphene forms semiconducting nanoparticles when it is rolled up to seamless cylinders of nanometer thickness known as *single-walled carbon nanotubes* (SWCNTs). The physical properties, like conduction type, are unambiguously defined by the way the nanotubes are rolled up. The optoelectronic properties of the quasi-one dimensional SWCNTs are also guided by the formation and dynamics of excitons similarly to the material group of the transition metal dichalcogenides. Due to the confinement to two dimensions of which one exhibits cyclic boundary conditions, the absorption of the nanotubes is spectrally condensed to distinct narrow peaks. This makes them an interesting material class for optical devices like SWCNT-LEDs[7]. SWCNTs can be produced in a variety of different types depending on the way the graphene sheet can be thought to be rolled-up (the so called chirality) determining their optical properties, thus making them attractive for applications in electronics[8] or sensing[9, 10].

The proper selection of material components and their structural investigation is a key action in the research of novel materials and the creation of heterostructures in order to develop new devices. The knowledge of charge carrier dynamics on the nanoscale is an indispensable tool for the evaluation of the material properties and the influence of defects and spatial variations. Confocal microscopy has evolved to a powerful technique in this field of research. Its spatial resolution is limited by the diffraction of light on the order of half an optical wavelength.

A variety of different contrast mechanisms in confocal microscopy has evolved since its development containing linear and non-linear microscopy, like second harmonic generation (SHG)[11] and third harmonic generation (THG)[12], photoluminescence (PL)[13], stimulated Raman scattering (SRS)[14], transient absorption (TA)[15] and a lot more.

Microscopy on small single nanoparticles like SWCNTs is particularly challenging as their scattering cross section is extremely small, thus, highly challenging to distinguish from the measurement background. Additionally, the possible excitation power levels are limited to several µW as the nanotubes show photodegradation at higher powers. For this reason, very sensitive and background free measurement techniques like PL microscopy are commonly used to image single nanoobjects. There emission down to the single photon level can be detected. For time-resolved investigation of the PL decay dynamics *time correlated single photon counting* (TCSPC) is the most common technique. However, its temporal resolution is limited to several tens

of picoseconds for typical photo-detectors, making dynamics right after the initial excitation process invisible.
Pump-probe techniques, on the other hand, comprise a temporal resolution which is mainly limited by the temporal pulse width of the utilized laser source, and thus it can easily resolve dynamics happening in the range of sub-100 fs after excitation[16]. Generally, it exhibits a comparatively low sensitivity because it observes relative changes and is not background free. This restricts its usage to enriched sample materials and impedes the measurement on single nanoparticles.
Despite being challenging, the scattering microscopy of single nanoobjects like individual single-walled carbon nanotubes can be realized by exploiting the interference of the scattered light and the dominating contribution of the reflected light on the substrate. This technique called *interferometric scattering microscopy* (iSCAT) was already proven to be capable of resolving single particles like viruses[17], gold nanoparticles [18] or SWCNTs[19].
In this work the iSCAT technique is combined with a pump-probe scheme to achieve a high sensitivity due to the interferometric detection on the one hand and a temporal resolution capable of resolving the initial decay mechanisms due to the pulsed laser system on the other hand. In the following, this microscopy technique is denoted as *transient interferometric scattering* (TiSCAT) microscopy.
The aim of this thesis is the utilization of this detection scheme to investigate the temporal dynamics of excited states in single low dimensional nanoobjects like semiconducting single-walled nanotubes and transition metal dichalcogenides.

The experimental part of the work is split into two distinct sections:

- For the realization of the pump-probe scheme a laser system with precisely tailored features was developed. This was done in cooperation with the company *TOPTICA photonics AG* where the two-arm fiber laser based system was constructed. It comprises all necessary components for the microscopy setup, thus ensuring the beam parameters and stability needed for the measurement.

- Following the fiber laser source development, the TiSCAT microscope was used for the investigation of the single nanoparticles and their decay mechanisms. The more detailed description of the individual experiments is given on the next page where a short overview of the thesis structure is provided.

The thesis is structured as follows:

Starting with **chapter 2** the physical background of the investigated materials like single-walled carbon nanotubes and transition metal dichalcogenides is elucidated. For the evaluation of the time-resolved measurements the influences on decay dynamics are shown paying special attention to excitonic states.

In **chapter 3** the principles of both utilized time-resolved measurements (time-correlated single photon counting and transient interferometric scattering) are introduced. The details of the experimental microscopy setup are shown in the following section. In the last section the sample preparation used for individualization of single nanoobjects on microscopy glass cover slides is explained.

The development of the two-arm fiber laser system is shown in **chapter 4**. In the beginning, a theoretical overview of the optical effects is given which were utilized to reach the desired pulse characteristics. The assembled laser system is then introduced and the most important measurements characterising the performance of the light source are presented.

In **chapter 5** the time-resolved measurements performed on single (6,5) SWCNTs are presented. It is demonstrated that both PL and TiSCAT microscopy are capable of detecting single nanotubes. A model is introduced which unifies the excited state dynamics in both measurements including the fast initial decay. Finally, Monte-Carlo simulations are utilized to investigate the origin of tube-to-tube variations.

Spectrally resolved TiSCAT measurements of excitonic states in single-layer $MoSe_2$ are shown in **chapter 6** revealing different signal contributions which are then further classified. The photostability and uniformity of the material is used to estimate the sensitivity of the TiSCAT system.

In **chapter 7** TiSCAT measurements on single (6,4) SWCNTs are presented. The first transient absorption spectra of a single nanotube measured via TiSCAT is compared to the PL spectrum and the differences between both are elucidated.

Chapter 2

Physical properties of studied materials

1 Single-walled carbon nanotubes

The first experimental observation of carbon nanotubes (CNTs) is often attributed to Sumio Iijima who found the novel nanoscale structures in 1991 by electron microscopy. The investigation of carbon electrodes after carrying out an electric arc discharge revealed a variety of tubules with several nanometers in diameter and up to micrometer length[20]. Since this finding the synthesis of specific types of carbon nanotubes has evolved to different techniques like chemical vapour deposition (CVD)[21, 22] or laser ablation[23] also yielding higher amounts of the material.
The quasi one dimensional structure of SWCNTs leads to a variety of mechanical, electrical and optical properties which will be explained theoretically in the following chapter. At first the structural characteristics will be shown and how they are determined by the tube chirality.

1.1 Representation in real space and reciprocal space

Single-walled carbon nanotubes can be described as a rectangular sheet of a single-layer graphene which is rolled up in form of a seamless hollow cylinder. Graphene consists of a monolayer of carbon atoms arranged in a hexagonal honeycomb lattice like shown in figure 2.1a. The real space unit cell contains two carbon atoms (marked in black and white in the figure) each being part of a triangular sublattice spanned by the basis vectors $\vec{a}_1$ and $\vec{a}_2$ exhibiting an angle of 60°.

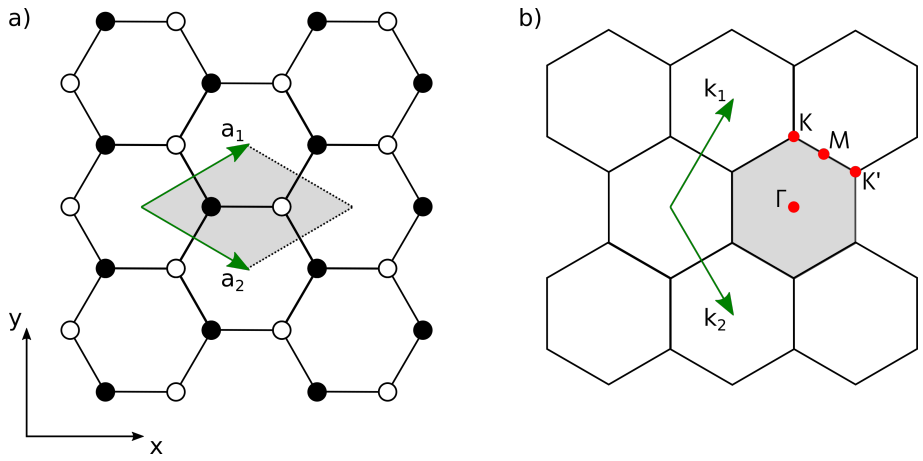

Figure 2.1: a) The lattice of a single sheet of graphene in real space. b) The corresponding Brillouin zone (shaded grey) in reciprocal space. Points of high symmetry are labelled Γ, M, K and K′.

These vectors can be written in Cartesian coordinates (x-y-axis in the figure) in the form

$$\vec{a}_1 = \left(\frac{\sqrt{3}}{2}, \frac{1}{2}\right) \cdot a_0, \qquad \vec{a}_2 = \left(\frac{\sqrt{3}}{2}, -\frac{1}{2}\right) \cdot a_0, \tag{2.1}$$

where a_0 denotes the length of the vectors and is determined by the bonding length of the carbon atoms a_{C-C} in the form $|\vec{a}_1| = |\vec{a}_2| = a_0 = \sqrt{3} \cdot a_{C-C} = 2.461\,\text{Å}$[24].

Structure of SWCNTs Carbon nanotubes of different types and diameters can be constructed by rolling up a single sheet of graphene along a certain axis as shown in figure 2.2. The vector determining the superimposing carbon atoms for different possibilities of rolling a SWCNT is represented in the figure in form of black arrows. This vector is called *chiral vector* $\vec{C}$ and can be written in the basis of the unit cell vectors $\vec{a}_1$ and $\vec{a}_2$ of graphene:

$$\vec{C} = n \cdot \vec{a}_1 + m \cdot \vec{a}_2, \qquad n, m \in \mathbb{N}, n > m. \tag{2.2}$$

The tuple (n,m) is known as the *chiral index* and is the most important property to distinguish the structure of SWCNTs and to group them by their properties. With this the carbon nanotubes can be divided into three subgroups called zigzag (m=0), armchair (n=m) and chiral ($n \neq m$). This naming can be easily understood by taking into account the characteristic pattern of the carbon bonds located along

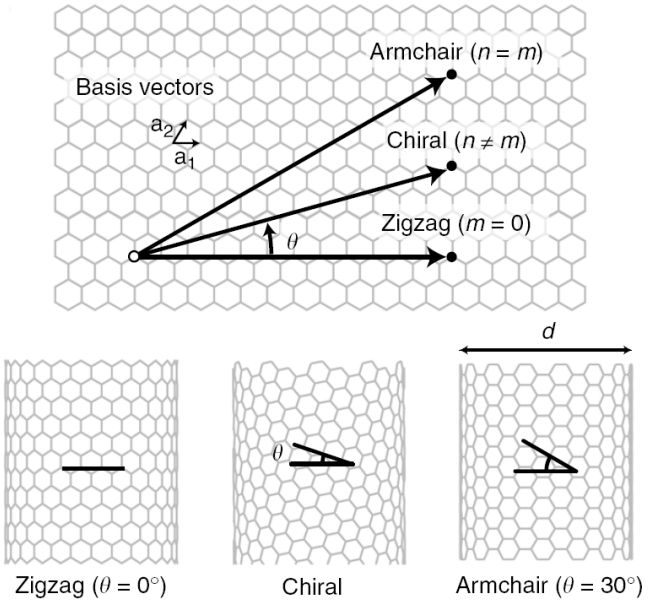

Figure 2.2: Different types of carbon nanotubes rolled from a single sheet of graphene. The three possible categories of SWCNTs are shown (zigzag, chiral and armchair) determined by the chiral vector $\vec{C}$. The chiral angle is depicted as Θ. Modified from [25] under creative commons license CC BY 4.0 (`http://creativecommons.org/licenses/by/4.0/`).

the chiral vector $\vec{C}$. This classification allows for the prediction of the electronic properties of SWCNTs as will be shown in detail in section 2.1.2.
The diameter d of a SWCNT can be calculated from the length of the chiral vector $\vec{C}$ (circumference of the nanotube) as

$$d = \frac{|\vec{C}|}{\pi} = a_0 \frac{\sqrt{n^2 + mn + m^2}}{\pi}. \tag{2.3}$$

For the (6,4) and (6,5) SWCNTs investigated in this thesis this leads to diameters of 6.83 Å and 7.47 Å, respectively.
The translational period vector $\vec{T}$ along the tube axis is determined by the chiral index in form of the equation

$$\vec{T} = \frac{2m + n}{d_r} \cdot \vec{a}_1 - \frac{2n + m}{d_r} \cdot \vec{a}_2. \tag{2.4}$$

This is the unit cell vector of the SWCNT along the z-axis. The factor d_r represents the greatest common divisor of $(2m + n)$ and $(2n + m)$. By the length of $\vec{T}$ the shortest distance between two equivalent carbon atoms can be derived:

$$|\vec{T}| = \frac{\sqrt{3} \cdot |\vec{C}|}{d_r}. \tag{2.5}$$

Since the chiral vector $\vec{C}$ and the translational vector $\vec{T}$ form a rectangle the area of the folded graphene sheet can be derived as $|\vec{C}| \cdot |\vec{T}|$. Dividing this by the area of a single unit cell of graphene one obtains the number of graphene unit cells N_{UC} in the unit cell of a SWCNT:

$$N_{\mathrm{UC}} = \frac{2(n^2 + nm + m^2)}{d_r}. \tag{2.6}$$

In every unit cell there are two carbon atoms so the number of atoms per unit cell of the carbon nanotube is given by

$$N_{\mathrm{C}} = \frac{4(n^2 + nm + m^2)}{d_r}. \tag{2.7}$$

This number can differ strongly for nanotubes of comparable diameter: As earlier shown the two types of SWCNTs studied in this work ((6,5) and (6,4)) exhibit similar diameter but the number of carbon atoms per unit cell differs by more than a factor of two (364 atoms for (6,5) and 152 atoms for (6,4), respectively).
Transferring the real space lattice of graphene into the reciprocal space one obtains the first *Brillouin zone* (BZ) spanned by the vectors $\vec{k}_1$ and $\vec{k}_2$ in Cartesian coordinates (see Fig. 2.1b):

$$\vec{k}_1 = \frac{2\pi}{a_0}\left(\frac{1}{\sqrt{3}}, 1\right), \qquad \vec{k}_2 = \frac{2\pi}{a_0}\left(\frac{1}{\sqrt{3}}, -1\right). \tag{2.8}$$

As previously shown for the real space representation this is adapted and modified for the description of the reciprocal lattice of SWCNTs as explained below.
For the reciprocal vectors $\vec{k}_1$ and $\vec{k}_2$ following expressions are derived from the orthonormality condition of the transformation from the real space into the reciprocal space: $\vec{k}_i \cdot \vec{a}_j = 2\pi\delta_{ij}$. This leads to conditions for the reciprocal vectors $\vec{k}_\perp$ and $\vec{k}_\parallel$ perpendicular and parallel to the tube axis:

$$\begin{aligned} \vec{k}_\parallel \cdot \vec{C} &= 0, & \vec{k}_\parallel \cdot \vec{T} &= 2\pi, \\ \vec{k}_\perp \cdot \vec{C} &= 2\pi, & \vec{k}_\perp \cdot \vec{T} &= 0. \end{aligned} \tag{2.9}$$

The length of $\vec{k}_\parallel$ is determined by the inverse of the length of the translational vector $\vec{T}$:

$$|\vec{k}_\parallel| = \frac{2\pi}{|\vec{T}|}. \tag{2.10}$$

As the carbon nanotube is regarded as infinitely long the wave vector $\vec{k}_\parallel$ may cover continuous values within the interval $[-\pi/|\vec{T}|, +\pi/|\vec{T}|]$.

In contrast to the BZ of graphene the wave vector along the circumference of SWCNTs is quantized. This is due to the boundary conditions which arise from the constraint that the length of the wave vector has to be a multiple of the circumference in order to fulfil constructive interference by a phase shift of an integer multiple of 2π:

$$\mu \cdot \lambda = |\vec{C}| = \pi \cdot d \qquad \Leftrightarrow \qquad |\vec{k}_\perp| = \frac{2\pi}{\lambda} = \frac{2\pi}{|\vec{C}|} \cdot \mu = \frac{2}{d} \cdot \mu. \tag{2.11}$$

Here λ denotes the wavelength of the wave vector perpendicular to the nanotube axis and μ can take integer values $-N_{\mathrm{UC}}/2 + 1, ..., -1, 0, 1, ..., N_{\mathrm{UC}}/2$. All other wave vectors will vanish due to destructive interference. This constraint leads to a first Brillouin zone consisting of N_{UC} equidistant parallel lines of length $2\pi/|\vec{T}|$ (see Eq. 2.10) and gap spacing of $2\pi/|\vec{C}|$.
Finally, the first Brillouin zone of a SWCNT can be expressed by $\vec{k}_\parallel$ and the quantized vector $\mu \cdot \vec{k}_\perp$ perpendicular to it as

$$\vec{k} = \vec{k}_\parallel + \mu \cdot \vec{k}_\perp. \tag{2.12}$$

The vector components can be derived from the orthonormality conditions given in Eqs. 2.9 and are represented by the reciprocal lattice vectors of graphene as follows:

$$\vec{k}_\parallel = \frac{1}{N_{\mathrm{UC}}} \left(m\vec{k}_1 - n\vec{k}_2 \right), \tag{2.13}$$

and

$$\vec{k}_\perp = \frac{1}{N_{\mathrm{UC}}} \left(\frac{2n+m}{d_r}\vec{k}_1 + \frac{2m+n}{d_r}\vec{k}_2 \right). \tag{2.14}$$

As stated before, the number of parallel lines forming the first BZ of a SWCNT is determined by the number of hexagons in the real space unit cell which can be calculated according to Eq. 2.6. For example, in a (6,4) SWCNT there are 76 lines in the first BZ. The location of the reciprocal vectors $\vec{k}_\parallel$ and $\vec{k}_\perp$ and their cutting points with the reciprocal lattice of graphene have significant influence on the electronic properties of SWCNTs as will be shown in the following section.

1.2 Electronic properties

The electronic properties of single-walled carbon nanotubes can be derived taking the electronic properties of graphene as the starting point. The most common way is the so called *zone folding approach* where the Brillouin zone of graphene is cut by the first Brillouin zone of the SWCNT which is represented by parallel lines as

shown in the previous section. The emerging lines form the allowed electronic band structure of the nanotube. This technique gives qualitatively accurate results though it does not take into account deviations caused by curvature effects[26]. However, fundamental effects occurring in SWCNTs can be well understood in this picture.
In graphite the $2s$, $2p_x$ and $2p_y$ orbitals hybridize to three sp^2 orbitals forming the covalent σ bonds between the carbon atoms which are located in-plane and are spread in angles of 120°. The remaining p_z orbital is located perpendicular to this surface forming bonding and antibonding π orbitals resulting in the valence band and the conduction band, respectively. The cohesive properties like elasticity of the graphene sheets are mainly governed by the strong in-plane σ bonds whereas the electronic properties are determined by the π bonds[27]. Although comparatively strong, the energy bands of the σ bonds are too far away from the Fermi level ($\pm$ 4 eV)[27] in order to play a significant role in transport effects[24].

Tight binding model of graphene In order to derive the electronic dispersion relation of graphene the *tight-binding approach* is chosen[28]. The p_z electrons can be treated independently of the other valence electrons due to the vanishing overlap of the electronic wave functions of the σ bonds and the π bonds.
To derive the electronic band structure of graphene the Schrödinger equation has to be solved for the present system:

$$H\Psi(\vec{k}) = E(\vec{k})\Psi(\vec{k}). \tag{2.15}$$

Here H describes the Hamiltonian of the system, E the eigenvalues at wave vector $\vec{k}$ and $\Psi(\vec{k})$ the eigenfunctions. These can be written as a linear combination of periodic Bloch functions $\Phi_l(\vec{k})$ in the form

$$\Psi(\vec{k}) = \sum_l C_l \Phi_l(\vec{k}). \tag{2.16}$$

In the tight-binding approximation the Bloch functions are represented as the periodic linear combination of the atomic wave functions of the two carbon atoms of every unit cell. These can be written for the sublattice A in the form

$$\Phi_{\mathrm{A}} = \frac{1}{\sqrt{N}} \sum_{\vec{R}_{\mathrm{A}}} e^{i\vec{k}\vec{R}_{\mathrm{A}}} \psi(\vec{r} - \vec{R}_{\mathrm{A}}), \tag{2.17}$$

and for the sublattice B in an equivalent way[24]. Here N denotes the number of unit cells in the material, $\vec{R}_{\mathrm{A}}$ the lattice vector and ψ the normalized p_z orbital of an isolated atom.

The further derivation of the electronic dispersion relation can be found in detail in refs. [24, 28, 26, 27] and leads to:

$$E(\vec{k}) = \frac{\epsilon_{2p} \pm t \cdot w(\vec{k})}{1 \pm s \cdot w(\vec{k})}. \tag{2.18}$$

Here the plus and minus sign correspond to the π band and the π^* band, respectively. The function $w(\vec{k})$ can be written as

$$w(\vec{k}) = \sqrt{1 + 4\cos\left(\frac{\sqrt{3}k_x a_0}{2}\right)\cos\left(\frac{k_y a_0}{2}\right) + 4\cos^2\left(\frac{k_y a_0}{2}\right)}. \tag{2.19}$$

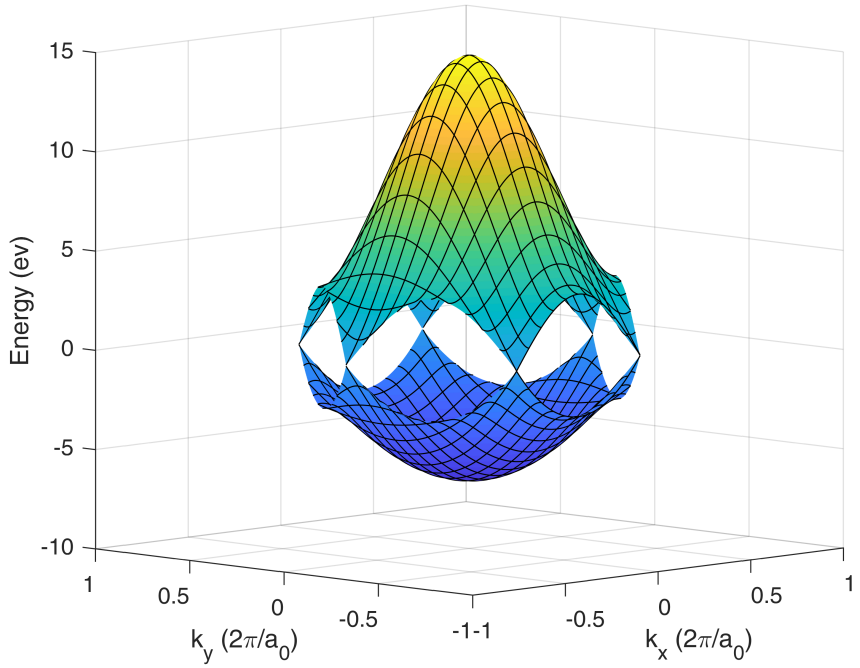

Figure 2.3: Dispersion relation of graphene calculated using Eqs. 2.18 and 2.19.

Here often used parameters are $\epsilon_{2p} = 0$, $t = -3.033$ eV and $s = 0.129$ derived from first principles calculations[26]. In Fig. 2.3 the dispersion relation of graphene is shown for the first Brillouin zone. The upper part displays the antibonding π^* band (conduction band) and the lower part the bonding π band (valence band). The valence band is completely filled up to the Fermi energy E_F and touches the conduction band at the K and K′ points. Graphene is classified as a zero-gap semiconductor[26] due to a vanishing density of states at the Fermi energy. However, a band gap opening has been experimentally shown by implanting hydrogen atoms at the positions of a Moiré superlattice pattern in a graphene sheet[29].

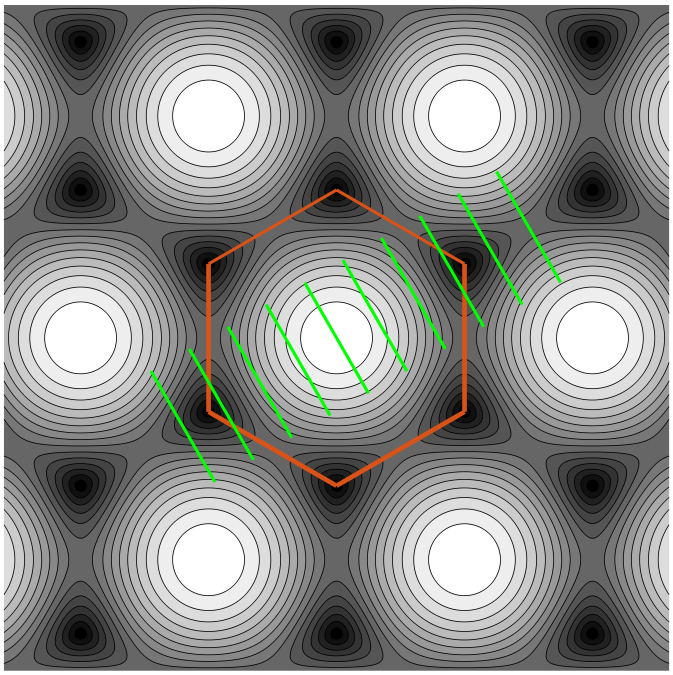

Figure 2.4: Brillouin zone of a (5,0)-SWCNT (shown in green) projected onto the contour plot of the dispersion relation of graphene. The first BZ of graphene is depicted in orange.

The zone folding approach can be applied to the obtained dispersion relation of graphene which is illustrated in Fig. 2.4. Here the first Brillouin zone of a (5,0) SWCNT is projected onto the contour plot of the dispersion relation of graphene. This chirality was chosen in the example due to its simplicity as it consists only of ten separate lines.

The band structure of the SWCNT emerges from the cutting lines of the dispersion relation of graphene and the first BZ of the nanotube. This is depicted schematically in Figure 2.5 for two different positions of the cutting surface. The zone folding approach is shown for a zoom-in to the dispersion relation at the position where conduction band and valence band of graphene touch each other at the K and K′ points. In this area the dispersion relation exhibits a linear behaviour resulting in the so called *Dirac cones*. The charge carriers can be described as massless Fermions[30] at this point which results in the high mobility of graphene. The cutting lines determined by the chirality of the SWCNT are shown as turquoise surfaces cutting through the Dirac cones. The emerging line shape of the band structure is depicted at the bottom position of the figure. If one line of the first BZ of the SWCNT is cutting through the touching point of the Dirac cone the conduction band of the SWCNT is connected to the valence band. This results in metallic properties of the

nanotube (see Fig. 2.5 left side). The SWCNT is semiconducting if both resulting bands are not connected as shown on the right side of Fig. 2.5.

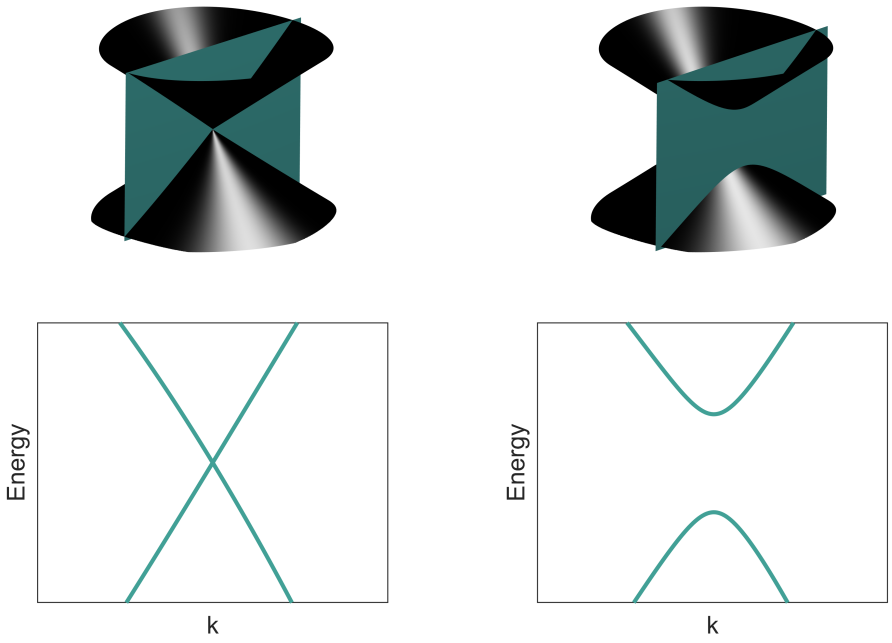

Figure 2.5: Illustration of the zone folding approach used for the calculation of the energy band scheme of SWCNTs. The Dirac cone of graphene is depicted in black which is cut by the lines of the first BZ of the SWCNT shown in turquoise. The emerging bands are shown in the bottom plots. Right: metallic SWCNT, left: semiconducting SWCNT.

This illustrates that electronic properties of SWCNTs are predominantly determined by their corresponding chirality (n,m). The general rule for the metallicity of the tube is given by the difference of the values of n and m: The SWCNT is of metallic character if their difference value is a multiple of 3 ($(n-m) \bmod 3 = 0$) as the first Brillouin zone cuts the graphene Dirac cone in the touching point of its bands. All other cases are semiconducting with a direct band gap[27].

Density of states

A fundamental property for the optical transition processes is the so called *density of states* (DOS). It specifies the number of allowed states which can be occupied in a certain energy interval $[E, E + \Delta E]$.

For the one-dimensional case of a SWCNT it is given by[31]:

$$\mathrm{n(E)} = \frac{\partial N(E)}{\partial E} = \frac{2}{l} \sum_i \int dk\, \delta(k - k_i) \left| \frac{\partial \epsilon}{\partial k} \right|^{-1} . \tag{2.20}$$

Here $l = \int dk$ denotes the length of the BZ, k_i the roots of the equation $E - \epsilon(k_i) = 0$. $N(E)$ represents the total number of electron states below a given energy E. From equation 2.20 it becomes apparent that the density of states exhibits singularities for points of local extrema $\frac{dE}{dk} = 0$. This leads to sharp features in the DOS which are typical for low dimensional materials. In 2D the DOS shows a step like behaviour at the bottom position of subbands whereas the step height remains constant[32]. For the one dimensional case of a SWCNT the DOS exhibits a diverging value at the minima of the energy bands[33]. In Fig. 2.6 a numerical simulation of the band structure of a (6,4) SWCNT is depicted for the first BZ on the left side and the corresponding density of states on the right side. The calculation was performed with the simulation software *CNTbands*[34]. The BZ of the nanotube does not cut the Dirac cone of graphene at the K point which leads to a semiconducting behaviour, and thus to a vanishing density of states between the first two singularities which define the band gap. The points of diverging density of states in one dimension are also called *van-Hove-singularities* (vHs). They strongly influence the absorption and emission properties of the SWCNTs as their transition probability is dependent on the number of states which can be occupied for a certain energy[32].

In 1999 Kataura et al. presented a theoretical study about the dependence of the tube diameter on the energy difference of the vHs of the same subband indices (E_{ii}, see Fig. 2.6) in the conduction and valence band based on the tight-binding model of graphene[35]. A dependence of $E \sim 1/d$ can be found for all semiconducting SWCNTs independent on chirality but with a family pattern splitting the tubes into two groups[26, 31].

In the following, a short discussion of the transition probabilities is given. The transition between different energy bands requires the conservation of momentum. As a photon exhibits a negligible value of momentum only vertical transitions are allowed ($\Delta k \approx 0$).

Interband transition probabilities in single-walled carbon nanotubes strongly depend on the subband index of the corresponding valence and conduction band (see right image of Fig. 2.6). For the conservation of angular momentum the corresponding quantum number remains constant for excitation of light polarized parallel to the tube axis z: $\Delta m = 0$ for $E \parallel z$. This is realized by transitions between van-Hove singularities of the same index i: $E_{11}, E_{22}, ...$ These are depicted as red arrows in Fig. 2.6.

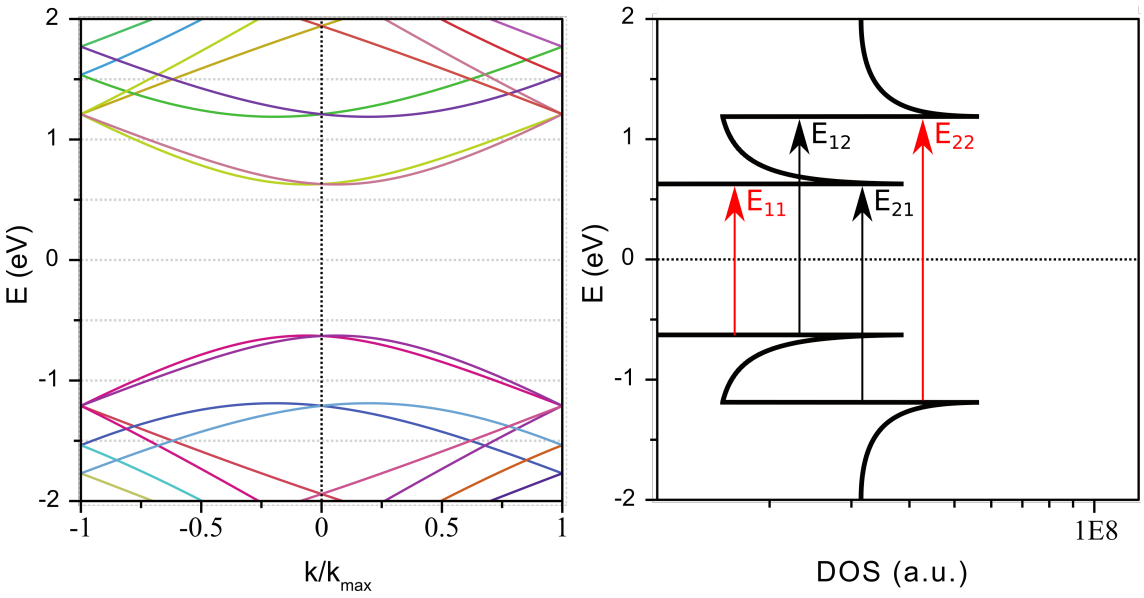

Figure 2.6: Calculated bandstructure and density of states (DOS) of an (6,4) SWCNT. Calculations were performed with the simulation software *CNT-bands*[34]. The red arrows indicate possible optical transitions whereas black arrows show strongly suppressed transitions.

Transitions between different indices of the vHs (see black arrows in Fig. 2.6) require the change of the angular momentum number; thus, a light polarization perpendicular to the tube axis z is necessary in this case: $\Delta m = \pm 1$ for $E \perp z$[24]. Although allowed by the selection rules, absorption perpendicular to the tube axis is strongly suppressed due to the induced charges in the cylinder walls. These produce a counteracting polarisation which nearly prevents any absorption[36, 37].

1.3 Excitonic states

The simple single particle picture of carrier excitation as assumed in the previous section is a good estimation for the case of semiconducting (bulk) materials. Here the high relative permittivity ϵ_r, giving the ratio of electric field strength in a material compared to vacuum condition, leads to a strong shielding of Coulomb interactions between charge carriers also called *dielectric screening*. This shielding is strongly decreased in the case of low-dimensional materials like SWCNTs. Here the electrical field lines generated by the separation of an electron from its positively charged origin (denoted as *hole*) are predominantly located outside the wall of the nanotube where the relative permittivity is small. Furthermore, due to the low-dimensionality of the SWCNT the probability for having an electron and a hole in a certain distance is greatly enhanced[38]. The many-body effects facilitated by the reduced screening

leads to two effects influencing the transition energies: Firstly, the repulsive interaction of free electrons leads to an increase of the band gap energy known as *band gap renormalization* (BGR) shifting the absorption to the blue. Secondly, the attractive force between the electrons and their corresponding holes establishes the formation of bound electron-hole-pairs called *excitons* shifting the absorption to the red as it is decreased by the binding energy of the quasi-particles E_{exc}[39].
In common semiconductor bulk materials excitons can be observed as well. Their binding energies in the order of several meV limit the detection of the energy deviation from the single-particle band gap to low temperature experiments. In contrast, the binding energy of excitons in SWCNT can reach values in the eV-range. Thus, they are measurable even at room temperature[40]. Excitons can be treated as hydrogen-like particles exhibiting a series of energy levels which can be occupied.
There were several experimental reports which gave an indication for the quasi-particle nature of excited states in SWCNTs. The formation of excitons was shown experimentally for example by two-photon excitation where a shift of the absorption to higher energies (higher lying excited states of the exciton) was observed[38]. This shift with respect to the one-photon absorption can be explained by symmetry selection rules which forbid the transition to the lowest bright state of the exciton[41]. Another experimental hint was the so called *ratio problem* where the radiative recombination (*photoluminescence*, PL) of SWCNTs was investigated. The ratio E_{22}/E_{11} of two distinct states was measured differing from theoretical predictions in the single-particle model suggesting the influence of many-body effects[42].

1.4 Excitation and recombination of excitons

Considering optical transitions from the valence band to an excited state of an exciton, these are only possible in vertical direction as the absorbed photon has negligible amount of momentum ($k_C = k_V$) as shown in Fig. 2.7a. Here k_C and k_V denote the wave vector of the excited electron in the conduction band and the wave vector of the remaining hole in the valence band, respectively. The wave vector of the center of mass of the quasi-particle is given by $K = (k_C - k_V)/2$. The exciton energy dispersion is governed by K determining the translational motion of the particle. Therefore, only excitons with vanishing K value can recombine by emission of a photon. Thus, states with $K \neq 0$ are forbidden in radiative recombination and remain as so called *dark excitons*[40]. However, recombination of these states is possible though phonon-assisted processes as will be shown below.
By the absorption of a photon an electron with a certain spin (for example spin-up "↑" as depicted in Fig. 2.7b) is promoted to a higher lying state.

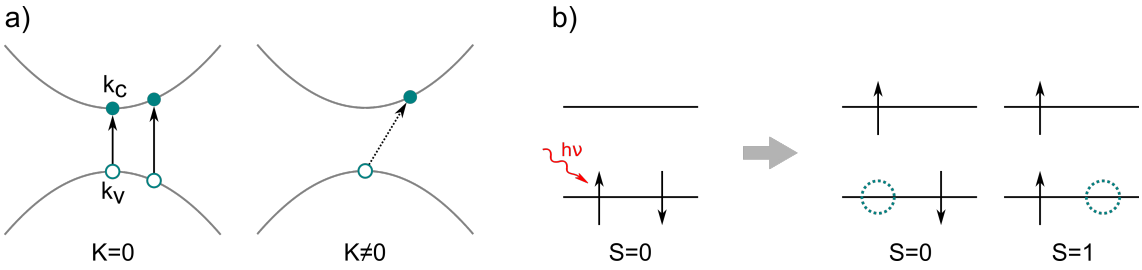

Figure 2.7: a) Excitation schemes with ($K \neq 0$) and without momentum transfer ($K = 0$). b) Formation of a singlet ($S = 0$) and a triplet exciton ($S = 1$). Adapted from [40].

A positively charged hole is left behind (depicted as petrol circle in the figure). The created exciton is a singlet exciton with total spin quantum number $S = 0$ as the corresponding dipole transition does not change the ground state spin with $S = 0$. The overall spin is determined by the sum of the spins of the two involved electrons each carrying $S = \pm 1/2$. In contrast, a triplet exciton is formed by an excited electron of same spin as the electron in the ground state yielding a total spin of $S = 1$[40]. Such a particle cannot recombine to the ground state via emission of a photon due to the Pauli exclusion principle which forbids identical fermions to be in the same quantum state simultaneously. However, PL emission originating from this dark triplet state has been reported for example by Matsunaga et al. for SWCNTs of different chiralities. They attributed the brightening of the exciton to a spin-flip process guided by defects[43].

After excitation into a higher lying state, the exciton relaxes very fast (in the order of tens of fs) into the lowest excitonic state and can recombine by emission of a photon[44]. The PL emission originates purely from the lowest excited bright state which is in accordance to Kasha's rule for molecules where an intra-subband relaxation happens prior to the transition to the ground state[45].

The *quantum yield* (QY) is defined as the ratio of the number of emitted photons with respect to the number of absorbed photons. For SWCNTs this is rather low in the order of 10^{-3} up to several percent depending on environmental conditions and production methods[46, 47, 48]. This is partially attributed to dark states that have a slightly smaller energy level than the bright state and do not contribute to PL intensity though contributing in form of a non-radiating decay channel[49].

Also other, non-radiative, decay channels have been proposed which contribute to recombination of the excitons whose overall lifetime τ can be described by the single

decay rates k_n of the different decay mechanisms (radiative k_r and non-radiative k_{nr}) as

$$\tau = \frac{1}{k_r + k_{nr}}. \tag{2.21}$$

Several studies of the lifetimes τ of excitonic states in SWCNTs have been reported which show a variety of different values between several ps, tens of ps or even over 100 ps suggesting different possible pathways for the decay and recombination of the particles[50, 51, 52].
In the following, some of the proposed decay mechanisms will be explained in detail:

- **Förster resonance energy transfer:** Bundling of SWCNTs due to strong van der Waals forces plays an important role in investigation of the nanotubes. This was historically a big issue and finally led to the development of a variety of separation techniques. In fact, the discovery of photoluminescence of semiconducting SWCNTs was not reported until 2002 when O'Connell et al. separated the single SWCNTs by micelle-encapsulation[47]. Since that discovery several other separation techniques have been shown like DNA-wrapping[53] or CVD-growth[54]. The agglomeration of nanotubes and the resulting small distances between them leads to efficient *Förster resonance energy transfer* (FRET) where an excited donor transfers energy of its excited state to a lower lying state of a nearby acceptor giving a non-radiative decay pathway[55].

- **Defects:** Localized defects along the SWCNT can act as trap states leading to variations in the excitonic energy landscape of the tube and modifications in the decay rate[56, 57]. This influence will be investigated in more detail in the experimental part in chapter 5.

- **Phonon assisted decay:** Perebeinos and Avouris have suggested two different decay mechanisms they named *multiphonon decay* (MPD) and *phonon-assisted indirect exciton ionization* (PAIEI) taking into account phonons contributing to the decay mechanisms[58, 59]. In MPD an exciton can decay when its energy matches a multiple of a phonon resonance energy. It recombines under creation of a corresponding number of phonons. For the bright exciton the momenta of the created phonons need to add up to zero[58]. This mechanism is depicted in Fig. 2.8a.

  PAIEI on the other hand is a process occurring in p-doped carbon nanotubes which is attributed due to the environmental conditions of the SWCNTs in air. The SWCNTs adsorb oxygen atoms which leads to p-doping and thereby to

vacancies in the conduction band[60]. In this process, an exciton decays under emission of a phonon to the ground state as depicted in Fig. 2.8b. To account for conservation of energy and momentum an additional electron-hole pair is created in the valence band. This is only possible for a p-doped SWCNT as the valence band has to be partially unfilled. The effect probability increases for stronger p-doping.

- **End quenching:** Due to the high mobility of excitons in SWCNTs quenching at the end points plays an important role in recombination of the quasi-particles. Hertel et al. have shown a strong increase of the quantum yield and the exciton PL lifetime for increasing length of SWCNTs suggesting the non-radiative quenching of excitons at tube ends to be a significant decay mechanism[61].

Exciton-exciton annihilation

Until this point no interactions between excitons were assumed. However, these play an important role in the dynamics investigated by pump-probe experiments where a high number of mobile excitons is excited in a short time interval and contained in the small focus volume. The excitons are limited to the one-dimensional motion most likely leading to a scattering event of two of the quasi-particles. As consequence, one of the excitons can be promoted to a higher lying state whereas the other exciton rapidly recombines under conservation of energy and momentum. This particular scattering event is called *Auger recombination* whereas the general effect of recombination due to scattering of excitons is named *exciton-exciton annihilation* (EEA)[62, 63]. This decay mechanism happens on a time scale of the order of hundreds of femtoseconds up to several picoseconds after excitation depending on the initial exciton density[62, 64]; and thus, it is not directly accessible via time resolved PL experiments as TCSPC.
Srivastava and Kono have worked out a theoretical model which combines the dynamics of the fast process of EEA and the slower decay of the single excitons[65]. The individual decay mechanisms can be written as

$$\begin{aligned} A + A &\rightarrow kA, \text{ with } k = 0, 1, \\ A &\xrightarrow{k_r} \text{photon}. \end{aligned} \tag{2.22}$$

Here A denotes excitons which can whether decay via complete EEA ($k = 0$), partial EEA (k=1) or radiative recombination with the decay rate k_r.

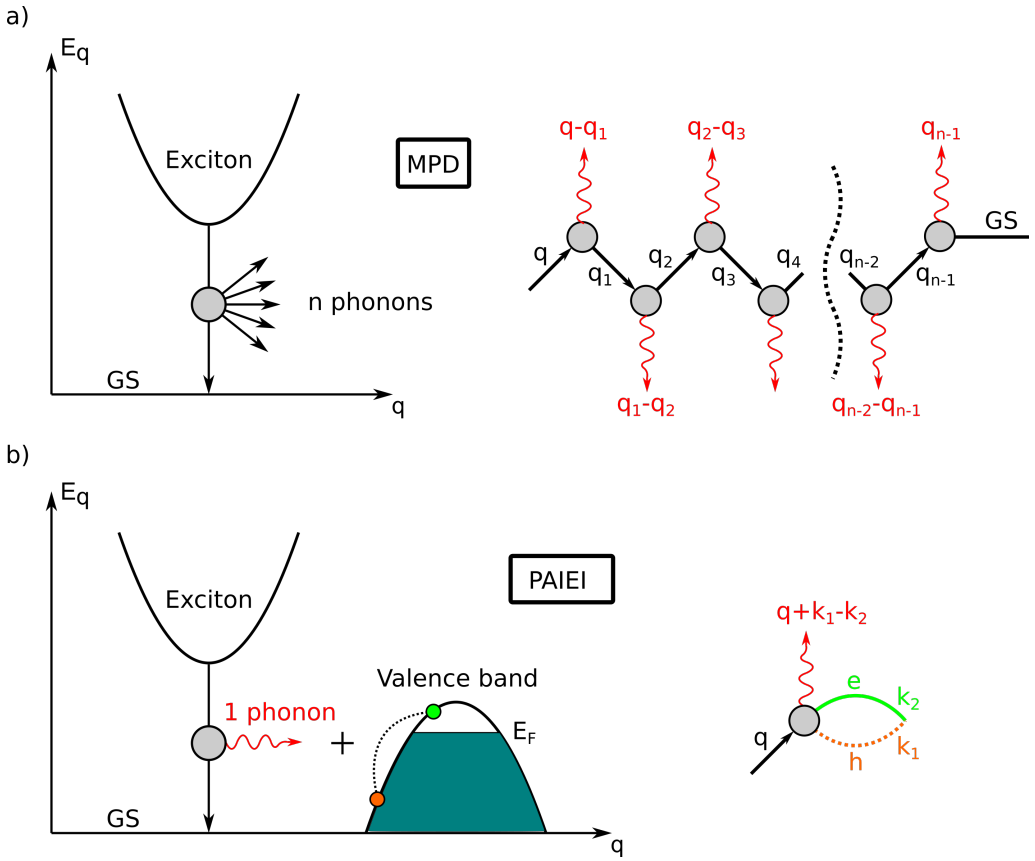

Figure 2.8: a) Exciton decay via multiphonon decay (MPD). The quasiparticle decays under emission of several phonons. b) Exciton decay via phonon-assisted indirect exciton ionization (PAIEI). The exciton recombines via emission of a phonon and a simultaneous splitting of an electron-hole pair in the valence band. Adapted from [58].

Assuming a Brownian motion of particles in one dimension they derived the following term for the fraction of excitons still alive after the time t in the case of complete EEA[65]:

$$n_A(t) = \frac{\exp(-\gamma t)}{1-\nu}\left[\exp\left(\frac{1-\nu}{\nu}\gamma t\right)\operatorname{erfc}\left(\sqrt{\gamma t/\nu}\right) + \sqrt{\nu}\operatorname{erf}(\sqrt{\gamma t}) - \nu\right]. \qquad (2.23)$$

Here γ denotes the sum of the radiative and non-radiative decay rates and $\nu = \tau_D/\tau_{\text{exp}}$ the ratio of the diffusional time τ_D and the exponential lifetime τ_{exp}. Equation 2.23 is restricted to values of $\nu << 1$ which is fulfilled for the experimental data reported in this work showing much longer exponential lifetimes than EEA dependent decay times. The diffusional time can be calculated from the initial mean distance d_0 and the diffusion coefficient D as $\tau_D = {d_2}^2/D$. In the limit of low exciton density barely any EEA event would occur and the decay would be purely exponen-

tial. In this case $n_A(t)$ reduces to a mono-exponential decay $n_A(t) = \exp(-\gamma t)$[65]. Previous transient absorption experiments on the decay dynamics of E_{11} excitons in SWCNTs have suggested different models, including purely diffusion driven EEA [66, 67, 68] without including the exponential decay dynamics of bright excitons as frequently reported by time resolved PL experiments on SWCNTs over a ns time scale[56, 57, 69]. Thus, a unifying model describing PL and TA decay dynamics of E_{11} excitons seems to be missing. However, the theoretical model developed by Srivastava and Kono[65] (see Eq. 2.23) is capable of describing both decay mechanisms and will by applied to analyze and compare the experimental data collected by time resolved PL and TA measurements in this work. Since the probability of EEA events strongly depends on the exciton density, the exciton decay dynamics for different excitation fluences will be investigated. In particular, the limit of few initially created excitons will be probed and compared to the experimental model. Additionally, due to the surrounding environment and inhomogeneities of SWCNTs their decay dynamics is known to differ from tube to tube[56, 57]. Therefore, the exciton decay dynamics of individual tubes will be probed to avoid ensemble effects and to investigate decay variations due to single nanotube imperfections. This requires a highly sensitive microscopy setup with a low noise excitation source which will be introduced in chapters 3 and 4.

2 Transition metal dichalcogenides

After single-layer graphite, known as graphene, has triggered an outstanding increase of investigation of 2D materials due to its unique physical properties, a whole new group of 2D semiconductors has become of importance: The so called *Transition-metal dichalcogenides* (TMDCs). This material group is based on a single-layer of a transition metal M like molybdenum (Mo) or tungsten (W) sandwiched between two layers of a chalcogenide X like selenium (Se) or sulfur (S) giving the generic molecular formula MX_2[70]. Theoretical studies have predicted 52 different material combinations which are stable as single-layer[70]. Thinning down the TMDC bulk material to single-layer thickness e.g. by mechanical cleavage[71] or thermolysis[72] changes the physical properties of the material dramatically. For example, monolayer MoS_2 performs the transition from an indirect semiconductor to a direct semiconductor as been experimentally shown by Splendiani et al. in 2010[73]. In combination with strong light absorption TMDCs are a promising candidate for opto-electronical devices like ultrasensitive photodetectors[74].
In the following a short overview of the physical properties of TMDCs is given.

2.1 Structure

The six-fold bonding structure of the transition-metal is realized by an orbital hybridization of s-, p- and d-orbitals equivalent to the well known sp^3-hybridization. The so called coordinate covalent bond (or dative bond) results from the bonding between a vacant s-p-d-hybridized metal orbital and the lone pair electrons of the chalcogenide ligand in this case. In contrast to common covalent bonds where every bonding partner serves with an electron to the bonding both electrons are offered by the ligand in the coordinate covalent bond[75].

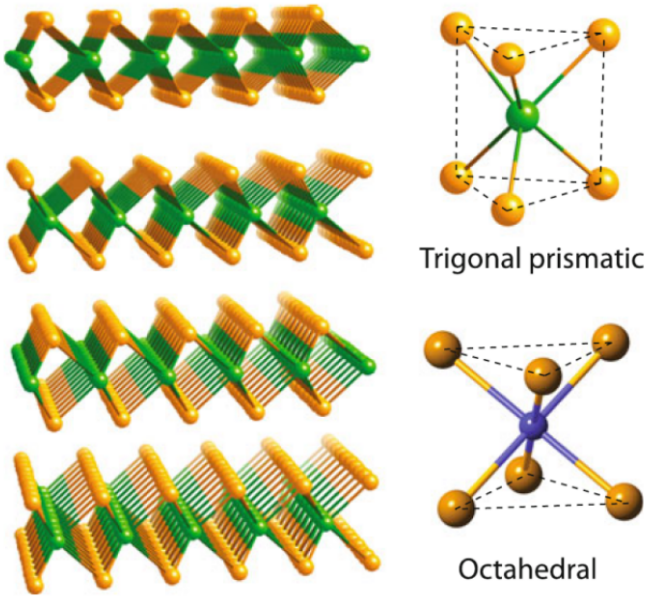

Figure 2.9: Crystal structure of a typical bulk TMDC (left). The metal atoms are shown in green whereas the chalcogenide atoms are depicted in yellow. The bonding geometry of the metal atoms can either be triagonal prismatic (top right) or octahedral (bottom right). Reprinted by permission from [75]. © 2016 Springer Nature.

In contrast, the separate layers of the TMDC are held together only by van der Waals forces which are of comparable strength compared to multilayer graphene[75]. The layers can be separated by mechanical exfoliation to the single-layer level[76]. These are stable and non-reactive due to the absence of dangling bonds[75].

2.2 Electronic properties

By decreasing the number of sandwiched TMDC-layers a transition from an indirect to a direct semiconductor has been observed experimentally when reaching a single-layer thickness[77]. There the QY of the photoluminescence increased strongly by

four orders of magnitude compared to the multilayer thickness of the material. This can be explained by the coincidence of the extrema of the valence band and the conduction band in momentum space. In this case, radiative recombination of excited states is possible without the need for additional phonon interactions and, therefore, is strongly enhanced. This shift of the extrema in the reciprocal space is attributed to an increase of the quantum confinement strength which enlarges the band gap energy of the indirect transition such that it outweighs the direct transition leading to the change from an indirect to a direct semiconductor[78, 77]. This is depicted in Fig. 2.10 where the calculated band structure of MoS_2 is shown for four different layer thicknesses. The solid arrows in the figure represent the lowest transition energy. The transition from an indirect to a direct semiconductor can be observed for the monolayer in Fig. 2.10d.

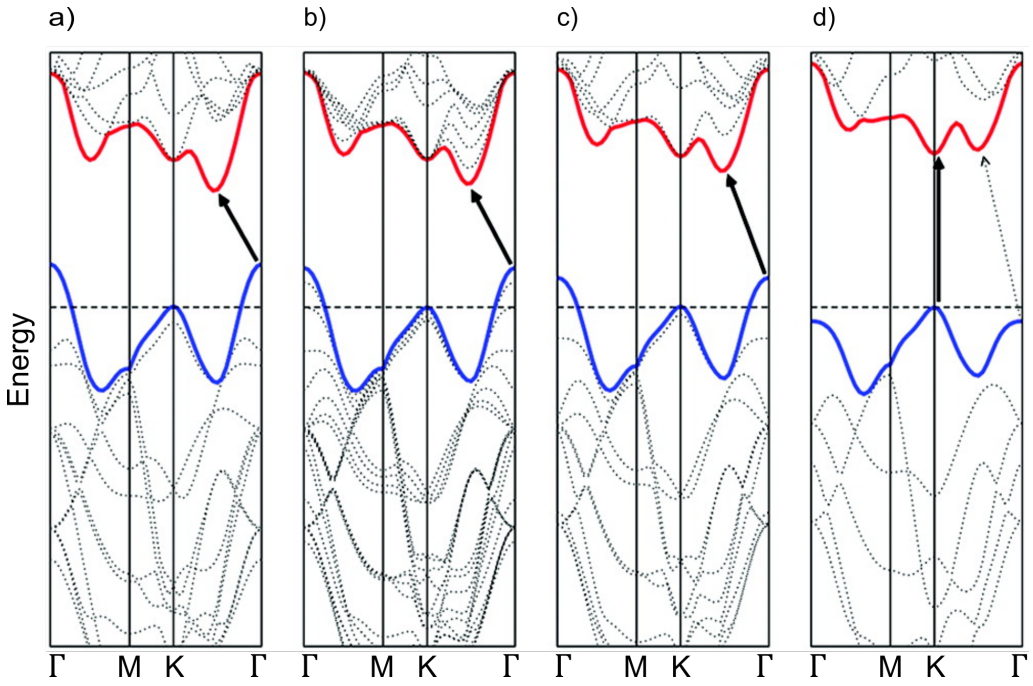

Figure 2.10: Calculated band structures of MoS_2 for the case of a) bulk material, b) quadrilayer, c) bilayer and d) monolayer. The solid arrows represent the lowest energy transitions. A single-layer of MoS_2 exhibits a direct band gap. Adapted by permission from [73]. © 2010 American Chemical Society.

The heavy metal atoms in TMDCs lead to an emerging spin-orbit splitting of the valence band of the single-layer material with values up to 456 meV[79]. This can be seen in the rise of two distinct absorption lines/emission energies in PL. These are commonly denoted as A and B absorption/emission peaks and can be addressed individually by photons of the corresponding energies[77].

The single-layer materials exhibit an inversion symmetry breaking which gives rise to a circular dichroism for equivalent valley points at different positions in momentum space (K and K′); thus, optical selection rules emerge dependent on the excitation polarization[80]. Electronic excited states in these points can be addressed either by right- or left-handed circular polarized light which gives rise to the field of *valleytronics* which could lead to new forms of electro-optical devices[81].

TMDCs show strong excitonic features due to reduced electrostatic screening of fields comparable to SWCNTs as explained in section 2.1. The optical properties of these materials are mainly governed by the excitons as measurements confirm an absorbance of up to 15% for the A-excitonic peak in a single-layer TMDC[82]. Bernardi et al. have shown absorption of single-layer MoS_2 in the order of 5-10% in the visible range traced back to excitonic absorption making it an interesting candidate for photovoltaic devices with nanometer thickness[83].
Further many-particle dynamics have been predicted and experimentally observed in the form of *trions* (charged excitons)[84], *biexcitons* (two bound excitons)[85] or interlayer excitons which were reported for heterostructures involving different TMDCs [86].
Transient absorption has evolved to a powerful technique to study the ultrafast optical response of TMDCs revealing a variety of excitonic effects like EEA[87], coherent phonons due to exciton trapping on defects[88] and transient changes of the exciton resonance energy and linewidth[89]. The observation of bandgap renormalization[90] and mid-gap defect states[91] leads to a transient optical response in TMDCs covering a wide spectral range besides the excitonic absorption peaks. Thus, transient absorption microscopy with a tunable probe wavelength as used in this work is an excellent tool to further investigate the role of material inhomogeneities on the microscopic level and their influence on the excitonic decay dynamics. With a high detection sensitivity, the transient absorption features spectrally apart from the absorption peak, especially below the A-excitonic peak, can be studied in detail. The microscopy setup used for this purpose is introduced in the next chapter.

Chapter 3

Experimental methods

In the following the physical background of confocal microscopy and its capability to reach the physical limit in spatial resolution given by the diffraction of light is described. The most common and easy approach in this technique is using the scattered or reflected light as contrast mechanism for imaging. However, the amount of information obtained by this technique is rather limited. There are plenty of different contrast mechanisms utilized with confocal microscopy as coherent anti-Stokes Raman scattering (CARS)[92], stimulated Raman scattering (SRS)[14], photoluminescence (PL)[13], transient absorption (TA)[15], second harmonic generation (SHG)[11] and a lot more, revealing plenty of physical material properties. In this work, photoluminescence microscopy and transient interferometric scattering (TiSCAT) microscopy will be used to investigate the dynamics of excited states in single-layer molybdenum selenide ($MoSe_2$) and individual single-walled carbon nanotubes. Both techniques can be used to extract time-resolved dynamics of the excited states but their signal formation differs significantly. Their physical mechanisms will be introduced in the following chapter.

1 Confocal microscopy

The principle of confocal microscopy is based on the approach that only light is collected by the detector which was emitted from the very point of excitation. Light coming from other positions of the sample is blocked. This is schematically shown in Fig. 3.1 where a commonly employed implementation called epi-geometry is depicted. A collimated laser beam is focused onto the sample on-axis in the object plane (shown as black line). The light emitted from the focal area is collected by the objective and partially reflected by a beam splitter. A second lens focusses the light onto a conjugate object plane where a pinhole is located in front of the detector.

Light which has its origin off-axis (blue line) or in a different depth in the sample (red line) is strongly suppressed by the pinhole. This leads to an increase of spatial resolution of the microscope given by the diffraction limit of the system.

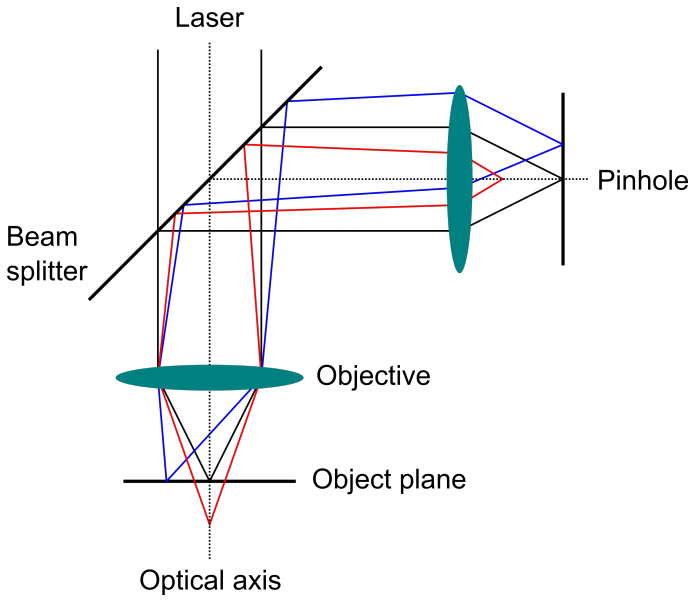

Figure 3.1: Schematic of the principle of confocal microscopy. Light coming from the sample but does not have its origin at the position of the focus (example ray traces in blue and red) is strongly suppressed due to the pinhole at the conjugate object plane. Exemplary beam paths are not for scale. Adapted from [19]

.

In contrast to common bright-field microscopy the focus spot has to be scanned over the sample in order to make imaging possible via point-to-point reconstruction. This can be done by piezoelectric displacement of the sample or by scanning the excitation and detection area via galvanometer scanning systems. Even experimental schemes where the excitation and detection spot are spatially separated are possible in which the recombination and mobility of diffusive excited states can be investigated[93].

Resolution limit

Considering the intensity profile of a point like emitter giving an Airy-pattern in the image plane called point-spread function (PSF), one can define the resolution limit as the minimal distance of two points in lateral direction at which both can still be distinguished which is also known as the Rayleigh criterion given for common

bright-field microscopy as[94]

$$\Delta r = \frac{0.61\lambda}{\mathrm{NA}}. \tag{3.1}$$

Here λ denotes the emission wavelength in the case of a fluorescent point object and $\mathrm{NA} = n \cdot \sin(\alpha)$ the numerical aperture of the objective with n being the refractive index between objective and sample and α the maximal angle to the optical axis under which a ray still contributes to the image and can enter the objective. In this criterion two points can still be distinguished when the intensity maximum of one emitter is located in the intensity minimum of the other emitter and vise versa.
In the case of confocal microscopy, there is an additional factor determining the resolution limit of the instrument given by the detection pinhole. The effective resolution can then be approximated by the multiplication of the detection PSF and the emission PSF in the case of a small pinhole ($d \leq 0.5$ Airy unit, AU). This yields a lateral resolution for an pinhole size significantly smaller than 1 AU given by[95]

$$\Delta r = \frac{0.37\lambda}{\mathrm{NA}}. \tag{3.2}$$

However, this increase of resolution causes a significant loss of transmitted intensity and, thus, has to be chosen as a good compromise between resolution and detection yield. The axial resolution is improved by confocal microscopy as well and has some important applications for example in cell biology. For example 3D models of tissue can be produced by additional scanning parallel to the beam axis[96]. This will not be further pointed out in this thesis as the axial resolution has a less important role in image contrast for low-dimensional materials. Further details can be found in the corresponding literature[94, 95].

1.1 Time correlated single photon counting

A commonly used technique for time resolved measurements of fast radiative decay processes is *time correlated single photon counting* (TCSPC)[97]. Here the statistical distributed event of the emission of a photoluminescence photon is detected and correlated to a corresponding reference signal e.g. a laser pulse signal from a second photodiode. The time between the reference signal pulse and the event of the photon detection is determined electronically and stored in a corresponding timing bin as an additive entry. By summing up a large number of detection events the actual temporal shape of the decay can be reconstructed. This is depicted in Fig. 3.2.

For the measurement utilizing lasers with high repetition rates, the detection scheme is reversed: When a photon is detected, the time until the next reference pulse arrives is measured (*reversed start-stop*). By this technique the requirements on the speed of the electronic timing system can be lowered. It is important that the count rate of the APD detector is significantly smaller than the repetition rate of the excitation laser to prevent multiple detection events within one laser pulse cycle. Higher count rates would lead to the so called *pile up event* which warps the reconstructed pulse shape as later arriving photons are neglected in the detection scheme [97].

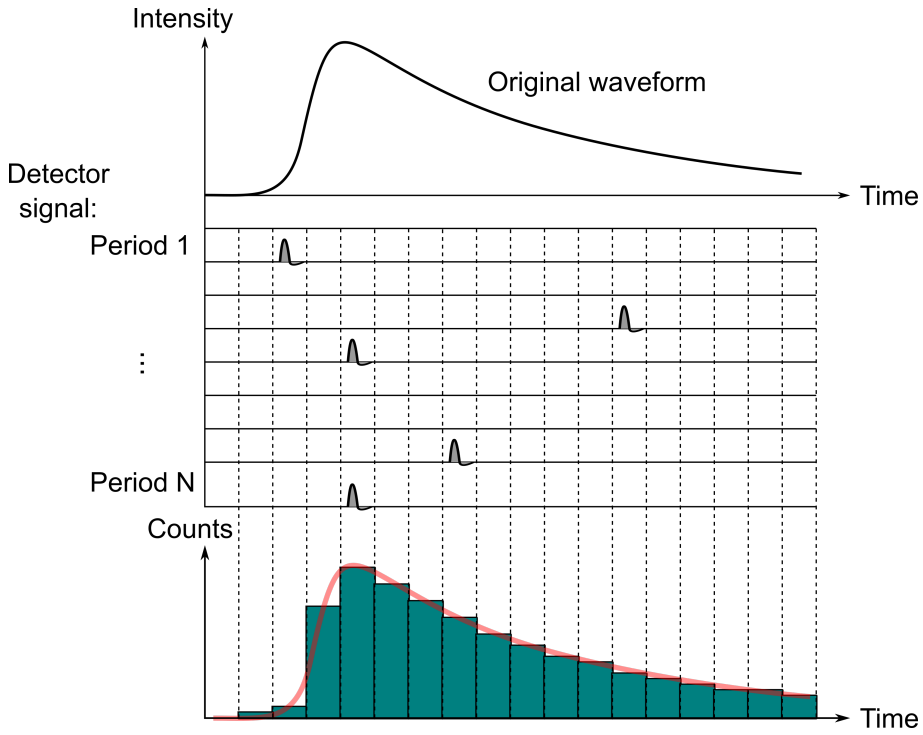

Figure 3.2: Principle of Time-correlated single photon counting (TCSPC). Every counting period is started by a reference event. The time until the detection of a PL photon is stored in a corresponding digitized bin. Adapted from [97].

Time correlated single photon counting is an extremely sensitive technique for measuring events in the picosecond to nanoseconds range. The minimal temporal resolution is limited by the instrument response function (IRF) given by the timing jitter of the electronics and the detection uncertainty of the APD. The detector can absorb the photon in different depths of the depletion region leading to a timing uncertainty. Further detection events of excited free charge carriers from outside the avalanche region lead to further detection events that form an elongated tail of the IRF called the *diffusion tail*. This can be seen in Fig. 3.3 which shows the

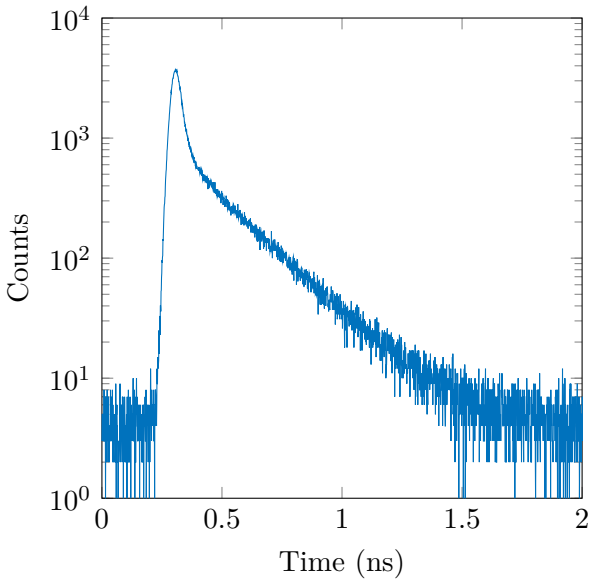

Figure 3.3: Measurement of the instrument response function (IRF) of the TCSPC setup. The laser was set to a center wavelength of 1000 nm.

measurement of an IRF at a laser center wavelength of 1000 nm. Small detector areas minimize these effects, leading to a width of the response function down to approximately 30 ps (FWHM). This can be measured by transmission of a small portion of the excitation laser beam onto the APD and correlating the detected events with its own reference signal. This should be performed utilizing the wavelength expected for the PL measurement as the IRF is dependent on the energy of the detected photons due to their different penetration depths (shown in reference [19] on the experimental setup utilized in this work). By convolution of the model function of choice with the measured IRF curve, decay dynamics down to approximately 10% of the width of the IRF can be determined[98]. In the present case, this would translate to a temporal resolution of approximately 3 ps.

In a typical experiment carried out in this work, the excitation power was set in a way that the count rate of the APD was below 10 kHz and a typical measurement took an acquisition time in the order of several minutes on a single SWCNT. This prevented the sample from photobleaching but yielded a sufficient SNR for further fitting of a model function. Fitting of different function types was done using the program *expFIT* written in Matlab by Alexander Biewald. Here user-defined fit functions are convoluted with the IRF and fitted to the experimental data via a trust-region method.

1.2 Transient interferometric scattering microscopy

Interferometric scattering (iSCAT) microscopy is based on the interference between a reflected or transmitted reference light field and a (potentially weak) light field scattered by the sample particle. In contrast to PL microscopy it does not rely on the radiative recombination of excited states. This increases the range of materials observable with this technique. The first report on interference scattering imaging of nanoparticles was published 2004 by Lindfors et al.[99]. The high sensitivity of this method was used later to track smallest particles like single viruses[17], proteins[100] or gold nanoparticles with few nanometer size [18, 101] without the need for fluorescent labelling.
In the underlying experiment, which is in epi-configuration (see section 3.2) the reference field $\overline{E}_r$ is given by the reflected field on the glass-air interface of the sample cover slide. The scattered field $\overline{E}_s$ originates from the sample under test e.g. a SWCNT or a single-layer of $MoSe_2$. The origin of the fields is depicted in Fig. 3.4.

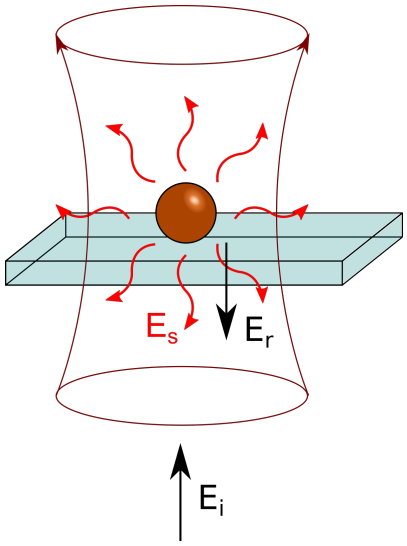

Figure 3.4: Field contributions to iSCAT signal. A fraction of the initial electrical field is reflected at the glass-air interface (E_r). A smaller portion is scattered by the particle (E_s). Adapted from [102].

The intensity on the detector I_{det} can be written in terms of the interfering fields as[103]

$$I_{det} \sim |\overline{E}_r + \overline{E}_s|^2 = I_r + I_s + 2E_r E_s \cos(\Delta\phi). \tag{3.3}$$

Here $\overline{E}_r = E_r \exp(i\phi_r)$ and $\overline{E}_s = E_s \exp(i\phi_s)$ denote the complex electric fields of the scattered and reflected light and $\Delta\phi$ the phase difference between between them. The intensity of the fields is calculated as $I = |\overline{E}|^2$. Thus, equation 3.3 can be expressed in terms of the scattering and reflection coefficients r and s, respectively:

$$I_{det} \sim I_0 \left(|r|^2 + |s|^2 + 2|r||s|\cos(\Delta\phi) \right). \tag{3.4}$$

The cross-term originating from the interference between both field components can be expressed in terms of the individual phases as a combination of the Gouy-phase ϕ_{Gouy} arising from the focused excitation condition and from the scattering event ϕ_s on the sample imposed by material properties: $\phi = \phi_{Gouy} - \phi_s$. In the case of a focused excitation spot in the distance z from the scattering particle and z_R denoting the Rayleigh length of the focused beam, the Gouy phase shift of the reflected beam with respect to the light scattered at the sample equals[104]

$$\phi_{Gouy} = -\frac{\pi}{2} + \arctan\left(\frac{z}{z_R}\right). \tag{3.5}$$

With this, equation 3.4 becomes

$$I_{det} \sim I_0 \left(|r|^2 + |s|^2 + 2|r||s|\cos\left(-\frac{\pi}{2} + \arctan\left(\frac{z}{z_R}\right) - \phi_s\right)\right). \tag{3.6}$$

In case of weakly scattering objects, the scattering term becomes sufficiently small as it drops with the sixth power of the particle size[103]. Consequently, the interference term dominates in this case as it is linearly proportional to the scattered field. Thus, the iSCAT contrast is favourable when it comes to the detection of weakly scattering objects.

By further taking into account the relations $\cos(x) = \cos(-x)$ and $\cos(\frac{\pi}{2} + \phi) = -\sin(\phi)$ and the focus spot at the position at the scattering particle ($z = 0$) equation 3.6 can be written as

$$I_{det} \sim I_0 \left(|r|^2 - 2|r||s|\sin(\phi_s) \right) = I_0 \left(|r|^2 - 2|r|\mathrm{Im}(s) \right). \tag{3.7}$$

In the electrostatic approximation for particles smaller than the excitation wavelength, the scattering coefficient s is proportional to the polarizability α describing the optical response of the particle to the external field[105]. The imaginary part of s is directly proportional to the absorption cross section σ_{abs} such that equation 3.7 becomes[106]

$$I_{det} \sim I_0 \left(|r|^2 - 2|r|\mathrm{Im}(s) \right) \sim I_0 \left(|r|^2 - 2|r|\sigma_{abs} \right). \tag{3.8}$$

While equation 3.8 applies to nanoscale particles and can thus be used to describe the absorption response of single SWCNTs its applicability to particles of larger extent, like 2D monolayers, is not necessarily given. Here, the scattering response can be characterized in terms of the Fresnel coefficients describing the 2D layer either via a refractive index and an effective thickness or via its sheet optical conductivity[107]. Additionally, the scattered field component I_s can no longer be neglected due to the extent of the layer as assumed in the calculations before and potentially outweighs the interference term (see Eq. 3.6). The further quantification of the sample response in the employed configuration is rather complicated due to additional phase effects like the non-vanishing Gouy phase of the scattered field or the Goos-Hänchen shift occurring for total internal reflection for angles exceeding the critical angle[108].

Transient iSCAT

By introducing a pump-probe scheme, one can utilize the transient iSCAT contrast to investigate the dynamics of excited states in the particle. By irradiating the sample with an optical pulse the initial absorption cross section can be altered for subsequent probe pulses. Assuming σ^* being the absorption cross section after excitation of the sample by a pump pulse, the signal after lock-in detection becomes

$$\boxed{\frac{\Delta I}{I_0} \sim -(\sigma^* - \sigma).} \tag{3.9}$$

Equation 3.9 shows that the TiSCAT signal is directly proportional to the pump induced changes in sample absorption. Several effects can have an influence on the TiSCAT signal amplitude and sign. These are depicted in Fig. 3.5 and described below based on [109]:

Ground state bleaching and Pauli-blocking: By excitation of higher lying states by the pump pulse the occupation number of the ground state is decreased and by that the possibility for the absorption of a further photon. The absorption cross section is lowered which results in a positive TiSCAT signal. Furthermore, the occupation of higher lying states prevents the further excitation of these states due to the Pauli exclusion principle where Fermions like electrons cannot occupy the same quantum state and so the transition is forbidden.

Stimulated emission: Assuming a two-level system, the Einstein coefficients determining absorption (A_{12}) and stimulated emission (A_{21}) of the system are identical. Thus, after excitation of the higher lying state stimulated emission will occur during transmission of the subsequent probe-pulse. The excited state relaxes to the ground state through the stimulation of the probe light emitting a photon at the same

wavelength as the probe wavelength. This leads to an increase of the intensity and, thus, seemingly to a decrease of the absorption cross section resulting in a positive TiSCAT signal.

Excited state absorption: After excitation there may be higher lying states present whose energy difference to the pump-excited state corresponds to the energy of the probe photons. This leads to an additional absorption channel increasing the absorption cross section of the sample for the given probe wavelength. This leads to a negative TiSCAT signal contribution.

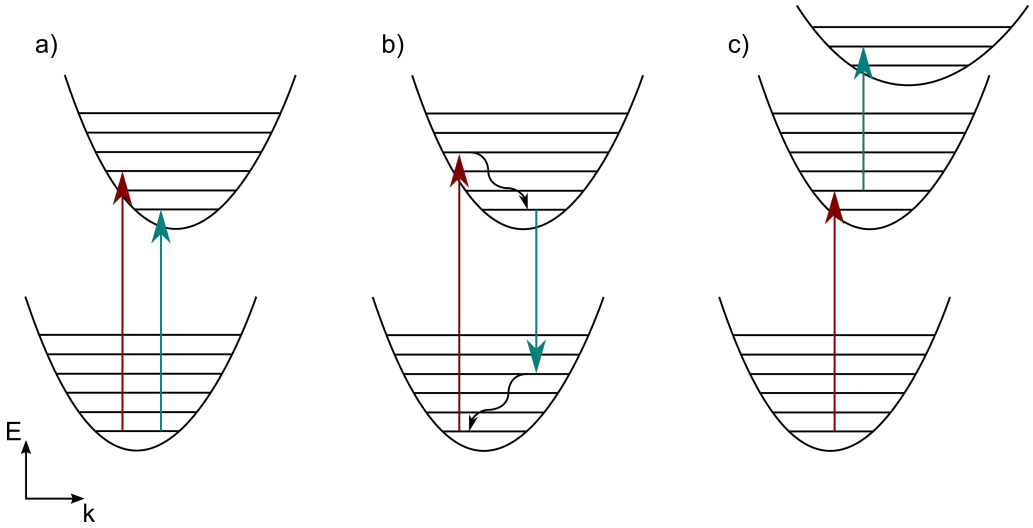

Figure 3.5: The three signal contributions possible in transient interferometric scattering: a) Ground state bleaching and Pauli-blocking, b) stimulated emission and c) excited-state absorption. Adapted from [110].

The effects listed before where assumed in case of a constant spectral position of the electronic states. However, the photo-excitation of charge carriers can modify the band gap energy due to many body interactions and thus lead to a spectral shift of the absorption resonances of the investigated material. This effect is called *bandgap renormalization* (BGR). Due to the strong spatial confinement and reduced shielding of fields, BGR is pronounced in low-dimensional materials and has already been observed for TMDCs and SWCNTs[90, 111]. Depending on the probe wavelength this shift of the excited state energies can lead to an increase or decrease of transient absorption.

2 TiSCAT/PL microscopy setup

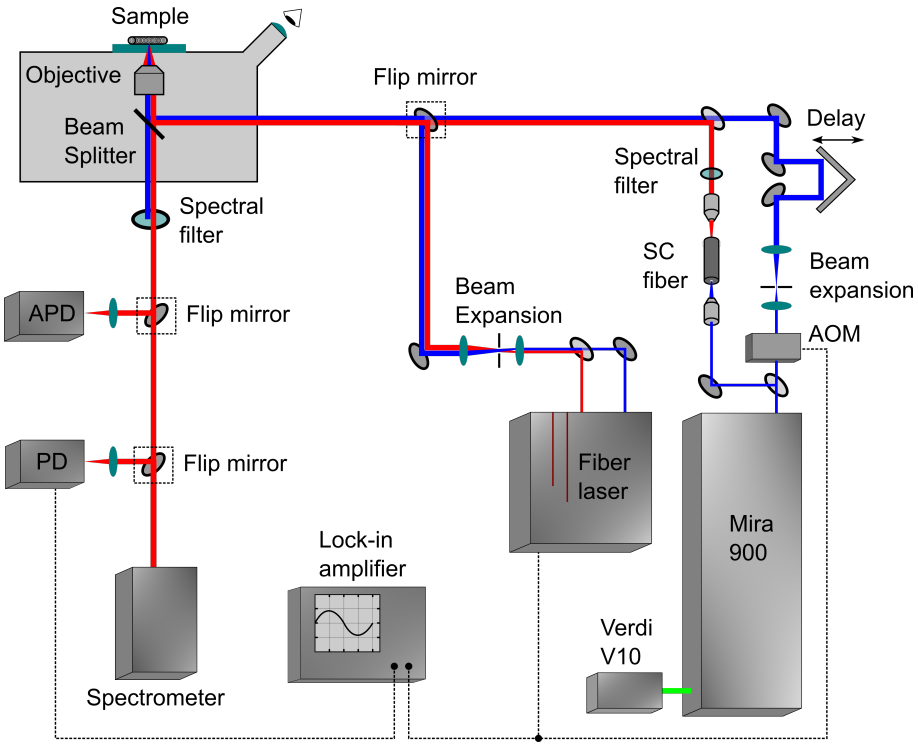

Figure 3.6: Experimental setup of the TiSCAT/PL microscope. The excitation light source can be chosen by a flip mirror. Dashed lines represent electrical signal lines for the lock-in detection. The detection scheme can be switched by flip mirrors between a single photon avalanche photodiode (APD), a fast photodiode (PD) or a spectrometer. A detailed experimental description can be found in the text.

The setup utilized in this thesis is shown in Fig. 3.6. Two different laser sources can be used for excitation of the sample material. They are selected by a flip mirror. The first laser line (right side in the figure) is fed by a Ti:Sa oscillator (Coherent Mira900) at a repetition rate of 76 MHz with an adjustable center wavelength in the range of 700 nm to 900 nm. The output is split into two arms by a pellicle beamsplitter to be able to carry out pump-probe experiments. The pump arm (depicted in blue) passes through an acousto-optic modulator (AOM) which switches the pulse train at a frequency of approximately 100 kHz. The measured signal is demodulated with a lock-in amplifier (LIA) at this very frequency to increase the measurement sensitivity. With this technique, noise contributions of the probe light at other frequencies than the modulation frequency can be suppressed. Low frequency noise contributions like mechanical influences of the environment or 1/f-noise of the laser

are minimized by fast modulation of the pump beam. A beam expansion containing a pin hole at the focus point extends the beam diameter for a sufficient filling of the aperture of the microscope objective and improves beam quality. A retroreflecting mirror located on a translation stage (20 mm range of motion) allows for an adjustable time delay between the pump and the probe arm. To probe at a different wavelength than the pump wavelength the light pulses emitted by the laser are coupled into a supercontinuum fiber (*SC fiber*, Femtowhite800 from NKT Photonics). In this device highly nonlinear effects like self-phase modulation lead to an extensive broadening of the pulse spectrum spanning from the visible to the NIR (up to approximately 1100 nm). A subsequent spectral filter allows for selection of a specific wavelength range of interest.

The second laser source is a new customized fiber laser built at TOPTICA Photonics AG based on the FemtoFiber Ultra product line. It emits two wavelengths simultaneously which can be modulated and delayed internally, combining essential parts of the experiment inside the housing. Furthermore, the probe arm is continuously tunable in its output wavelength between 810 nm and 960 nm, eliminating the need for further spectral filtering of the beam. The development of the laser system was carried out preceding the microscopy measurements and is described in chapter 4.

Both laser beams of the fiber laser system are spatially overlapped and expanded after the system output. The laser source (Ti:Sa setup or fiber laser) can be switched by flipping a mirror ahead of the microscope.
The laser beam is guided into a commercially available inverted microscope (Nikon Eclipse TE2000-S) where the beam power can be adjusted by inserting optical density filters. A portion of 70% of the the beam gets reflected at the 30/70 beam splitter and is focused onto the sample by an oil immersion objective with a NA of 1.49 (Nikon CFI apochromat TIRF 60x). The reflected and scattered probe light (in the case of a TiSCAT measurement) or photoluminescence light is collected by the objective. A fraction of 30% transmits through the beamsplitter and enters the detection path. Here the pump light is removed by spectral filtering from the probe light or the photoluminescence light, respectively. Depending on the measurement method the light is then focused onto a single photon avalanche photodiode (APD) for PL-microscopy or TCSPC-measurements, a fast photodiode (Femto LCA-S-400K-SI) for TiSCAT measurements or enters a spectrometer for spectrally resolved PL/TiSCAT measurements.

The camera of the spectrometer (Andor Newton) can be read out with frequencies up to 600 Hz. This can be used for spectrally resolved TiSCAT measurements with lower sensitivity. There the recording of the spectra is triggered by the AOM

modulation frequency such that alternating spectra with and without the sample irradiation with pump light are taken. The TiSCAT spectra can than be extracted from the measured data sets. A sensitivity of up to approximately $1 \cdot 10^{-4}$ was achieved by averaging typically over several thousand single TiSCAT-spectra.
The microscope is operated in sample-scanning mode: The laser is focused onto the sample which is raster scanned by an piezoelectric stage. For every spot the corresponding measurement signal is taken (PL intensity or TiSCAT amplitude) and the microscope image can be reconstructed from the associated contrast mechanism. For time resolved measurements the focus spot is fixed at one sample position and the TiSCAT or TCSPC transient can be taken. PL spectra of the sample can be measured in the same way utilizing the spectrometer as detector.

3 Sample preparation

(6,4) SWCNTs

The (6,4) single-walled carbon nanotubes used in this thesis were produced by chemical vapour deposition (CVD) via the HiPCO-method (high-pressure catalytic decomposition of CO) developed by Nikolaev et al. in 1999[112]. Here carbon monoxide acts as the carbon feedstock and gaseous iron pentacarbonyl as the metal-particle catalyst precursor for the production process of the carbon nanotubes. The mixture is fed into a furnace and heated to temperatures up to 1200 °C. By variation of the reaction temperature and pressure different diameter distributions can be achieved. Compared to other established production methods for SWCNTs the tubes of the HiPCO process are rather thin[113].
The raw HiPCO material was further separated to nearly single chirality purity of (6,4) carbon nanotubes by aqueous two-phase (ATP) separation as suggested by Subbaiyan et al.[114]. First, single-walled carbon nanotubes were individualized by stirring the CNT raw powder in 1 wt%-sodium deoxycholate (DOC) solution for 5 weeks. Stirring of the sample solution breaks the bundles of carbon nanotubes that form due to van der Waals interactions. The DOC molecules act as a surfactant for the individualized carbon nanotubes by the formation of micelle structures around the tube preventing them from clustering together. Different surfactants can be used for example sodium deoxycholate (DOC), sodium dodecylsulfate (SDS) or sodium cholate (SC). A mixture of these components was used to create micelles of different densities and preferred encapsulation chiralities. This can be further used to separate different types of single-walled carbon nanotubes via an ultra centrifugation process and subsequent separation of the different density phases showing up.

In this way, the HiPCO raw material was separated to a nearly single chirality (6,4) SWCNT solution. The solution was then spincoated onto a glass cover slide for microscopy.

(6,5) SWCNTs

The sample material containing the polymer-wrapped (6,5) SWCNTs was provided by the group of Prof. Hertel from the Julius-Maximilians-University Würzburg. Organic polymer stabilized SWCNT samples were produced from shear-mixing nanotube raw material and 9,9-dioctylfluorenyl-2,7-diyl (PFO) and bipyridine (BPy) copolymer in toluene for 13 h followed by filtration. 30 µl of this suspension were deposited on thin glass coverslides by spincoating. To reduce environmental perturbations and to decouple the SWCNTs from the glass surface, cover slides were precoated by a thin (30 nm) polystyrene layer.

Single-layer $MoSe_2$

The sample material containing the single-layer $MoSe_2$ was provided by Dr. Achint Jain from the group of Prof. Lukas Novotny at the ETH Zürich. Monolayer $MoSe_2$ samples were obtained by mechanical exfoliation and polymer-assisted transfer onto a glass cover slide covered by 40 nm of hexagonal boron nitride (hBN). After transfer, polymer residues, interfacial bubbles and wrinkles were efficiently removed by vacuum-annealing at 200°C resulting in a stacked layer formed by MoSe2 on hBN on glass without gap. More details about the sample preparation recipe can be found in ref.[115].

Chapter 4

Development of a two-arm fiber laser system

Transient absorption measurements with high sensitivity often require very complex, costly and bulky experimental setups as titanium:sapphire laser systems. These often include additional optical parametric amplifiers/oscillators (OPA/OPO)[116][15] to generate pump and probe pulses at the desired wavelength of interest. Other pump-probe experiments make use of highly nonlinear supercontinuum generation [117][118] which is a potential source of intensity noise limiting the sensitivity of the experiment as shown later in the experimental section. Furthermore, these systems often exhibit a variety of optical components along the beam path for light manipulation making frequent realignment of the experiment necessary.
In this work an ultrafast fiber laser system was developed combining nearly all optical components of the light source necessary for transient interferometric scattering microscopy with high sensitivity. The soliton self-frequency shift (SSFS) was utilized to produce wavelength-tunable probe laser light covering a broad spectral range of 150 nm.
Applications of fiber lasers utilizing the SSFS have already been demonstrated for a variety of contrast mechanisms including CARS[119], three-photon excitation[120], fluorescence/phosphorescence lifetime imaging[121] and have been proposed as potential turnkey systems for endoscopic imaging of tissue[122] speaking for high stability and good noise characteristics of such laser sources.
In the following chapter the development of the fiber laser system will be pointed out. At first, the basic principles of pulse propagation in fiber lasers is introduced. Furthermore, several nonlinear optical effects like soliton-propagation and second harmonic generation are presented. As it has a strong influence on the signal-to-noise ratio of TiSCAT measurements, the origin of intensity noise will be explained.

Finally, the introduced principles will be put together to introduce the developed fiber laser system and the characterisation of the two laser arms.

1 Light guidance in optical fibers

Optical fibers manifest in a variety of different types and areas of application. The easiest type is the step-index fiber which consists of a cylindrical core and a surrounding cladding of smaller index of refraction. In the simple picture of ray optics this leads to total reflection of light that is coupled into the core region under the acceptance angle Θ_{max} which is determined by the numerical aperture NA of the fiber and, thus, by the difference of the refractive indexes of the materials[123]:

$$\mathrm{NA} = n_0 \sin(\Theta_{max}) = \sqrt{{n^2}_{core} - {n^2}_{clad}}. \tag{4.1}$$

Here n_0, n_{core} and n_{clad} denote the refractive index of the surrounding material from which the light is coupled into the fiber (e.g. air) and the refractive indexes of the core and the cladding, respectively. In the limit of a small core diameter the viewpoint of ray optics is no longer justified and the transmission of light has to be treated in wave optical point of view where the optical fiber acts as a wave guide with dielectric walls given by the index step. There the solutions of the wave equations yield several different transverse modes (*transverse electric* (TE)) whose electrical field vector is perpendicular to the optical axis z. By thinning down the fiber geometry it can be achieved that only one single mode is guided in the device. This type of fiber is therefore called *single mode fiber* (SM fiber) and the corresponding diameter d of the core for a certain wavelength λ is given by[123]

$$\mathrm{d} \leq \frac{0.76\lambda}{\sqrt{{n^2}_{core} - {n^2}_{clad}}}. \tag{4.2}$$

The field strengths of the guided mode do not drop to zero at the position of the core to cladding interface due to continuity restrictions of the fields. So the light is also partially guided in the cladding. The corresponding intensity distribution can be approximated by a Gaussian function symmetrical to the optical axis[124].
The wave guide transmission adds an additional chromatic dispersive effect besides the commonly known chromatic dispersion of the material[125]. This gives rise to the possibility of dispersion management due to variations of the material and geometrical properties of the fiber.
Besides the common step-index fibers other types of fibers are widely used as for example *highly nonlinear fibers* (HNLF) where nonlinear effects are enhanced due to

small mode field diameters[126], doped *active fibers* for laser amplification or *hollow-core fibers* suited for sensing purposes[127]. Also geometrical variations along the fiber can be realized as shown for fiber based Bragg gratings which can be created inside a single mode fiber core via laser irradiation. These act as a wavelength dependent fiber mirror or even as a dispersive element[128].
Typical *mode field diameters* (MFD, the diameter over which the intensity decreases to $1/e^2$) in single mode fibers are in the order of 10 µm[124]. This leads to the possibility of maintaining high optical intensities over nearly unlimited distances, thus taking advantage of nonlinear effects as self-phase modulation or solitonic propagation. This will be explained in the following sections in more detail.

2 Nonlinear pulse propagation

> "Nonlinear optics is the study of phenomena that occur as a consequence of the modification of the optical properties of a material system by the presence of light." [129, p. 1]

Due to the high electrical fields necessary to induce a nonlinear behaviour in optical media the resulting effects are mainly noticeable in laser driven applications and experiments. The first experimental discovery of an optical nonlinear effect utilizing a laser like source is attributed to Franken et al. in 1961 who discovered the frequency doubled component of a ruby optical maser beam sent through a quartz crystal [130]. Since this finding several other nonlinear effects have been predicted theoretically and experimentally proven like higher order harmonics (second harmonic generation (SHG), third harmonic generation (THG) and higher), self-phase modulation (SPM), supercontinuum generation, self-focussing in media and various others. This variety of effects is the basis for modern pulsed light sources with broad wavelength coverage which could not be generated with commonly used active media like Ytterbium and Erbium because of their spectrally limited gain. Also the realization of ultra short pulse durations below several femtoseconds is a consequence of optical nonlinear effects as high-order harmonic generation[131].

Derivation from induced polarization
In linear optics the induced polarization in a medium by an electrical field $E(t)$ is given by

$$\vec{P}(t) = \epsilon_0 \chi \vec{E}(t), \tag{4.3}$$

where ϵ_0 describes the permittivity of vacuum and χ the linear susceptibility which is a tensor in general. For simplicity the fields $\vec{E}(t)$ and $\vec{P}(t)$ will be treated as scalar quantities in the following. To introduce a nonlinear behaviour of the medium this formula can be expanded as a power series in the electrical field strength $E(t)$:

$$P(t) = \epsilon_0[\chi^{(1)}E(t) + \chi^{(2)}E(t)^2 + \chi^{(3)}E(t)^3 + ...]. \tag{4.4}$$

Here $\chi^{(1)}$ is the linear susceptibility and $\chi^{(n)}$ for $n > 1$ are the nonlinear susceptibilities of higher order polarizations. It should be noticed that $\chi^{(2)}$ is only non-vanishing for materials not exhibiting an inversion symmetry hence showing no nonlinearity of second order. However, a third order susceptibility is possible for both cases, centrosymmetric and noncentrosymmetric materials (like amorphous quartz glass)[129]. In this work several nonlinear effects were used in order to create the optical pulse characteristics needed for the experiment. The final sequence of the utilized effects is summarized in chapter 4.4 where the complete fiber laser system is shown. At first, the concept of the pulse propagation in form of an *optical soliton* as a consequence of self phase modulation in combination with chromatic dispersion will be introduced which is used for the stable propagation of the light pulses through the optical fibers inside the laser. This leads to the preservation of pulse duration and spectral characteristics during propagation through the optical media. Secondly, the nonlinear effect named *soliton self-frequency shift* used for tuning the output wavelength of the probe beam will be introduced. The third nonlinear effect which will be explained is the generation of the second harmonic of the fundamental laser wavelength at 1560 nm to generate pulses at a center wavelength of 780 nm used as the pump beam in TiSCAT microscopy.

2.1 Soliton pulse propagation

Self phase modulation Considering a medium with a vanishing second order susceptibility $\chi^{(2)} = 0$ (e.g. a quartz glass fiber) and taking only into account the third order susceptibility $\chi^{(3)}$ besides the linear response $\chi^{(1)}$ of the medium, Eq. 4.4 becomes

$$P(t) = \epsilon_0[\chi^{(1)}E(t) + \chi^{(3)}E(t)^3]. \tag{4.5}$$

For a monochromatic, linear polarized wave $E(t) = E_0 \cdot \cos(\omega t)$ and the use of the identity $\cos^3(\omega t) = \frac{1}{4}\cos(3\omega t) + \frac{3}{4}\cos(\omega t)$ this yields for the terms oscillating at the fundamental frequency ω:

$$P(t) = \epsilon_0 \left[\chi^{(1)} + \frac{3}{4}\chi^{(3)}|E_0|^2\right] E(t) = \epsilon_0(\chi^{(1)} + \Delta\chi)E(t). \tag{4.6}$$

By the relation $n_0^2 = 1 + \chi^{(1)}$ the additional term $\Delta\chi$ relates to a nonlinear incremental change of the linear susceptibility. So it can be computed as an incremental change of the linear refractive index n_0 in the form

$$\Delta n = \frac{\partial n}{\partial \chi}\Delta\chi = \frac{\partial(1+\chi)^{\frac{1}{2}}}{\partial\chi}\Delta\chi = \frac{\Delta\chi}{2\sqrt{1+\chi}} = \frac{\Delta\chi}{2n_0} = \underbrace{\frac{3\chi^{(3)}}{4n_0^2\epsilon_0 c}}_{n_2} I. \tag{4.7}$$

Hence the intensity dependent refractive index can be represented as $n(I) = n_0 + n_2 I$. Here the intensity of the electric field was used in the form $I = \frac{1}{2}n_0\epsilon_0 c|E_0|^2$. For the effect of this nonlinear deviation of the refractive index on an ultra short pulse propagating over a distance z in a medium the instantaneous phase of the pulse can be written as

$$\phi(t) = \omega_0 t - k_0 z = \omega_0 t - \frac{2\pi}{\lambda_0} n(I) z. \tag{4.8}$$

Thus, the instantaneous frequency is given by

$$\omega(t) = \frac{d\phi(t)}{dt} = \omega_0 - \frac{2\pi}{\lambda_0}\frac{dn(I)}{dt} z. \tag{4.9}$$

For a Gaussian shaped pulse $I(t) = I_0 \exp(-\frac{t^2}{\tau^2})$ this yields

$$\omega(t) = \frac{4\pi z n_2 I_0}{\tau^2} \cdot t \cdot \exp(-\frac{t^2}{\tau^2}). \tag{4.10}$$

The effect of this so called *self phase modulation* (SPM) on a propagating pulse is shown in Fig. 4.1 for the example of a Gaussian pulse. For positive values n_2 the front of the pulse exhibits a negative frequency shift which is equivalent to a red shift whereas the tail of the pulse is shifted to the blue. Only the center part of the pulse is unaltered at the initial center frequency ω_0. Such an optical pulse with temporally varying instantaneous center frequency is also called a *chirped* pulse comparable to the acoustic sounds of birds in nature. It should be noticed that for a frequency shift exceeding the initial spectral bandwidth of the pulse it undergoes a symmetric spectral broadening to both sides of the center frequency. From Fig. 4.1 it can be seen that for a certain frequency shift (except the extrema) there are always two associated distinct points in time exhibiting the same value. This results in identical frequency components shifted in time leading to oscillating destructive and constructive interference effects in the spectrum of the pulse[132]. The generated spectrum exhibits an oscillating behaviour which is typical for SPM.

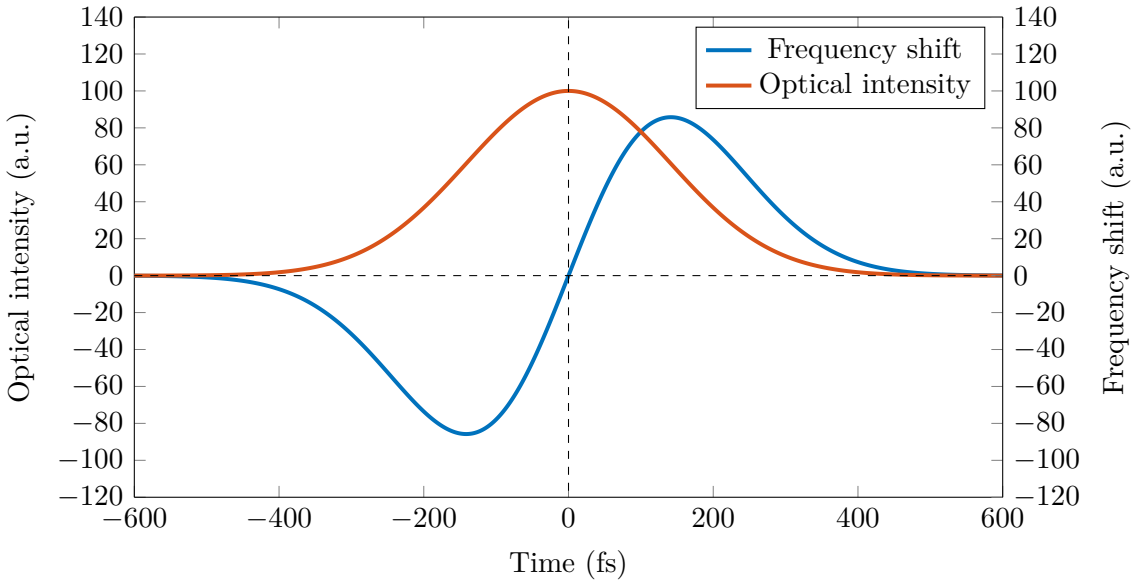

Figure 4.1: The effect of self phase modulation on a pulse with Gaussian shape ($\tau_{\frac{1}{e}} = 400$ fs). The front of the pulse (negative times) is red-shifted whereas the tail (positive times) undergoes a blue-shift.

Chromatic dispersion So far, dispersive effects where neglected. For a more complete description of pulse propagation in media the dependence of the wavelength on the refractive index must be considered. To quantify this *chromatic dispersion relation* a Taylor series of the propagation constant $\beta(\omega) = n(\omega)k_0$ as a function of the frequency ω around the center frequency ω_0 is carried out[133]:

$$\beta(\omega) = \beta_0 + \beta_1(\omega - \omega_0) + \beta_2(\omega - \omega_0)^2 + \beta_3(\omega - \omega_0)^3 + \dots . \tag{4.11}$$

Here β_n denotes the value of the n-th derivative of $\beta(\omega)$ at ω_0. In the following the influence of β_1 and β_2 on the pulse propagation will be pointed out:

- $\boldsymbol{\beta_1}$ is the inverse of the *group velocity* ($\beta_1 = \frac{1}{v_g}$) which describes the velocity of the pulse envelope[132]. Without higher orders of chromatic dispersion the propagation of a pulse would not change the form of the envelope even if the phase velocities v_{ph} of its spectrum differ. There would be just a slipping of the field oscillation with regard to the pulse envelope.

- $\boldsymbol{\beta_2}$ (which is also called *group velocity dispersion*, GVD) leads to a temporal broadening of the optical pulse during propagation. Dependent on the sign of the second order dispersion one has to distinguish between *normal dispersion* ($\beta_2 > 0$) which is the case for most optical media in the visible range and *anomalous dispersion* ($\beta_2 < 0$) which is known to be present in several media

in the IR spectral region. Both types of GVD lead to a chirp whose orientation in time is dependent on whether its normal or anomalous dispersion. $\beta_2 > 0$ leads to a red-shifted leading edge followed by a blue-shifted tail and vice versa for the anomalous case.

Nonlinear Schrödinger equation In order to merge the nonlinear effect of self phase modulation and the chromatic dispersion which both predominantly govern the propagation of ultrashort optical pulses in media the following method is shown closely based on the work of Byod[129] and Agrawal[132]. The propagation of waves can be described by the wave equation written in the form

$$\nabla^2 \vec{E} - \frac{1}{\epsilon_0 c^2} \frac{\partial^2}{\partial t^2} \vec{D} = 0, \tag{4.12}$$

where $\vec{D} = \epsilon_0 \vec{E} + \vec{P}$ describes the total displacement field. By the Fourier transformation of $\vec{E}$ and $\vec{D}$ to the frequency domain and the assumption of a slowly varying amplitude $A(z,t)$ of the electrical field which allows for dropping second order derivatives in space the following formula can be derived:

$$\boxed{\frac{\partial A}{\partial z} + \frac{1}{2} i \beta_2 \frac{\partial^2 A}{\partial \tau^2} = i\gamma |A|^2 A.} \tag{4.13}$$

Here the time frame was substituted by the retarded time $\tau = t - \beta_1 z$ in order to simplify the equation which is called *nonlinear Schrödinger equation* (NSE). The right-hand side includes the nonlinear contribution of the propagation and was defined by the substitution

$$\Delta k_{NL} = n_2 \frac{\omega}{c} I = 2 n_0 \epsilon_0 n_2 \omega_0 |A|^2 \equiv \gamma |A|^2. \tag{4.14}$$

From equation 4.13 it can be seen that the second term on the left-hand side sums up all dispersive components which tend to broaden the pulse during propagation. However, the (nonlinear) term on the right-hand side can be of a form which exactly cancels out this dispersive influence in a way that the shape of the pulse is stable in time. Such a pulse is often termed *temporal optical soliton*[1]. The Nonlinear Schrödinger equation can be solved by the inverse scattering method as shown by Zakharov and Shabat[135] or numerically by the split step Fourier method[136].

[1]Solitary waves do not only occur in the case of electromagnetic wave packages. The first mention of a wave packet with stable shape was published in 1834 by John Scott Russel who discovered a solitary water wave while riding a horse for several kilometers beside a boat canal[134].

A solution for the NSE is depicted in equation 4.15a in the form of a hyperbolic secant ($\mathrm{sech}(x) = \frac{1}{\cosh(x)}$)

$$A(z,\tau) = A_0 \cdot \mathrm{sech}\left(\frac{\tau}{\tau_0}\right) e^{i\kappa z}, \tag{4.15a}$$

where A_0 and κ are defined as

$$|A_0|^2 = \frac{-\beta_2}{\gamma {\tau_0}^2} = \frac{-\beta_2}{2n_0\epsilon_0 n_2 \omega_0 {\tau_0}^2}, \tag{4.15b}$$

and

$$\kappa = \frac{-\beta_2}{2{\tau_0}^2} = \frac{1}{2}\gamma |A_0|^2. \tag{4.15c}$$

This solution is also called a *fundamental soliton* which does not change the shape during propagation[2]. In Fig. 4.2 a comparison between the sech^2-shape of an optical pulse (the square is due to the viewpoint of optical intensity) and the well-known Gaussian shape is shown which is the output of most common pulsed laser systems. From equation 4.15b it becomes clear that the group velocity dispersion β_2 and the nonlinear refractive index n_2 have to be of opposite sign in order to yield a positive intensity $|A|^2$. For most materials n_2 is positive (e.g. $n_2 = 2.19 \cdot 10^{-16}\ \frac{cm^2}{W}$ for fused silica at 1030 nm[137]) so an anomalous GVD is necessary to form a solitary wave.

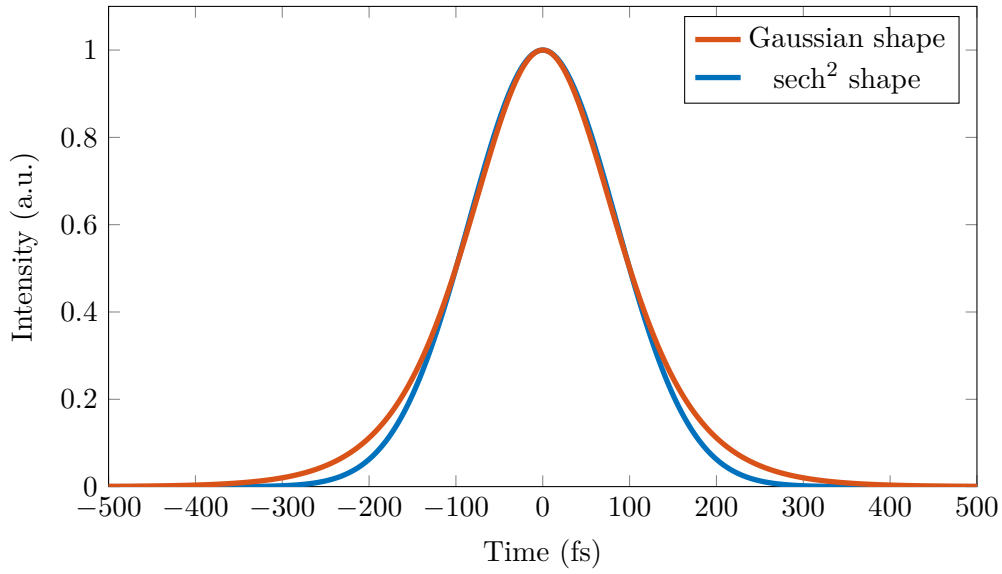

Figure 4.2: Comparison between a sech^2-pulse and a pulse with a Gaussian shape. Both pulse shapes have a FWHM of 200 fs.

[2]There are also higher-order solitons solving the NSE that exhibit a oscillating behaviour of their pulse shape. The type of the soliton depends on the initial pulse parameters like peak amplitude of the electrical field or temporal width. Further details can be found in the literature e.g. [129][132].

Solitons show a remarkable stability against perturbations of the fundamental shape. Even the initial pulse envelope does not necessarily have to exhibit the sech^2-form or has to be unchirped when launched into a nonlinear medium. After a certain propagation distance the pulse evolves into a stable soliton[138]. This effect is shown in Fig. 4.3 where a Gaussian shaped pulse is launched into a material suitable of solitary wave propagation. The peak amplitude, pulse width and shape change until the stable form of a sech^2-shaped pulse is reached.

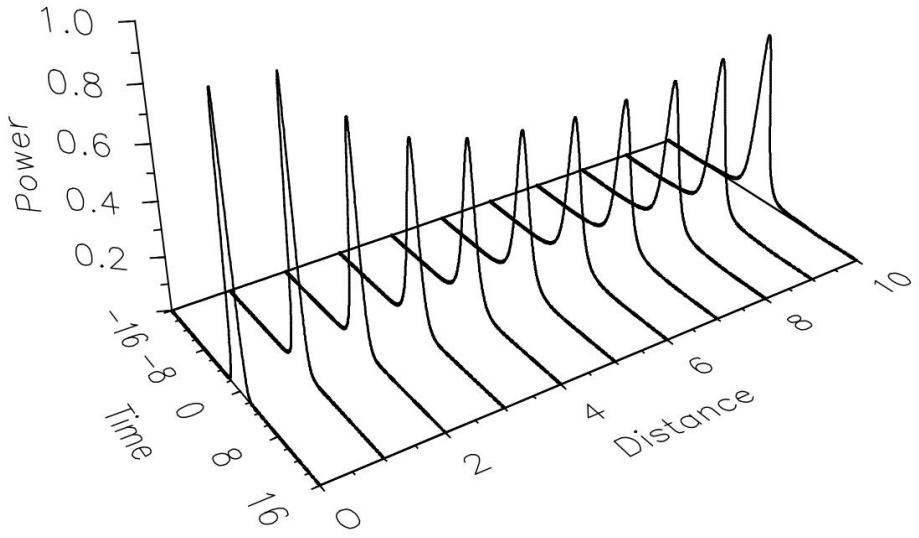

Figure 4.3: Reshaping of a initially Gaussian shaped pulse under the simultaneous effect of contrariwise acting SPM and second order dispersion leading to the formation of a fundamental soliton. Reprinted by permission from [139].

2.2 Soliton self-frequency shift

In 1986 the effect of soliton self-frequency shift (SSFS) was shown experimentally by Mitschke and Mollenauer at the AT&T Bell Laboratories[140]. They launched sub-picosecond pulses of variable average power at a center wavelength of 1.5 µm into a fiber with a length of several hundred meters and analysed temporal and spectral characteristics of the laser pulses after their propagation through the medium. When the pulse energy exceeded the soliton condition of the used fiber (see previous section) a satellite pulse was observed in the autocorrelation whose temporal delay to the main pulse increased with rise of the initial pulse energy launched into the fiber. In the optical spectrum an additional peak at the longer wavelength side of

the main peak appeared whose shift could be controlled by the energy of the initial pulse. The higher this value was chosen the more the satellite was shifted to the red.

This effect is attributed to stimulated Raman-scattering which is a nonelastic scattering process of photons with matter (in this case the silica fiber core). Silica fibers exhibit a substantially broad range of vibrational modes which is due to the amorphous nature of glass. The sharp vibrational molecular features overlap and create a continuous band which covers a frequency range up to 40 THz with a peak at 13.2 THz[141].

While propagation through the fiber the shorter wavelength part of the optical pulse spectrum overlaps spatially and temporally with the longer wavelength part due to the solitonic nature of the wave package. This leads to stimulated Raman-gain for the lower frequency part of the soliton spectrum at cost of the higher frequency part which experiences a Raman-loss. This leads to a constantly advancing red shift of the center wavelength of the pulse propagating along the fiber.

The first theoretical description was shown by Gordon in 1986 who treated the intrapulse Raman-effect as a perturbation of the NSE (see Fig. 4.13)[142]. There, the following formula for the frequency shift per propagation length $\frac{d\nu_0}{dz}$ was derived as follows:

$$\frac{d\nu_0}{dz} = -\frac{10^5 \lambda^2 D}{16\pi c {t_c}^3} \int_0^\infty \Omega^3 R(\Omega/2\pi t_c)/\sinh^2(\pi\Omega/2)\, d\Omega. \tag{4.16}$$

Here λ, D, c and t_c are in units of cm and ps. R is the normalized Raman-loss spectrum, t_c the pulse width in soliton units ($\tau_{\mathrm{FWHM}} = 1.763 t_c$) and D the dispersion parameter ($D = -\frac{2\pi c}{\lambda^2}\beta_2$). This expression can be approximated by the next formula assuming a wavelength λ of 1.50 µm and $D = 15$ ps/nm/km [142]:

$$\frac{d\nu_0}{dz} = 0.0436 \frac{h(\tau)}{\tau^4}. \tag{4.17}$$

Here the term $h(\tau)$ is mainly taking into account the Raman loss spectrum of the media (in this case a silica optical fiber) and was derived numerically. As it can be seen from equation 4.17 the pulse width τ has an exceptionally strong influence on the rate at which the mean frequency of the pulse is shifted to the longer wavelengths. This is depicted in Fig. 4.4 where the frequency shift $d\nu$ in dependence of the pulse width τ is shown for three different starting pulse parameters τ according to equation 4.17.

Equation 4.17 suggests a linear dependence on the propagation length of the frequency shift. This is reasonable for small deviations of the initial center frequency

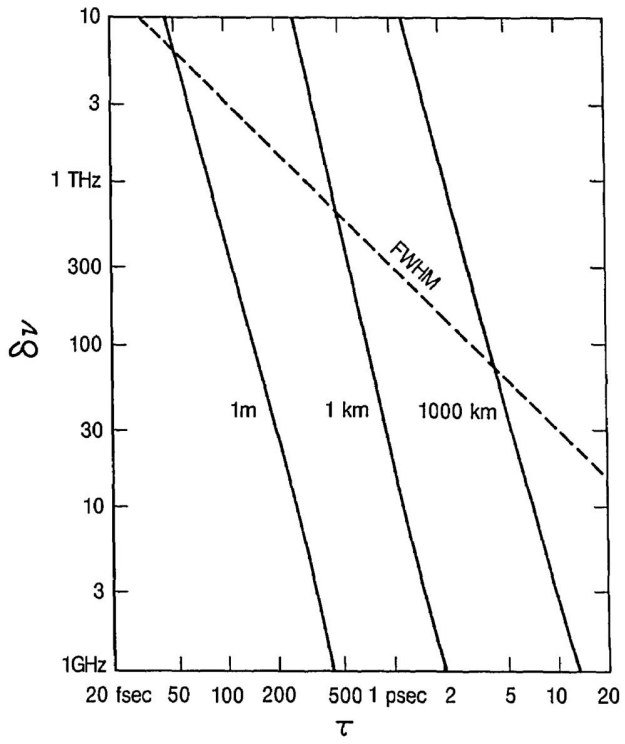

Figure 4.4: Frequency shift caused by soliton self-frequency shift in dependence of the pulse width for three different fiber lengths. For comparison the associated spectral pulse width is depicted as a dashed line. Reprinted by permission from [142]. © The Optical Society.

but this assumption deviates from measurements at large frequency shifts (see chapter 4.4). This is due to a wavelength dependence of the dispersion parameter D and changes in the soliton width due to variations of the pulse width, peak amplitude or nonlinearity of the guiding medium e.g an optical fiber.

2.3 Second harmonic generation

The nonlinear interaction of charge carriers in media with an incident intense light field leads to an anharmonic oscillation of the particles. This leads to frequency components different from the ones of the initial light field. By this interaction several effects like higher harmonics of a single incident frequency can occur as well as mixed frequencies in the case of different light waves propagating simultaneously. In the following the effect of second harmonic generation (SHG) will be derived as well as other three-wave-mixing processes (difference frequency DFG, sum frequency SFG and optical rectification OR) starting from the nonlinear induced polarisation

as seen in equation 4.4. Starting with an incident electrical field $E(z,t)$ consisting of two field components $E_1(z,t)$ and $E_2(z,t)$ the resulting field can be written in the form

$$E(z,t) = E_1 e^{i(k_1 z - \omega_1 t)} + E_2 e^{i(k_2 z - \omega_2 t)} + c.c.. \tag{4.18}$$

Here *c.c.* denotes the complex conjugated terms. Inserting this into equation 4.4 yields for the second order nonlinear polarisation P_2

$$P_2 = \epsilon_0 \chi^{(2)} (\underbrace{E_1^2 \cdot e^{2ik_1 z - 2i\omega_1 t} + E_2^2 \cdot e^{2ik_2 z - 2i\omega_2 t}}_{\text{SHG}} + \underbrace{2E_1 E_2 \cdot e^{i(k_1+k_2)z - i(\omega_1+\omega_2)t} + ...}_{\text{SFG+DFG+OR}} + c.c.). \tag{4.19}$$

The previous equation shows field components E_1^2 and E_2^2 oscillating at $2 \cdot \omega_1$ and $2 \cdot \omega_2$, respectively. In the following only the terms denoted SHG will be considered. This is reasonable due to different phase matching conditions of the different frequency mixing processes which will be shown later in this section. By inserting this into the wave equation (Eq. 4.12) one gets following terms describing the field amplitude of the second harmonic E_{SHG} (assuming $E_1 = E_2 \equiv E_0, k_1 = k_2 \equiv k_0$ and $2\omega_1 = 2\omega_2 \equiv \omega_{SHG}$):

$$\frac{\partial^2 E_{\text{SHG}}}{\partial z^2} + \frac{\partial E_{\text{SHG}}}{\partial z} \cdot 2ik_{\text{SHG}} = -\frac{2\omega_{\text{SHG}}^2}{c^2} \cdot \chi^{(2)} \cdot E_0^2 \cdot e^{2ik_0 z} \cdot e^{-ik_{\text{SHG}} z}. \tag{4.20}$$

Here the complex conjugated term was neglected without loss of generality and the amplitude of the incident wave E_0 was assumed to remain constant while propagation. In the *slowly varying amplitude approximation* the amplitude of the electromagnetic wave is considered to stay almost constant over one oscillation of the electric field:

$$\left| \frac{\partial^2 E_{SHG}}{\partial z^2} \right| \ll \left| \frac{\partial E_{SHG}}{\partial z} \cdot k_{SHG} \right|. \tag{4.21}$$

With that a formula for the evolution of the field amplitude of the second harmonic can be derived:

$$\frac{\partial E_{SHG}}{\partial z} = \frac{i\omega_{SHG}^2}{c^2 \cdot k_{SHG}} \cdot \chi_{(2)} \cdot E_0^2 \cdot e^{i\Delta k \cdot z}. \tag{4.22}$$

Here Δk denotes the difference between the fundamental wave vector and the wave vector of the SHG as $\Delta k = 2k_0 - k_{SHG}$ and is called *wave vector mismatch*.

By integration over z the field amplitude of the SHG after propagation over the length L in the nonlinear medium can be derived:

$$E_{\mathrm{SHG}}(L) = \frac{i\omega_{\mathrm{SHG}}^2}{c^2 \cdot k_{\mathrm{SHG}}} \cdot \chi^{(2)} \cdot E_0^2 \int_0^L e^{i\Delta k z}\, dz = \frac{i\omega_{\mathrm{SHG}}^2}{c^2 \cdot k_{\mathrm{SHG}}} \cdot \chi^{(2)} \cdot E_0^2 \cdot \left(\frac{e^{i\Delta k L} - 1}{i\Delta k} \right). \quad (4.23)$$

From the term in brackets in the previous equation it can be seen that the field amplitude $E_{SHG}(L)$ is oscillating in the imaginary plane with constant vector length for the case of a non-vanishing wave vector mismatch. This leads to very low reachable intensities of the SHG because there is an oscillating flow of energy between the fundamental wave and the second harmonic wave. By adjusting Δk in a way that it vanishes, it is possible to reach considerable high efficiencies of the energy transfer to the SHG. This is called *phase matching* and can be done exploiting birefringence or quasi-phase matching (as will be seen in chapter 4.4). With $I = 2n\epsilon_0 c|E|^2$ an expression for the intensity of the SHG can be deduced:

$$\boxed{I(L) = \frac{\omega_{\mathrm{SHG}}^2 \cdot \chi^{(2)2} \cdot I_0^2}{2n_{\mathrm{SHG}} \cdot n_0^2 \epsilon_0 \cdot c^3} \cdot L^2 \cdot \mathrm{sinc}^2 \left(\frac{\Delta k L}{2} \right).} \quad (4.24)$$

Here $\mathrm{sinc}(x)$ stands for $\sin(x)/x$ and I_0 denotes the intensity of the incident wave. The value of the wave vector mismatch is crucial for the intensity of the second harmonic generation as can be seen in Fig. 4.5. For the case of a perfect phase matching ($\Delta k = 0$) the intensity of the second harmonic depends linearly on the propagated distance in the material and quadratically on the intensity of the fundamental wave. Technically perfect phase matching can be realized by birefringent materials and perpendicular polarized fundamental and second harmonic light. However, this is only possible for materials showing a non-vanishing value of the corresponding tensor element of the nonlinear susceptibility. Another possible way to reach nearly perfect phase matching is by making use of the so called *quasi phase matching*. In this case the direction of the nonlinearity of the material is flipped after a certain propagation distance (*coherence length* $l_c = \frac{\pi}{\Delta k}$). This length indicates the distance after which the phase slipping equals π and leads to an energy flow back into the fundamental wave. By flipping the direction of the nonlinearity (generally by inverting the crystalline structure of ferroelectric materials like Lithiumniobate) an additional phase offset of π is introduced which counteracts the phase mismatch and ensures a steady flow of energy into the second harmonic.

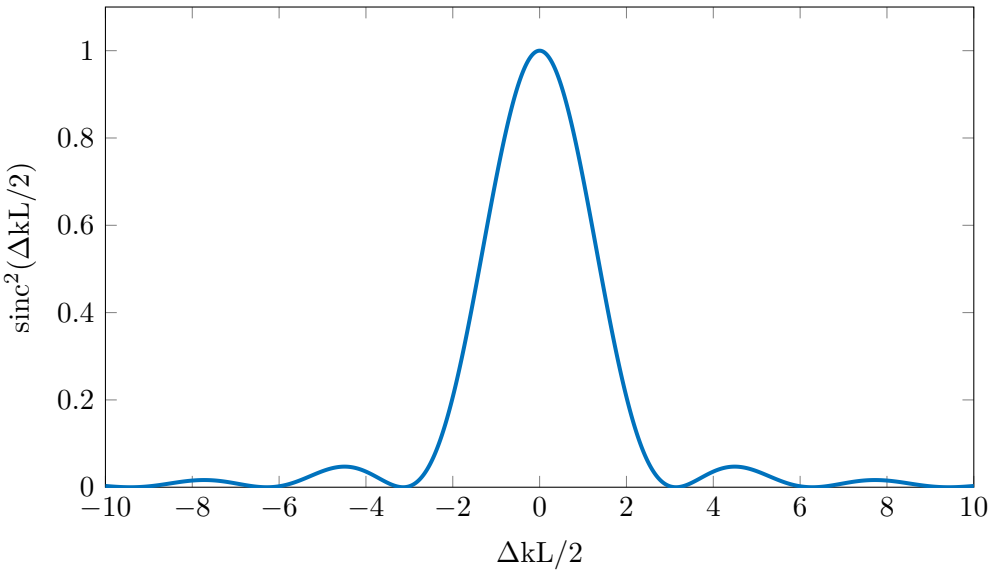

Figure 4.5: Dependency of the conversion efficiency to the second harmonic ($I \sim \mathrm{sinc}^2(\Delta kL/2)$ of the wave vector mismatch Δk.

3 Relative intensity noise

Sensitive measurements based on the detection of intensity changes of a laser beam as stimulated Raman scattering (SRS)[143] or TiSCAT rely on minimizing the intensity noise influences of the experiment. Sources for intensity noise (often quantified as *relative intensity noise*, RIN) are influencing different parts of the noise spectrum. Thermal fluctuations of the laser power are extremely slow and have negligible influence on the outcome of experiments on the time scales of seconds, yet they can have a critical impact on the adjustment of the setup. Mechanical disturbances like vibrations and sound waves cause noise mainly in the lower kHz-regime[144]. Electrical noise of control electronics as well as noise of pump laser sources can be translated into intensity noise of the whole laser system[145] such that the noise of laser amplifiers is mainly determined by the noise characteristics of the pump laser for low frequencies in the order of tens of kHz[146].

High-frequency intensity noise (also sometimes called *flicker noise*) is mainly given by a $1/f$-dependence[147]. Thus, it is strongly decreasing for frequencies above the influence regions of mechanical and electrical disturbances. This is the main reason for lock-in detection schemes at high frequencies as the noise can reach the so called *shot-noise-limit*. This is the limit of intensity detection sensitivity given by the Poisson distribution of the detected photons.

The most common way to determine the relative intensity noise (RIN) of a light

source is by expressing it as the ratio of noise power for a measurement bandwidth of 1 Hz normalized by the average signal power in form of a power spectral density PSD[148]. It is defined as

$$\mathrm{PSD}(f) = \frac{\langle \Delta P(f)^2 \rangle}{P^2}. \tag{4.25}$$

Here $\langle \Delta P(f)^2 \rangle$ denotes the mean-square optical intensity fluctuation for a bandwidth of 1 Hz at a specified frequency and P the average optical power. Usually, this value is given in the unit 1 [dBc/Hz] and can be understood as the *intensity fluctuation in the bandwidth of one Hertz*. The measurement can be carried out by detecting the laser intensity via a fast photodiode, computing the measured optical power and Fourier-transforming the signal in its frequency components with a frequency analyzer[149]. To minimize noise influences of the electronic system and the shot-noise-level which is power dependent the attenuation of the power should be as low as possible.

The spectrally resolved measurement is useful identifying distinct frequencies of high noise levels which should be avoided as modulation frequency of the lock-in detection scheme of the experiment. The rms value of the RIN can be derived via integration over the noise spectrum in the frequency range $[f_1, f_2]$ and is commonly given in percent:

$$\mathrm{RIN}_{\mathrm{rms}} = \sqrt{\int_{f_1}^{f_2} \mathrm{PSD}(f)\, df}. \tag{4.26}$$

4 System overview and characterisation

In the following an overview of the whole fiber laser system is given and important measurements and characteristics of the instrument are shown.

Figure 4.6 depicts the composition of the components of the laser. The starting point is an all-fiber oscillator modelocked by a semiconductor saturable absorber mirror (SESAM). The SESAM exhibits an intensity dependent loss leading to favourable amplification of short pulses and thus modelocking of the laser oscillator. Further details about the mechanisms of this semiconductor device can be found in the literature e.g. [150]. The oscillator pumped by fiber coupled laser diodes emits pulses at a repetition rate of 80 MHz and a center wavelength of 1560 nm. After that the fiber output is split into two portions each seeding an amplifier arm. These are necessary for pump-probe experiments.

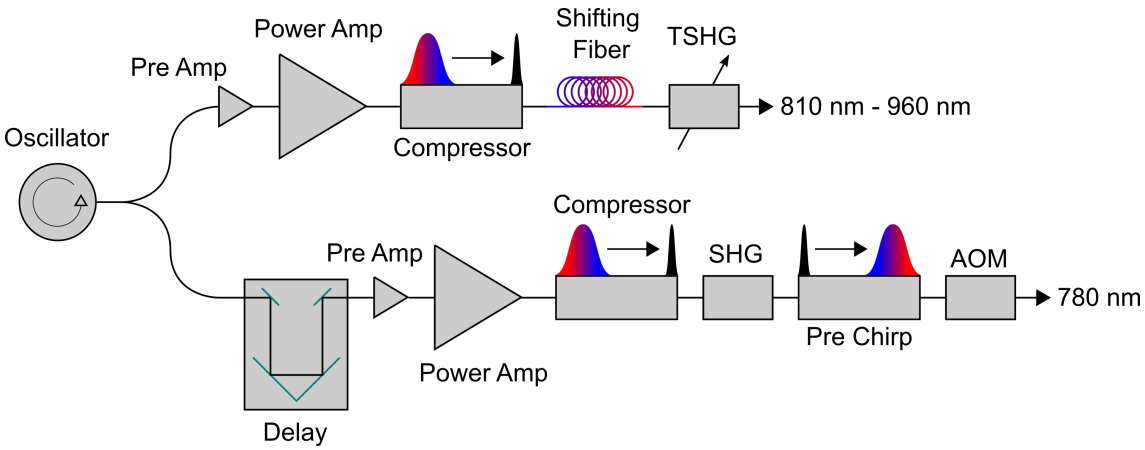

Figure 4.6: Overview of the essential optical components of the fiber laser system. Starting on the left side the pulses emitted from the oscillator are split into the pump arm (bottom path) and the probe arm (top path). Detailed information is given in the text. Reprinted with permission from [151] © Optical Society of America.

Pump arm

For time resolved pump-probe experiments it is an indispensable requirement that the pulses of both arms can be delayed in time with high accuracy and without distortion of the beam pointing or other pulse characteristics which would lead to deviations in the measurement. In this system a fiber coupled step motor driven delay stage capable of a maximal temporal delay of 500 ps is utilized. It is inserted behind the oscillator in order to minimize nonlinear effects arising due to long fiber lengths in the subsequent high-power section of the laser which would impair the pulse quality.

The pulses are then amplified in a chirped pulse amplification (CPA) system. This technique invented by Strickland and Mourou in 1985[152], recently honored with the Nobel price in physics 2018[153], dramatically increased the peak intensities accessible with pulsed laser systems. There, an initially short pulse is temporally stretched up to several orders of magnitude of its previous pulse length lowering its peak intensity to a fraction of the initial value[154]. This prevents the pulse from strong nonlinear effects during propagation and amplification to high powers, conserving the initial pulse quality while amplification. After transmission trough the amplifier the pulse is then recompressed to exhibit a short pulse width.

In the present fiber laser system the pulses are spectrally chirped and pre-amplified first to reach the pulse intensities necessary for an efficient amplification in the all-fiber power amplifier as this is an stimulated effect enhanced by higher initial

light intensities. In the subsequent compressor the pulse is then compressed to the minimal pulse length. After this amplification to roughly 25 nJ pulse energy the pulses are then doubled in frequency to a center wavelength of 780 nm by second harmonic generation (SHG) in a periodically poled lithium niobate crystal (see chapter 4.2.3). The pulse width of the nearly unchirped pulse is approximately 90 fs (FWHM).
In the next step the pulses are pre-chirped to account for the chromatic dispersion of the acousto-optic modulator (AOM) and the microscope objective, both exhibiting high amounts of group delay dispersion (GDD). The group delay dispersion is calculated as the group velocity per unit length (see chapter 4.2.1) and is for these two optical elements in the order of +8000 fs^2 (normal dispersion) in sum. Assuming an unchirped pulse exhibiting a Gaussian shape the pulse length τ after a certain value of group delay dispersion can be calculated as [155]:

$$\tau = \tau_i \sqrt{1 + \frac{16\ln(2)^2 \cdot \mathrm{GDD}^2}{\tau_i^4}}. \tag{4.27}$$

Here, τ_i denotes the initially unchirped pulse width. For the present case a Gaussian pulse with a length of 90 fs (FWHM) experiencing a group delay dispersion of $\pm$8000 fs^2 would be lengthened to 262 fs (FWHM). This would lower the temporal resolution of the experiment drastically. By introducing the pre-chirp of the same amount but reverse sign, the pulse is shortest after propagation through the mentioned optical elements and at the sample position; thus, it yields a better temporal resolution of the experiment.
This is shown in Fig. 4.7 based on the measurement of the cross-correlation of pump and probe arm at the position of the sample. Here, nanoscale crystals of iron iodate were used for sum frequency generation as they exhibit a strong nonlinear response of second order even in form of nanocrystals[156]. The Gaussian fit function exhibits a width of 285 fs (FWHM) which is longer than the theoretically predicted value of 178 fs (FWHM) by a factor of 1.6. For this the convolution of two Gaussian functions with the widths of 90 fs for the pump pulse (assumed to be bandwidth-limited) and 243 fs for the probe pulse (initially 90 fs lengthened by the propagation through the objective) were assumed.[3] This deviation could be caused by the underestimation of the chromatic dispersion of the objective or the influence of other optical components in the beam path.

[3]The convolution of two normal distributions again results in a normal distribution with a mean value and variance which can be calculated by the sum of the corresponding values of the initial functions[157, suppl.mat.].

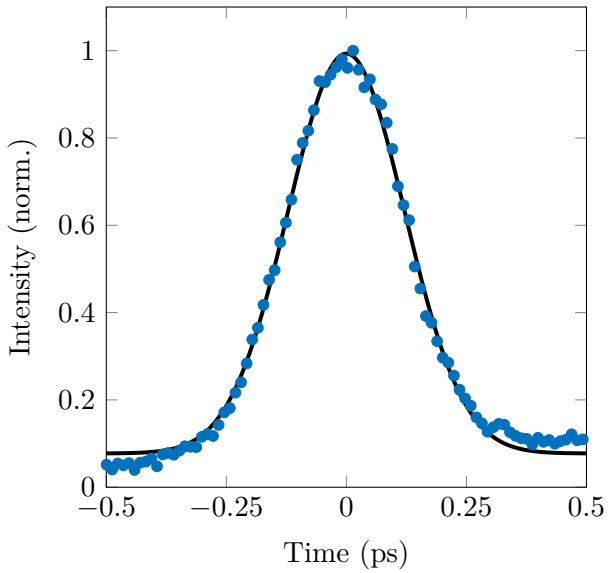

Figure 4.7: Cross-correlation of pump and probe arm at the focal position of the microscope. The signal was achieved by detection of the sum frequency generation on iron iodate crystals. A Gaussian fit with a width of 285 fs (FWHM) is depicted in black. Adapted with permission from [151] © Optical Society of America.

The mentioned acousto-optic modulator is utilized for the lock-in detection scheme of the TiSCAT experiment and can be modulated up to 1 MHz. Additionally, it can be used to continuously attenuate the average pump power which is up to approximately one Watt.

Probe arm

The probe arm is amplified in the same way as the pump arm. After the temporal compression the pulses are coupled into a single mode fiber. Because of the high peak intensity of the pulses a soliton is formed propagating with a stable temporal pulse shape (see chapter 4.2.1). This leads to the soliton self-frequency shift which was already introduced in chapter 4.2.2 moving the center wavelength of the pulse starting from 1560 nm to longer wavelengths.

By adjusting the length of the shifting fiber the spectral endpoint at maximum power of the amplifier can be determined and was adjusted to reach a wavelength of 1920 nm. The spectral peak position can then be shifted to the blue by lowering the gain of the power amplifier. This can be seen in Fig. 4.8 for three exemplary spectra and in Fig. 4.9 for a series of different power levels of the amplifier. The spectra show the wavelength-shifted solitons in the area around approximately 1800 nm

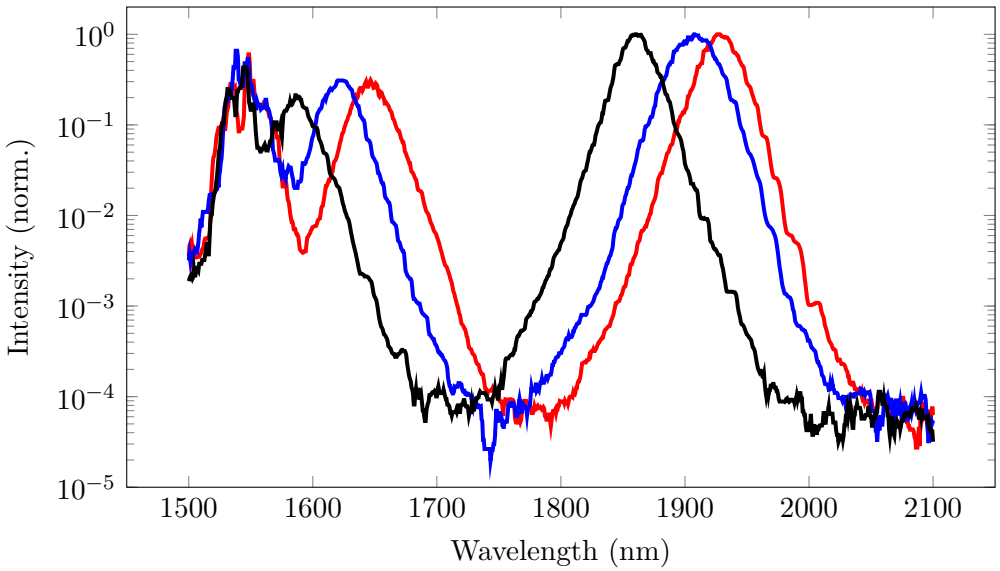

Figure 4.8: Exemplary normalized spectra of the laser for three different power levels after undergoing the soliton self-frequency shift. The power increases for the depicted measurements with line colors from black (lowest power) to red (highest power).

whose peak position is dependent on the power coupled into the fiber (from low-power to high-power: black, blue, red). At 1560 nm residual light of the fundamental pulse can be identified[122] which could be traced back to an imperfect pulse shape of the initial pulse.

At approximately 1620 nm additional peaks can be observed. Here additional solitons form for higher initial pulse energies which are shifted in their center wavelength due to the SSFS. This is in agreement with previously reported experiments[158]. These contributions are filtered out by the subsequent frequency doubling which is phase matched for the longer wavelengths.

Figure 4.9 shows the dependence of the soliton center wavelength on the power coupled into the shifting fiber. Differing from the theoretical predictions (see Eq. 4.17 in chapter 4.2.2) the measurement does not follow a linear behaviour but shows a saturation effect for higher powers. This has already been reported[158] and is attributed to several effects: The stimulated effect of Raman-scattering leads to a continuous loss of pulse energy to the lattice vibrations and thus to a decrease of peak intensity strongly affecting the SSFS. Additionally, higher order solitons are created at higher input powers draining energy from the initial pulse and slowing down the SSFS[119]. Furthermore, starting at approximately 1800 nm additional loss is attributed to residual water in the silica fiber[158].

The area over which the intensity of the fiber guided laser beam decays to $1/e^2$

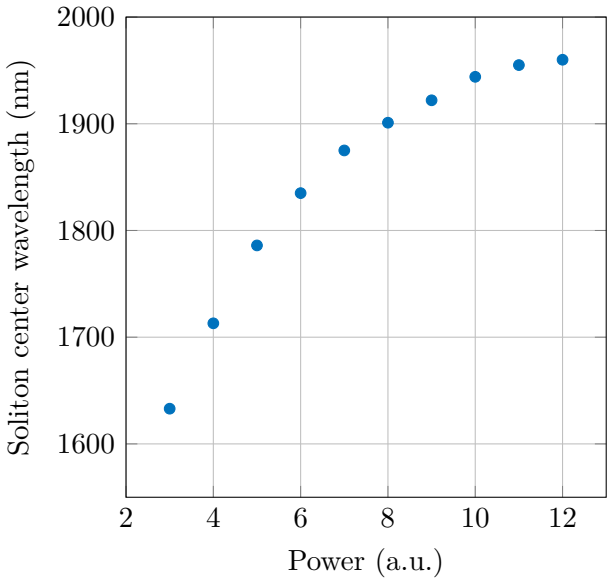

Figure 4.9: Dependency of the shifted soliton center frequency on the average pulse power coupled into the shifting fiber.

is called *mode field diameter* (MFD). It gives an important factor determining the peak intensity of the laser pulses inside the fiber and is thus a significant influence on the soliton self-frequency shift. For a given step-index fiber the MFD decreases with increasing wavelength for single-mode propagation[124]. This can slow down the SSFS for higher wavelengths additionally.

The group velocity dispersion is dependent on the center wavelength of the pulse (see section about chromatic dispersion in 4.2.1) and thus the soliton parameter like pulse width and peak intensity as well. This leads to different soliton pulse parameters during the process of the SSFS having influence on the wavelength-shift.

After the SSFS, covering the spectral region between 1620 nm and 1920 nm, the pulses are frequency doubled covering all wavelengths between 810 nm and 960 nm. This is carried out in a periodically poled lithium niobate (PPLN) crystal with adjustable phase matching in order to achieve maximum conversion efficiency for all wavelengths. With this technique over 50% of the pulse energy is transferred to the second harmonic yielding an average power between 80 mW and 280 mW which is dependent on the adjusted center wavelength of the wavelength-shifted pulses.

The achieved spectral pulse shape is depicted in Fig. 4.10 for five exemplary center wavelengths. The bandwidth is approximately 13 nm (FWHM) for the example of pulses at 930 nm which translates into a bandwidth limited temporal width of 76 fs for the measured spectrum. Figure 4.11a shows the interferometric autocorrelation (IAC) taken at this center wavelength. Making use of the IAC and the measured

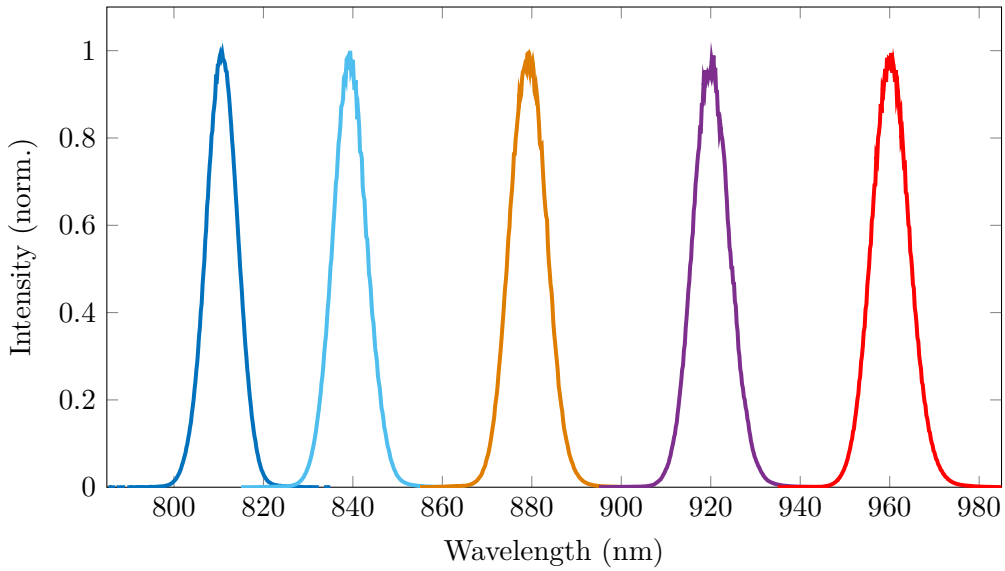

Figure 4.10: Exemplary normalized spectra of the laser after frequency doubling covering the spectral range between 810 nm and 960 nm.

spectrum, the temporal pulse shape can be reconstructed. This was carried out with the pulse propagation simulation program *SSFTprop*[159] and is shown in Fig. 4.11b. The retrieved pulse shape exhibits a temporal width of 90 fs (FWHM) which is close to the associated transform-limited pulse width of 76 fs. The deviation may be due to optical elements in the beam path introducing chromatic dispersion.

Residual fundamental light as well as higher order solitons are filtered out with an appropriate short-pass filter. An important property of the probe arm are the intensity noise characteristics (relative intensity noise, RIN, see chapter 4.3) as the accessible TiSCAT sensitivity is limited by the noise of the experimental setup including the detection section as well as the excitation source. The whole fiber laser system is enclosed in a metal housing ensuring best shielding from environmental influences leading to misalignment or additional RIN. To prevent thermal load of the optical components as much as possible, heat generating electronics like the AOM-driver electronics are located in a separated box as well as the pump diodes of the power-amplifiers which are fed into the laser head by optical fibers. The stability of the free-space components like the SHG-focusing unit is ensured by active thermal control via Peltier elements. This was verified by a test measurement over 65 hours at a center wavelength of 900 nm. There a mean power of 166.0 mW with a maximum deviation of 1.3 mW (translating to 0.78%) was measured. The stability of the center wavelength was determined by simultaneous measurement of the spectrum every 30 seconds via an optical spectrum analyzer. Here the value

of the maximum deviation was found to be 0.35 nm. The influence of RIN to the signal-to-noise ratio of the TiSCAT measurement will be demonstrated in chapter 6 including a spectrally resolved RIN measurement of the involved laser sources.

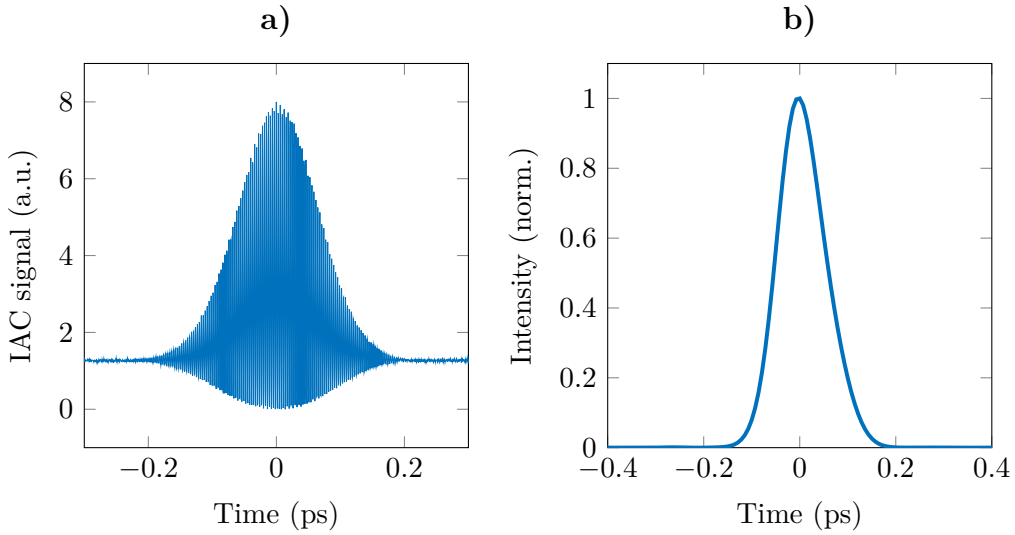

Figure 4.11: **a)** Interferometric autocorrelation of the frequency doubled pulse at a center frequency of 930 nm. **b)** Utilizing the interferometric autocorrelation and the optical spectrum, the pulse shape at the center wavelength of 930 nm can be retrieved. This was done with the simulation software *SSFTProp* with kind permission of Robert Herda[159]. This yields a pulse width of 90 fs (FWHM) which is close to the associated transform-limit of 76 fs.

Both outputs of the laser system are spatially separated to make future external manipulations like an additional frequency doubling of the pump arm possible. The beam combining of pump and probe arm is then realized by overlapping both beams via an 50/50-splitter. The beam diameter of both arms is approximately 1 mm which is not sufficient for an adequate filling of the back aperture of the microscope objective. To accomplish this, a beam expansion system with achromatic lenses (f=19 mm/f=125 mm) is located behind the beam combiner.

Delay position of the temporal overlap

TiSCAT measurements were carried out to identify the position of the mechanical delay where both arms temporally overlap. It was found that this position is approximately linearly dependent on the probe arm center wavelength adjustment as seen in Fig. 4.12. This is attributed to different values of group velocity dispersion experienced by the wavelength-shifted solitons at different center frequencies of the probe arm. The linear approximation was used in the following TiSCAT measurements for the initial delay adjustment.

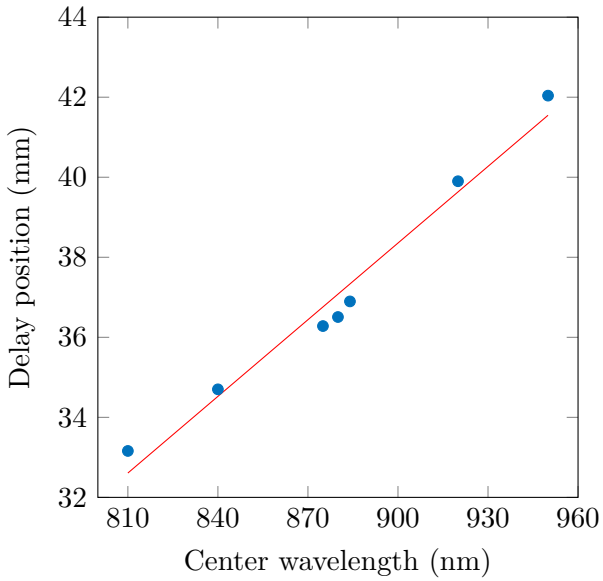

Figure 4.12: Dependency of the center wavelength on the delay position of the fiber laser.

Chapter 5

Measurements on single (6,5) SWCNTs

The following chapter is based on the paper *"Probing the ultrafast dynamics of excitons in single semiconducting carbon nanotubes"* that has been published in *Nature Communications* 13.1 (2022) [160].

The sample material containing the polymer-wrapped (6,5) SWCNTs was provided by the group of Prof. Dr. Tobias Hertel from the Julius-Maximilians-Universität Würzburg.

This chapter reports on the exciton dynamics of single semiconducting (6,5) single-walled carbon nanotubes using transient interferometric scattering (TiSCAT) and time-resolved photoluminescence measurements utilizing time-resolved single photon counting (TCSPC). Whereas time-resolved PL detection by single-photon counting provides a direct and highly sensitive tool for monitoring the population of emissive states in the ps to ns range it lacks the temporal resolution needed to analyze the very early decay processes. Transient absorption spectroscopy, on the other hand, easily reaches into this sub-ps regime but typically suffers from limited detection sensitivity. As shown before, the TiSCAT technique is capable of detecting even smallest particles. Using the confocal microscopy setup shown in chapter 3.2, it will be shown that pump-probe transients and PL transients for the same SWCNTs can be used to get a unified model of the involved processes.

Furthermore, Monte-Carlo simulations will emphasize the role of localization sites occurring in single SWCNTs deposited on substrates strongly affecting their decay dynamics.

1 Photoluminescence microscopy

The (6,5) SWCNT sample material was spincoated on a glass cover slide which was covered with a thin layer of polystyrene to prevent quenching of the nanotubes caused by the glass substrate[161]. The amount of SWCNT-solution was chosen in a way to end up with an appropriate sample density of approximately one nanotube per 10 μm^2. This was verified via PL microscopy utilizing the Coherent Mira900 as light source. Here the nanotubes were excited by pulsed excitation at a wavelength of 880 nm and the PL emission was detected with an APD detector after a longpass filter centered at 900 nm to remove residual pump light of the laser excitation. To prevent the sample material from photodamaging the incident laser power was set to approximately 1.5 µW at the position of the sample. A typical PL-scan is shown in figure 5.1 with a scan range of 20x20 μm^2.

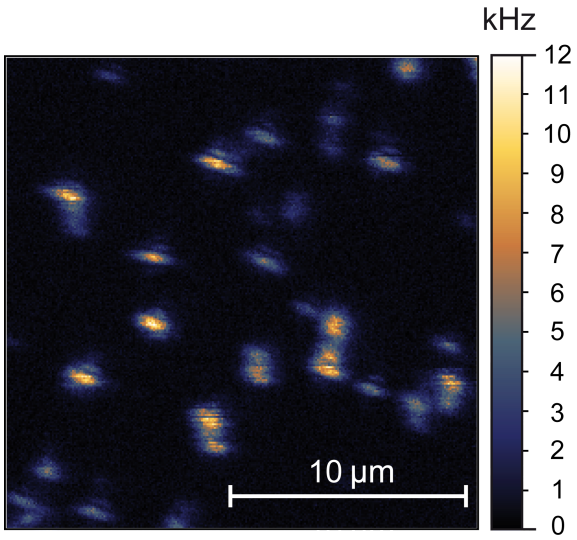

Figure 5.1: Photoluminescence (PL-) image of a sample area covered with single semiconducting (6,5) SWCNTs.

As there are different chiralities of semiconducting SWCNTs present in the raw material before separation, the type of nanotube was determined by PL spectroscopy as shown in Fig. 5.2a for an exemplary single nanotube. The single emission peak centered at 1000 µm indicates the E_{11} emission line of (6,5) SWCNT as been previously shown for nanotubes covered in PFO-BPy[162]. An absorption measurement of the chirality separated solution was performed by the group of Prof. Tobias Hertel and is shown in Fig. 5.2b. This ensemble measurement emphasizes the predominant existence of (6,5) SWCNTs in the solution as the absorption peak of the E_{11} state is most prominent at a wavelength of 1000 µm.

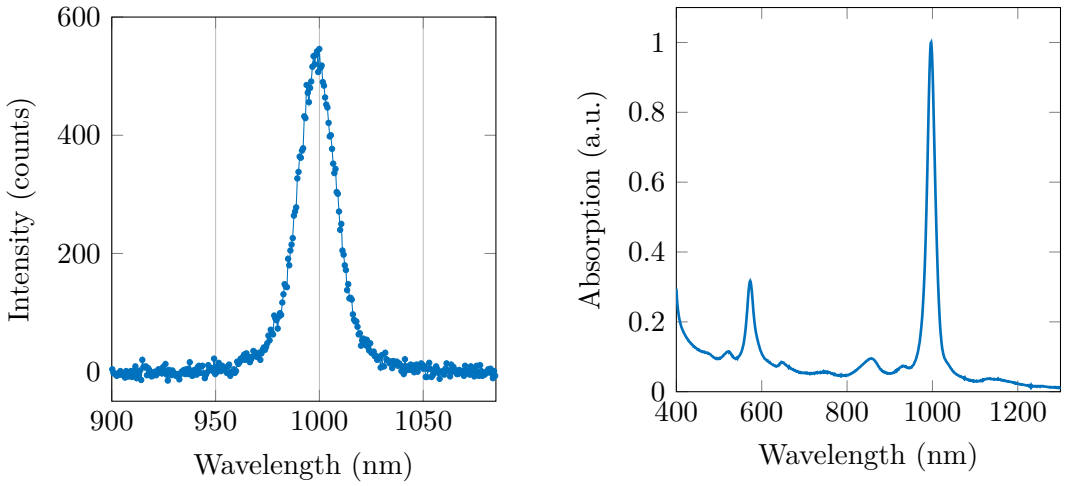

(a) PL spectrum.

(b) Absorption spectrum.

Figure 5.2: a) PL spectrum of a single (6,5) SWCNT and b) absorption spectrum of the corresponding raw solution taken by the group of Prof. Dr. Tobias Hertel.

The spectral emission profile was measured for a total amount of 43 single nanotubes and their center wavelengths were determined by fitting a Lorentzian function to the data. No emission wavelengths other than expected for the (6,5) SWCNTs were observed as depicted in the histogram in Fig. 5.3. The mean center wavelength was determined to be at 1002 nm whereas slightly shifted peak positions were observed as well. This can be due to variations of the environmental conditions of the nanotubes as the energies of the excitonic states are highly sensitive to their surroundings (see chapter 2). Defect sites alonge the nanotube cause variations in the excitonic energy landscape as well, leading to differences in PL emission energy. This was previously observed in high-resolution near-field measurements of SWCNTs[163].

2 Connection of photoluminescence and TiSCAT dynamics

The detection of spontaneous PL emission of single nanotubes via TCSPC is a widely used technique for the investigation of decay dynamics with highest sensitivity[56, 57, 69, 164]. However, as stated earlier, the initial decay dynamics happening at times well below several picoseconds cannot be resolved utilizing this technique and thus remain hidden. On the other hand, ultrafast pump-probe schemes determin-

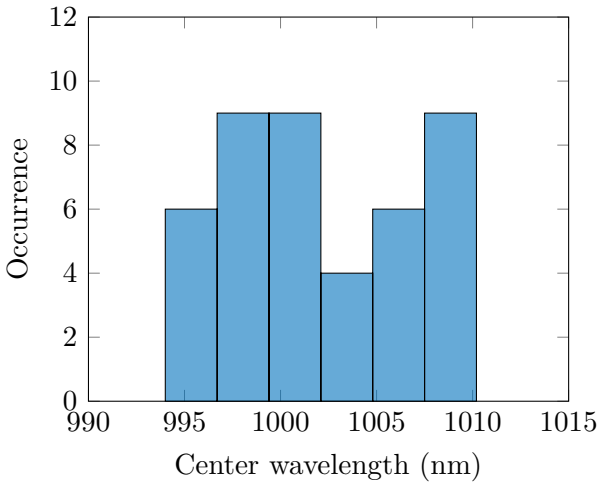

Figure 5.3: Histogram of the photoluminescence center wavelengths measured for a total of 43 SWCNTs whose chirality was identified as (6,5).

ing the relative changes of the absorption with an outstanding temporal resolution usually lack of the sensitivity necessary for single particle detection. Nevertheless, transient absorption measurements have been already carried out on individual SWCNTs with larger diameters in the range of 1.1 to 2.1 nm[161].

Interferometric scattering (iSCAT, see section 3.1.2), however, is capable of detecting smallest particles as has been shown for single molecules and semiconductor nanocrystals in special implementations[165, 166]. Significant discrepancies between the models derived from time-resolved PL and transient absorption studies seem to have emerged whereas a unifying picture appears to be lacking. On the one hand, this could be attributed to the lower time-resolution of TCSPC which is not able to reveal the early excited state dynamics in single nanotubes and on the other hand could result from the possibility of overlapping signal contributions in transient absorption in particular in the presence of multiple (n,m) species.

Observing the same single SWCNT at the same experimental conditions avoids ambiguities arising from the presence of different species (n,m) and nanotube to nanotube variations. Experiments on the same nanotube using the two complementary techniques allow for the unification of pump-probe and time-resolved PL model systems.

Figure 5.4 shows a single (6,5) SWCNT which was investigated via PL microscopy (Fig. 5.4a) and TiSCAT microscopy (Fig. 5.4b) as well. Excitation was done via the Ti:Sa setup adjusted to a pump wavelength of 880 nm which is a non-resonant case[167, 168] leading to a fast population of the E_{11} excitonic state by intraband relaxation[44]. Resonant probing is done at a center wavelength of 1000 nm by

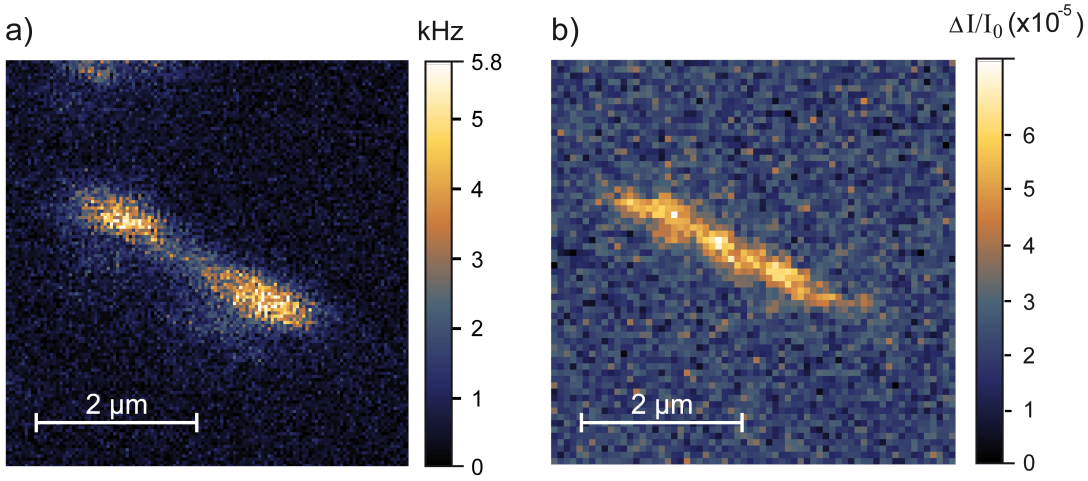

Figure 5.4: a) Confocal photoluminescence and b) transient interferometric scattering image of a single (6,5) SWCNT on glass covered with a thin layer of polystyrene. Modified from [160] under creative commons license CC BY 4.0 (`http://creativecommons.org/licenses/by/4.0/`).

making use of a corresponding bandpass filter after the supercontinuum generation with a spectral width of 10 nm (FWHM). For further evaluation of the measurement results it is important to point out that for PL and TiSCAT the same excitation parameters where chosen, leading to the same carrier dynamics in the single nanotubes. To prevent the single SWCNTs from photobleaching the pump power was set to a power level of 2 µW at the position of the sample. This corresponds to $2.3 \cdot 10^5$ photons per pulse at a repetition rate of 76 MHz and a duty cycle of 50% of the AOM modulation. For the TiSCAT measurement the probe power was set to 1 µW which translates to a photon number of $6.5 \cdot 10^4$ per pulse. Both images in Fig. 5.4 show the same nanotube with a length of approximately 2.2 µm. Remarkably, the nanoobject is not visible in the in the simultaneously recorded elastic scattering image due to the dominating background contribution resulting from the reflection at the glass-air interface. This points out the purpose of the pump-probe scheme which eliminates the constant background contribution of the reflection and additionally gives the possibility to investigate pump induced changes of the absorption of the nanoobject.

In the TiSCAT image the nanotube renders a positive signal which corresponds to a transient reduction of absorption (see Eq. 3.9 on page 32). This is in agreement with the observation of ground state bleaching (GSB) in the absorption spectrum of the SWCNTs in solution (see Fig. 5.2b). The observed signal contrast can thus be assigned to Pauli-blocking caused by the creation of E_{11} excitons. Addition-

ally, besides GSB a positive signal contribution is expected to arise from stimulated emission (STE) of E_{11} excitons due to the negligible Stokes-shift present in semiconducting SWCNTs[169]. Both signal contributions are thus not distinguishable in this measurement as they exhibit strong spectral overlap. Further excitation of the initially formed excited states would lead to a negative TiSCAT signal contribution as this increases absorption at the probe wavelength. This was not found in the course of this work for SWCNTs and can be attributed to a insignificant signal contribution of the higher lying states to the TiSCAT signal.
The exciton decay dynamics were explored by recording both TiSCAT and PL signal transients for a total of 18 (6,5) SWCNTs as depicted for two different nanotubes in Figs.5.5a/5.5b (TCSPC) and Figs.5.7a/5.7b (TiSCAT). Both measurement methods reveal differences in the decay dynamics of the individual SWCNTs which can be explained by a number of factors such as different defect densities and nanotube lengths[56, 57, 69, 168]. Additionally, the very fast decay is influenced by many-body effects such as EEA which will be discussed below.

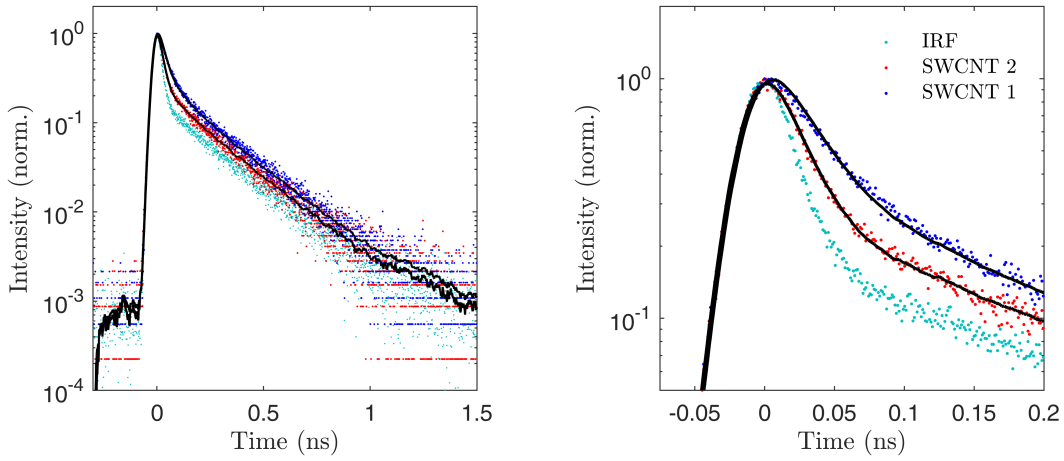

(a) Full range. **(b)** Zoom-in.

Figure 5.5: TCSPC transients of two (6,5) SWCNTs with the corresponding fit depicted in black. The instrument response function (IRF) is shown in turquoise.

The PL data of the measured transients was fitted by the model function suggested by Srivastava and Kono which was already introduced earlier in this work (Eq. 2.23, page 20)[65]:

$$n_A(t) = \frac{\exp(-\gamma t)}{1-\nu}\left[\exp\left(\frac{1-\nu}{\nu}\gamma t\right)\operatorname{erfc}\left(\sqrt{\gamma t/\nu}\right) + \sqrt{\nu}\operatorname{erf}(\sqrt{\gamma t}) - \nu\right]. \tag{5.1}$$

It combines the early influence of EEA as well as the mono-exponential decay of the single excitons for later times. In the equation γ denotes the sum of the radiative and non-radiative decay rates and $\nu = \tau_D/\tau_{\text{exp}}$ the ratio of the diffusional time τ_D and the exponential lifetime τ_{exp}. The diffusional time constant τ_D represents the time scale of exciton diffusion finally resulting in EEA. As seen in the figure the fit works well for the PL transients although it exhibits an ambiguity in the fast decay component which cannot be resolved due to the limited temporal resolution of the TCSPC measurement. So, as expected, the PL data can be described by a mono-exponential decay function as well yielding comparable results in the exponential decay time τ_{exp}. The distribution of this temporal component is depicted in the histogram in Fig. 5.6 and is in agreement with previously reported values[57, 168]. Analysis of the data was carried out via convolution of the IRF and the model function and fitting to the measured data.

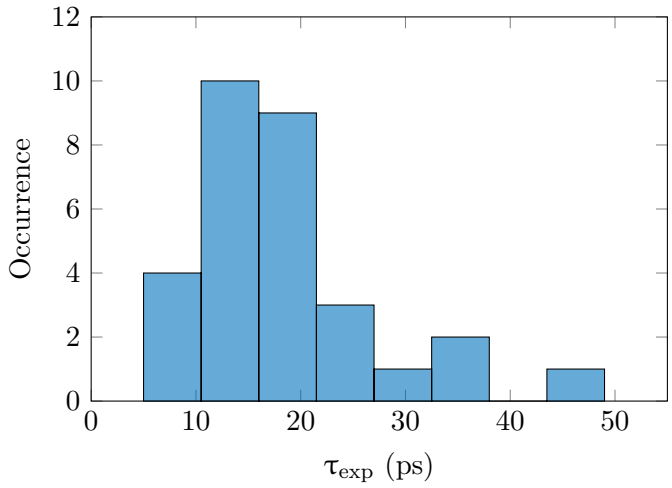

Figure 5.6: Histogram of the extracted exponential decay time component τ_{exp} for a total of 30 SWCNTs.

Even though a mono-exponential model function was sufficient in describing the PL decay of the single SWCNTs it is no longer suitable for the TiSCAT transients shortly after the pump excitation where EEA takes place. Two exemplary TiSCAT transients are shown in Fig. 5.7a/5.7b with the corresponding fit (see Eq. 5.1) taking the initial decay dynamics into account. The presented measurements were carried out for the two single (6,5) SWCNTs already used for the TCSPC transients shown in Fig. 5.5. Fitting of the model function was done with an exponential decay rate fixed to the value extracted from the PL measurements. The extracted values for the diffusional decay time τ_D leading to fast EEA are in the order of 1 ps which will be further elucidated in the following section.

The IRF used for the fitting of the model function was determined by TiSCAT measurements on a single-layer of graphene. There, excited charge carriers are generated by the pump pulse which rapidly thermalize leading to a fast decay of the TiSCAT signal. This extremely fast decay was considered as nearly instantaneous due to coupling to phonon modes[170] so the TiSCAT transient was used for an estimation of the IRF of the system which was determined to exhibit a width of approximately 600 fs (FWHM). The corresponding data can be found in Appendix A.

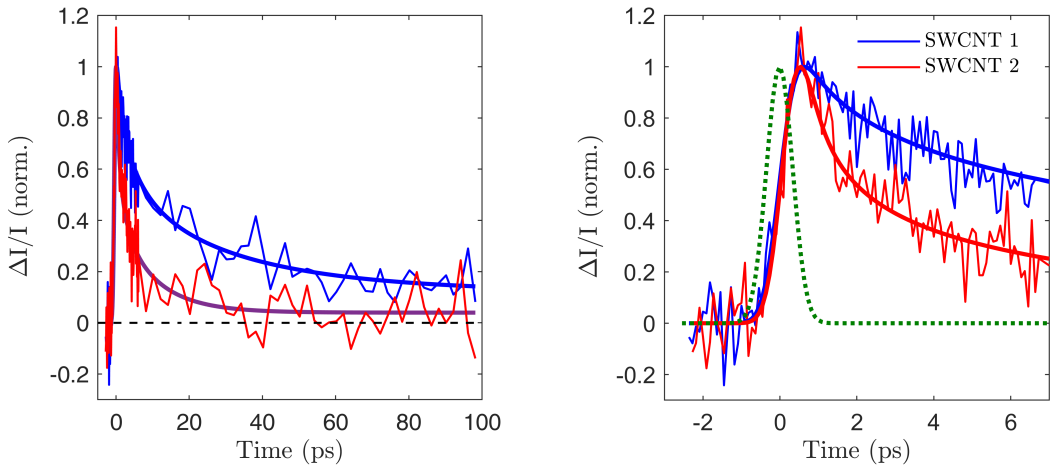

(a) Full range. **(b)** Zoom-in with IRF in green.

Figure 5.7: TiSCAT transients of two (6,5) SWCNTs with the corresponding fit as stated in the text. The considered instrument response function (IRF) is shown in green in b). Modified from [160] under creative commons license CC BY 4.0 (`http://creativecommons.org/licenses/by/4.0/`).

It should be noted that the decay in the range of 10 ps up to 100 ps in the PL and TiSCAT measurements could also be modeled by a $t^{-1/2}$ decay attributed to diffusion driven EEA on a longer time scale as recently suggested [67, 171]. This decay function, however, cannot describe the initial fast time dependence observed in the TiSCAT experiment. Furthermore, on longer time scales the dynamics of the E_{11} excitons has been precisely monitored over several orders of magnitude by TCSPC and can be described by an exponential decay function (Fig. 5.5a)[56, 57, 69, 168].

3 Influence of exciton density on decay dynamics

The implemented experimental setup combined with the model function connecting the many-body effects and the intrinsic exponential decay allows for the investigation of the exciton-exciton annihilation process in further detail. As the effect of EEA is dependent on the density of participating particles it can be investigated in further detail by the variation of the pump power and thus the number of created excitons. This is depicted in Fig. 5.8 for a single (6,5) SWCNT at two different pump powers. An increase of the incident power leads to significantly faster decay dynamics for early times after excitation.

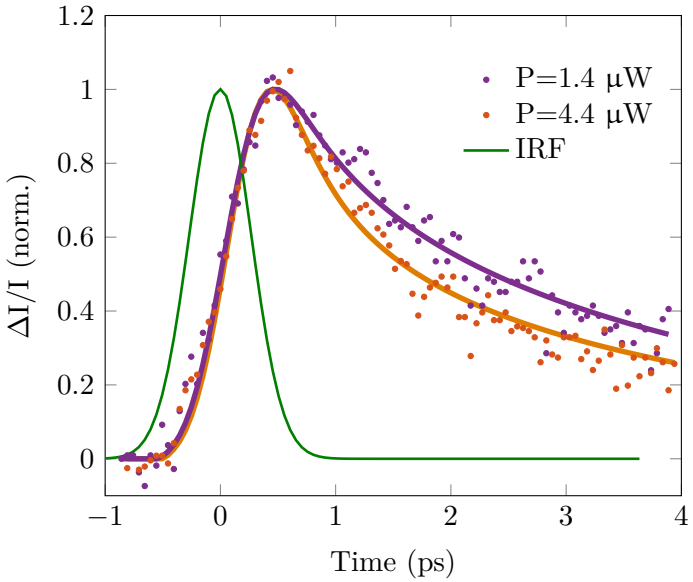

Figure 5.8: TiSCAT transient detected for a single (6,5) SWCNT for pump powers of 4.4 μW and 1.4 μW together with the fitted model curves, respectively. Modified from [160] under creative commons license CC BY 4.0 (`http://creativecommons.org/licenses/by/4.0/`).

Figure 5.9 illustrates the dependence of the derived diffusion time τ_D on the incident excitation power (bottom axis) for a set of four different SWCNTs. For the further evaluation the number of created excitons in dependence of the excitation power is derived and depicted in the figure on the top axis. For this the absorption cross section of the (6,5) SWCNTs is calculated from recent measurement of Oudjedi et al. closely matching the conditions of the present experiment[172]. There the absorption cross section of the second order optical transition was determined to be $3.2 \cdot 10^{-17}$ cm^2 per carbon atom. As an ideal (6,5) SWCNT includes 90 carbon atoms per nanometer[19], this can be calculated to be $\sigma = 8.6 \cdot 10^{-16}\ \frac{cm^2}{nm}$ taking

into account the off-resonant excitation at 880 nm and the approximately 3 times stronger absorption of the first order transition E_{11} compared to E_{22} (see ensemble absorption in Fig. 5.2b). The total absorption cross section then amounts to $\sigma \cdot L_{CNT}$, where L_{CNT} denotes the length of the nanotube. In the experiment the nanotube length significantly exceeded the diffraction limited spot size which is calculated as $d_f = 1.22\frac{\lambda}{\mathrm{NA}} = 720$ nm. With a focus area of $A_f = \pi(d_f/2)^2$ the absorption probability becomes $\alpha = \sigma d_f / A_f = 1.6 \cdot 10^{-4}$. This value applies for the case of a plane wave excitation and will be slightly smaller in the case of the focused beam due to orthogonal polarization components of the fields. In the experiment nanotubes which were oriented parallel to the excitation spot polarization were chosen for measurements as they render the strongest absorption (as already pointed out in section 2.1). Finally, the average number of initially created excitons can be calculated as $n_{exc} = \alpha N_{\mathrm{photons}}$ (see top axis in Fig. 5.9).

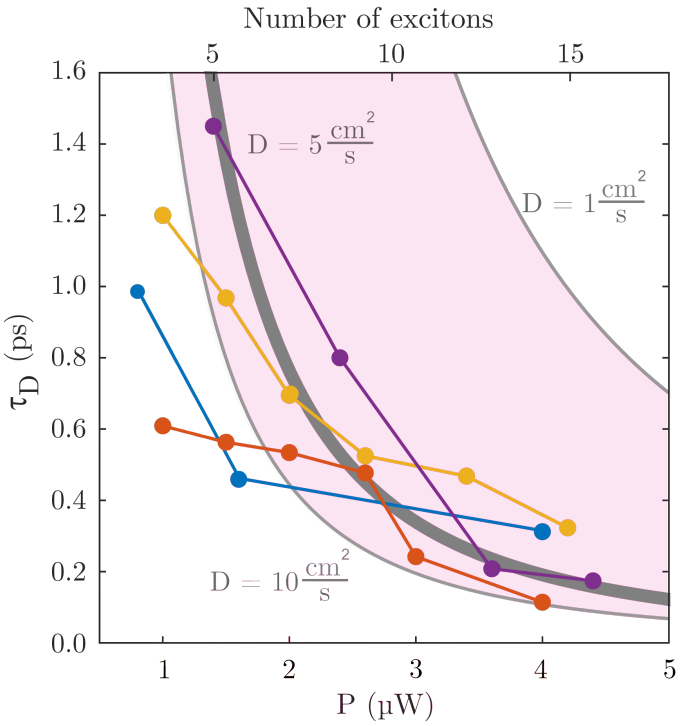

Figure 5.9: Pump power dependence of the diffusion time τ_D for four different nanotubes as derived from fitting the detected transients. The calculated diffusion times for diffusion coefficients of D = 1 $\frac{cm^2}{s}$ and 10 $\frac{cm^2}{s}$ are shown as solid grey lines. The best agreement with the experimental data was found for a diffusion coefficient of D = 5 $\frac{cm^2}{s}$ which is rendered as bold grey line. Modified from [160] under creative commons license CC BY 4.0 (`http://creativecommons.org/licenses/by/4.0/`).

From the amount of initially created excitons the average exciton-exciton distance can be calculated as $d_0 = d_f/(2N_{exc})$[65] considering a Gaussian distribution of excitons following the spatial profile of the focused excitation beam. The exciton diffusion coefficient D of freely suspended thin semiconducting SWCNTs has recently been reported for both bright and dark excitons by Ishii et al. who found a power law function describing the diffusion constant in dependence on the thickness of the SWCNT[69]. Using $d = 0.747$ nm for a (6,5) SWCNT one obtains $D \approx 7\ \frac{cm^2}{s}$ for the bright exciton. This value probably represents an upper limit of the diffusion constant because of the decoupling from any substrate material. Indeed, other reported values for micelle-encapsulated and polymer-wrapped SWCNTs were in the range of $D = 0.4\ \frac{cm^2}{s}$ to $7.5\ \frac{cm^2}{s}$[164, 173].

Using the values for D and d_0 one can calculate the diffusional time as $\tau_D = d_0^2/D$. This was done for $D = 1\ \frac{cm^2}{s}$ and $D = 10\ \frac{cm^2}{s}$ which are reasonable limits for the dynamics in the SWCNTs as stated before. The corresponding curves are inserted into Fig. 5.9 in form of grey lines and match with the fit results extracted from the measured data. The best agreement was found for a diffusional time of $D = 5\ \frac{cm^2}{s}$ which is shown in the figure as well. However, for low excitation powers the predicted times appear to be systematically longer than the experimental ones, whereas a better match is seen for high powers. The observed deviation of the diffusion times is attributed to spatially heterogeneous diffusion coefficients as expected for SWCNT environments that are known to lead to efficient exciton localization and thus changes in the diffusion behaviour of excitons[174].

The dependence of the pump power on the TiSCAT signal amplitude was determined by measurement of the peak value detected for different power values of the pump arm. This was done experimentally by adjusting the AOM driver level. For the power levels used in the present measurements no saturation of the signal was observed which is shown in Fig. 5.10a. A linear fit crossing the origin of coordinates is depicted in orange. This supports the approach for the previous calculation of the exciton distance in dependence of the power. There a linear behaviour of the exciton number with the excitation intensity was assumed.

Additionally, the power dependence of the TiSCAT signal was investigated for variations of the probe power as shown in Fig. 5.10b. This was experimentally realized via a lambda-half-plate which rotates the laser polarization and a subsequent polarizer which blocks out the perpendicular light component. By this way, by rotating the lambda-half-plate the power can be attenuated without further optical density filters which would alter the temporal overlap of both beams or misalign the spatial overlap. An approximately constant signal amplitude can be observed for the vari-

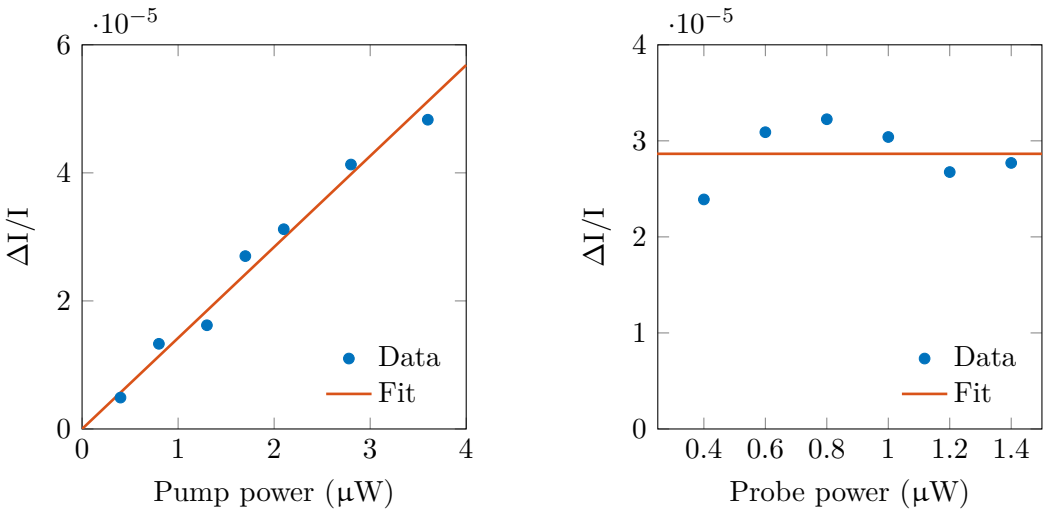

(a) Variation of the pump power.

(b) Variation of the probe power.

Figure 5.10: Measurement of the TiSCAT signal amplitude in dependence of the incident pump and probe power, respectively. A linear dependence of the pump power and a constant value for variation of the probe power was observed. Modified from [160, suppl.mat.] under creative commons license CC BY 4.0 (`http://creativecommons.org/licenses/by/4.0/`).

ation of the probe power which is indicated by the orange horizontal line depicted in the figure. This supports the assumption that no signal saturation occurred for the employed probe fluences.

4 Monte-Carlo simulation of EEA

Whereas the analytical model presented in the previous section fits well for the case of a high excitation fluence and thus a high exciton density, it reaches its limit for the case of a low excitation fluence where the quantization of annihilation partners becomes prominent. In the experimental data (Fig. 5.9) this deviation becomes apparent for small excitation powers below 2 μW corresponding to 5 initially created excitons on average. Additionally, in the analytical model all heterogeneities along the tube which can affect the exciton movement are summarized in a single, homogeneous diffusion coefficient.

For a further investigation of the EEA dynamics in SWCNTs, especially in the case of low exciton numbers and in presence of localization sites leading to a heterogeneous diffusion coefficient, Monte-Carlo simulations were carried out. The corresponding simulation code can be found in Appendix B.

First, the simulation of the initial exciton distribution along the nanotube was modeled with the subsequent diffusive motion.
The initial exciton distribution was done via random allocation of positions following a Gaussian distribution modelling the intensity profile of the focussed excitation beam. The number of created excitons was set as described in the previous section. After the creation of the excitons the mean distance to the nearest neighbour quasi particle was determined. The comparison to the data analytically acquired is depicted in Fig. 5.11a. The simulated data points (green circles) match well with the analytical model for the case of a focused excitation (yellow line). The case of a linear excitation of the tube for the same number of excitons is additionally shown as a blue curve, emphasizing the influence of the focused excitation on the mean distance of the excitons.

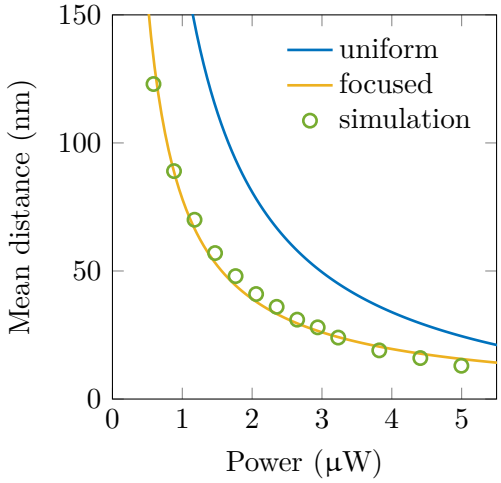

(a) Initial mean distance of the excitons.

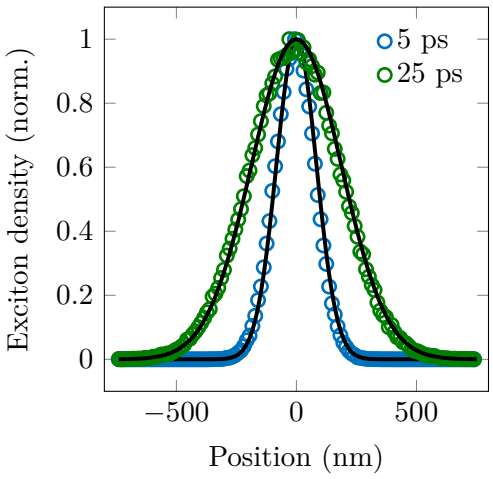

(b) Diffusion of excitons created at $x = 0$.

Figure 5.11: The initial creation of excitons following the focus spot profile as well as the diffusive motion along the tube was compared to the analytical calculations.

To account for the diffusive motion of the particles a Brownian motion is assumed where an exciton can perform a jump to the next lying left or right position with equal probability for each time step in the simulation. From the theory of the Brownian motion it is known that the distribution of particles initially located at position x_0 at the time t can be described as follows[175]:

$$F(x,t) = \left(\frac{1}{4\pi Dt}\right)^{\frac{1}{2}} \exp\left(-\frac{(x-x_0)^2}{4Dt}\right). \tag{5.2}$$

This process of motion exhibits a mean-square displacement (MSD) of

$$MSD = 2Dt. \tag{5.3}$$

The mean distance travelled by a diffusive particle can thus be derived as $d_{mean} = \sqrt{MSD} = \sqrt{2Dt}$. This was used to scale the step probability in the Monte-Carlo simulation in order to fit to the given diffusion constant, time-step width and position-step size. To fit to any chosen time value, the particle can either make a step or stay at its current position. To verify the implementation of the diffusive motion a number of excitons was created in the middle of the simulated nanotube. The particle distribution after 5 ps and 25 ps, respectively, was then compared to the analytically expected distribution (Eq. 5.2) for the same diffusion constant ($D = 7\ \frac{cm^2}{s}$) as depicted in Fig. 5.11b. Excellent agreement was found for simulated data (green and blue circles) and the analytical calculation (black curves).

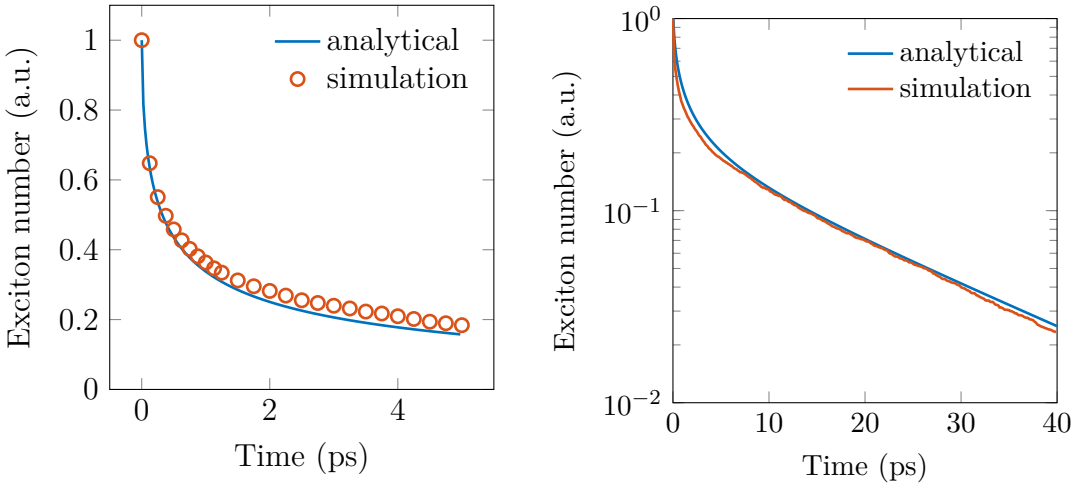

(a) Early decay governed by EEA.

(b) Exponential decay at later times.

Figure 5.12: Comparison of the Monte-Carlo simulations comprising EEA and mono-exponential decay with the analytical solution suggested by Srivastava and Kono[65].

In the next step the EEA and mono-exponential decay was implemented. Taking a mean EEA-interaction distance of the excitons into account, a distance d_{EEA} was defined at which two approaching particles annihilate if the distance of both is smaller than the defined value. For every time step of the simulation this distance to the nearest neighbour is calculated and annihilating excitons are removed. Furthermore, every exciton has a certain probability for an intrinsic decay in every iteration step defined as $p = 1 - \exp(-(\tau_{step}/\tau_D))$ describing an exponential decay with time constant τ_D. Additionally, a moving exciton decays when reaching one of the nanotube

ends. This accounts for quenching at the tubes ends as previously experimentally observed[61].
The results of the simulation were compared to the analytical calculation done with Eq. 5.1 for comparable parameters as shown in Fig. 5.12a and Fig. 5.12b. In the simulation 10 excitons were initially created along the nanotube. A diffusion constant of $D = 7\ \frac{cm^2}{s}$ was assumed which translates to a diffusive time constant $\tau_D = d_0^2/D \approx 0.5$ ps for the case of a focused excitation. The exponential lifetime of the excitons was set to 20 ps in both the Monte-Carlo simulation and the analytical calculation, respectively. The parameter of the exciton-exciton annihilation (d_{EEA}) was set to 5 nm which resulted in good agreement of the simulation and the calculation. The assumption of the EEA-distance is in fair agreement with reported exciton sizes in the range of 1 nm to 13 nm[66, 169, 176]. The effect of fast EEA is clearly visible in Fig. 5.12a whereas the transition to the slower intrinsic exponential decay can be observed in Fig. 5.12b for longer times.
To further investigate the influence of localization sites changes in the spatial energetic exciton level of the nano object were implemented into the simulation. This was done as suggested by Georgi et al. by a non-isotropic step probability of the exciton located in the energy gradient[163]. This leads to a location-dependent branching ratio of the probability ratio $p_{\mathrm{left}}/p_{\mathrm{right}}$ as a motion towards the lowest energetic state is favourable and leads to an additional drift motion. In this simulation the initially unaltered energetic landscape was modified by a single dip of Gaussian shape with the amplitude ΔE_{gap}. Since the exciton diffusion is driven by temperature T the branching ratio can be expressed by[163]

$$\frac{p_{\mathrm{right}}}{p_{\mathrm{left}}} = e^{-\frac{\Delta E}{k_B T}}. \tag{5.4}$$

With p being the probability in the unaltered case to make a step to the left/right it can be followed:

$$p_{\mathrm{left}} + p_{\mathrm{right}} = 2p. \tag{5.5}$$

Thus, the step probabilities become

$$p_{\mathrm{left}} = \frac{2p}{1 + e^{-\frac{\Delta E}{k_B T}}} \qquad \text{and} \qquad p_{\mathrm{right}} = \frac{2p}{1 + e^{+\frac{\Delta E}{k_B T}}}. \tag{5.6}$$

Here ΔE describes the energy difference between the current exciton position and the nearest neighbour position to the left and right.
The effect of such a localization site is depicted in Fig. 5.13 where a dip of the energy landscape was assumed to be located in the middle of the focus spot. An energy

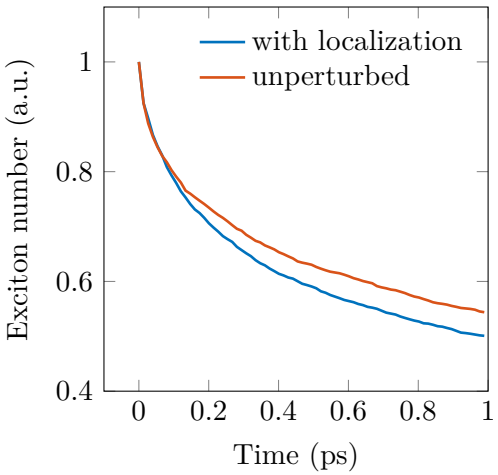

Figure 5.13: Monte-Carlo simulation of EEA under the influence of a localization site introducing a spatial modification of the excitonic energy. This leads to a speed up of the decay process as a drift motion towards the energy minimum is induced.

minimum of 100 meV with a width of the Gaussian shape of 20 nm was assumed. The figure shows the mean value of 1500 iterations with 3 initially created excitons. In this simulation the intrinsic decay of the excitons was switched off so the effect of EEA is the only decay channel besides end quenching. Apparently, the localization site significantly speeds up the effect of exciton-exciton annihilation.

To compare the results of the Monte-Carlo simulation with the analytical model the calculation was done for a different number of initially created excitons corresponding to variations in excitation power. Subsequently, the model function (see Eq. 5.1) was fit to the resulting transients. The extracted diffusional times τ_D are depicted in Fig. 5.14 together with the analytical curves in grey as already shown in Fig. 5.9. Noticeably, this speed up of the EEA decay due to localization sites is of higher impact for lower numbers of excitons whereas the effect vanishes for higher exciton densities where the quantized values agree well with the analytical curves. This can be understood by the fact that for small exciton numbers the relative contribution of single excitons remaining without annihilation partner becomes more relevant as has also been noted by Srivastava and Kono[65].

Introducing a single localization site in the center of the illuminated section of the SWCNT significantly speeds up the EEA dynamics for excitation powers below 3 µW, equivalent to about 10 initially created excitons. This is unexpected for a diffusion-limited system as inhibiting one of the reaction partners is assumed to slow down the diffusion time corresponding to a reduced diffusion coefficient decreased from $2 \cdot D$ to D. However, for a spatially confined excitation region as in the case

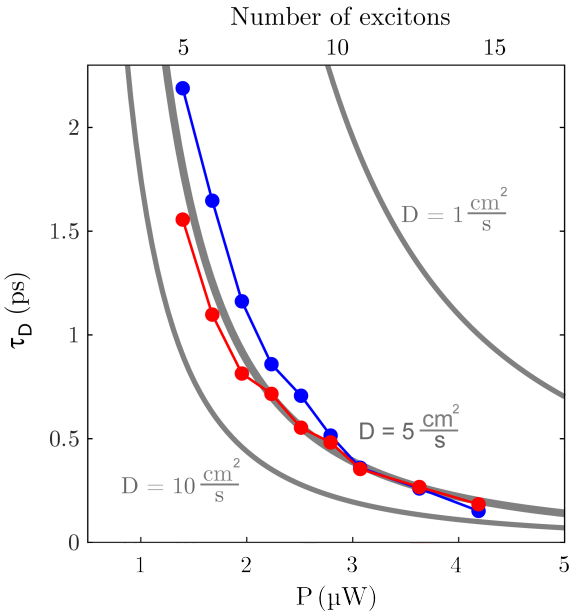

Figure 5.14: Monte-Carlo simulations of the diffusion times with (red points) and without (blue points) exciton localization and a diffusion coefficient of $D = 5\ \frac{cm^2}{s}$. Analytically calculated diffusion times for $D = 1, 5$, and $10\ \frac{cm^2}{s}$ are shown as solid gray lines. Modified from [160] under creative commons license CC BY 4.0 (`http://creativecommons.org/licenses/by/4.0/`).

of a tight focusing of the laser beam on the SWCNT, the distribution of excitons is strongly heterogeneous. The localization site thus prevents the confined excitons to escape from the high density exciton region preserving a higher probability for EEA events. In contrast, freely moving particles could escape unhindered to regions of lower exciton density leading to a smaller probability for an EEA encounter and thus a higher diffusional time τ_D. This effect is less pronounced in the case of higher initial excitons densities as the EEA becomes extremely fast. Here, the diffusional times decrease slower in the presence of a localization site matching the behaviour observed for the experimental data seen in Fig. 5.9. Adding further localization sites to the illuminated section of the SWCNT has a smaller effect on the EEA dynamics. The overall impact on the exciton decay will be an ensemble effect consisting of the number and distribution of the localization sites along the SWCNT. The observed variations in the experimental data from nanotube to nanotube is attributed to such heterogeneities. In a future work, this could be experimentally investigated by the implementation of an additional near-field probe enhancing the spatial resolution of the system down to the order of tens of nanometers.

5 Conclusion

In summary, time resolved photoluminescence and transient interferometric scattering (TiSCAT) microscopy has been utilized to investigate the dynamics of single semiconducting (6,5) SWCNTs deposited on a glass substrate. Both measurements were able to visualize the single nano objects. Time resolved PL measurements revealed differences in the transients which exhibited decay times in the range between 5 ps and 48 ps which could be due to different lengths of the SWCNTs, variations of the environment or defects along the nanotubes.
By time resolved TiSCAT measurements on the same single carbon nanotubes exhibiting similar temporal decay behaviour a model was applied unifying the observed dynamics of both measurements. Whereas the time resolved PL measurement cannot resolve the initial decay dynamics due to its limited temporal resolution, TiSCAT measurements are capable to bridge this gap. By making use of the model suggested by Srivastava and Kono[65] both measurements have been combined taking into account the mono-exponential decay of the single excitons and the initial exciton-exciton annihilation (EEA).
By variations of the pump power in TiSCAT measurements the effect of EEA dependent on the number of created excitons was investigated. Here, a speed-up of the decay was observed for an increasing particle density. The corresponding diffusive time constant describing the EEA decay which was extracted from the model function showed a decrease from approximately 1 ps down to 200 fs. This is in accordance to the analytical assumptions made from geometrical calculations of the focused excitation.
Furthermore, Monte-Carlo simulations were carried out improving the understanding of the EEA decay dynamics. Good agreement with the analytical model was achieved by implementation of the exponential decay of the exciton and the EEA process. Nanotube to nanotube variations could be explained by localization sites modifying the energy landscape of the SWCNT which can speed up the initial decay. Further improvement of the spatial resolution of the TiSCAT setup by implementation of a near-field probe could lead to a better understanding of the underlying defect mechanisms happening on the order of tens of nanometers.

Chapter 6

Measurements on single-layer $MoSe_2$

The following chapter is based on the paper *"Wavelength-Tunable Ultrafast Two Arm Fiber Laser System for Transient Interferometric Scattering Microscopy on Nanoscopic Objects"* that has been published in the *Journal of the Optical Society of America B* 41.2 (2024)[151].

The sample material consisting of exfoliated flakes of $MoSe_2$ transferred onto a glass slide covered by layer of hexagonal boron nitride (hBN) was provided by Dr. Achint Jain from the group of Prof. Dr. Lukas Novotny from the ETH Zürich. See section 3.3 for more details about the sample preparation.

In this chapter TiSCAT measurements on single-layers of molybdenum diselenide ($MoSe_2$) will be shown. Its uniquely high absorption especially in the form of a monolayer[83] and other optical properties have drawn recent attention to this type of semiconductor which is assigned to the material class of transition metal dichalcogenides (TMDCs)[70]. Similar to single-walled carbon nanotubes its optical properties are mainly governed by excitonic states due to the strong confinement of charge carriers and weak shielding of electric fields.
TiSCAT spectroscopy will be utilized in order to identify the spectral position of the mentioned excitonic energy levels. Further evaluation of the signal contribution gives insight into the origin of the involved decay dynamics.
The effect of intensity noise of the laser source on the pump-probe signal will be evaluated on this material as it compromises high photostability and an uniform spatial TiSCAT signal. This will be utilized for comparison measurements of the titanium-sapphire laser setup and the novel fiber laser setup. Noise measurements of

the individual setups will be used to assess the influence of experimental parameters and to calculate the sensitivity of both the systems.

1 TiSCAT microscopy

The optical and electronical properties of transition metal dichalcogenides are predominantly governed by the number of stacked layers of the material. $MoSe_2$ transforms from an indirect semiconductor to a direct semiconductor as it is reduced from multilayer thickness to a monolayer sheet[177]. In Fig. 6.1 this can be seen by comparing the confocal PL image (a) and the TiSCAT image at zero time delay (b) of the same sample region. In the confocal photoluminescence image only the monolayer can be observed as the multilayer does not show radiative recombination, thus remaining dark. Both images were taken utilizing the fiber laser system with a pump wavelength of 780 nm. For the TiSCAT measurement a probe wavelength of 810 nm was chosen which corresponds to the lower-energy side of the lowest excitonic state transition (E_{11}) as shown in the next section. The used power levels at the position of the sample are 5 µW for the pump arm and 1 µW for the probe arm. Detection of the probe light was done after removing the pump light via two long pass filters with cut off wavelengths at 810 nm and 800 nm, respectively. This non-ideal filter combination was necessary for a sufficient removal of residual pump light even if the probe light was attenuated partially as well. Further measurements at longer probe wavelengths did not suffer from this restriction.

A noticeable difference of both contrast mechanisms seen in Fig. 6.1 is the limitation of PL measurements to materials exhibiting a direct bandgap, and thus, a radiative recombination of states. This restriction is not applicable for transient interferometric scattering as it is not limited to the probing of emissive states. This can be seen in the microscopy image in Fig. 6.1b obtained by the TiSCAT technique where the multilayer part of the $MoSe_2$ sample can be observed in the left part of the image whereas the same region in the PL-image remains dark.

Both images basically show the same features of the single-layer flake including cracks, wrinkles or other defects. The TiSCAT signal is mainly negative for most parts of the object which translates to a photoinduced absorption of the material. The origin of this effect will be discussed in the next section. Additionally, small spots exhibiting a positive signal contribution can be observed. This areas of pump induced decrease of ground state absorption could potentially be attributed to local defect sites or doping causing a spectral red-shift of the exciton resonance leading to a ground state bleaching contribution at 810 nm.

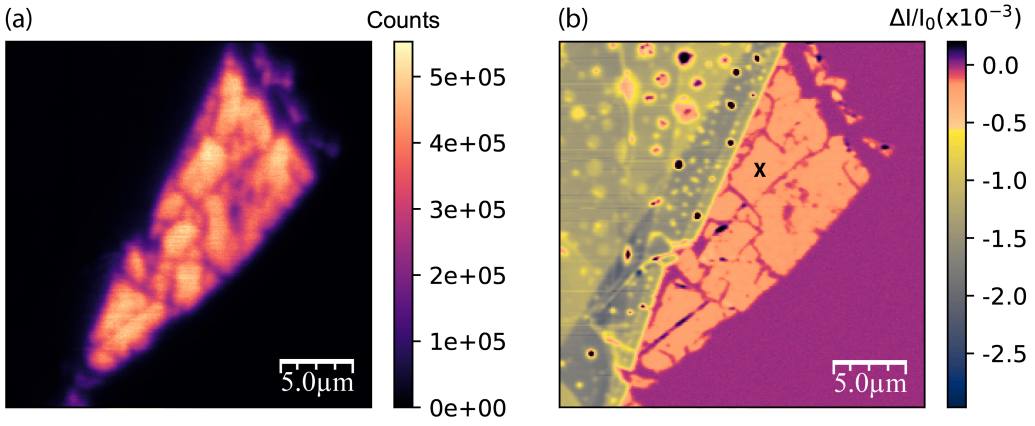

Figure 6.1: a) Confocal photoluminenscence image of a single-layer of $MoSe_2$ excited at 780 nm. b) TiSCAT image of the same area probed at 810 nm and zero time delay between pump- and probe-pulse. The monolayer in the center and the multilayers in the left part of the image exhibit a negative TiSCAT signal corresponding to pump-induced absorption. The position of the measurements shown in Fig.6.3 were taken at the position marked with a 'X'. Adapted with permission from [151] © Optical Society of America.

Figure 6.1 elucidates the improvement of the spatial resolution of the TiSCAT measurement in contrast to the PL image. The pump-probe technique exhibits the nonlinear characteristics of a multiphoton measurement and thus the effective point spread function (PSF) is created by the multiplication of the pump PSF and the probe PSF which results in an effective PSF whose FWHM can be calculated as[178, suppl.mat.]

$$\mathrm{FWHM_{PSF}} = \frac{0.53}{\mathrm{NA}} \sqrt{1/\left(\frac{1}{\lambda_p^2} + \frac{1}{\lambda_{pr}^2}\right)}. \tag{6.1}$$

Here λ_p and λ_{pr} denote the pump and probe wavelength, respectively. In this calculation the PSF of pump and probe beam where approximated by a Gaussian function. For the present measurement with excitation at 780 nm and probing at 810 nm, this yields a theoretical width of the effective PSF of 200 nm which is roughly a factor $\sqrt{2}$ smaller than for linear microscopy like one-photon excitation photoluminescence. A quantitative measurement of the spatial resolution of the measurement setup is given in chapter 7.

2 Spectrally resolved TiSCAT

For a better understanding of the involved decay mechanisms a spectrally resolved TiSCAT measurement was carried out on a single-layer of $MoSe_2$. For this purpose the pump-probe scheme was transferred to the spectrometer measuring at 500 Hz frame rate. The pump modulation was adjusted to 250 Hz hence the recorded data alternately include pump modulated and unmodulated probe spectra. The simultaneously triggered program written in *LabVIEW* sorts and classifies the measured data and calculates the change in reflectivity $\Delta I/I$ measured over a series of measurements. These were done utilizing the Coherent Mira900 setup where the probe light was not cut by the use of bandpass filters, thus yielding pump-probe data for a broad wavelength interval ranging from approximately 750 nm to 1000 nm. The pump wavelength was set to 730 nm which is off-resonant of the E_{11} transition in $MoSe_2$, and thus, allows the probing of the transition in this experimental configuration.

Optical elements like the microscope objective introduce noticeable amounts of chromatic dispersion leading to differences in group velocities of the spectral parts of a broadband pulse. This can be observed in spectrally resolved pump-probe measurements leading to variations in the temporal position of the pulse overlap for different probe wavelengths. This would limit the meaningfulness of spectrally resolved TiSCAT measurements involving several signal contributions. This issue is solved by a chirp compensation measured on a graphene layer which has an almost instantaneous pump-probe signal covering the whole spectral range of the used supercontinuum. The wavelength-dependent temporal maxima of the pump-probe data on graphene are used for post-processing subsequent measurements on other materials in order to compensate the chirp of the supercontinuum (see Appendix A). The utilized *Matlab*-Script was written by Edoardo Amarotti and Lucas Lange.

In figure 6.2 a TiSCAT spectrum measured on a single-layer of $MoSe_2$ is shown which is already chirp corrected as explained before. In general two peaks are observable which are centered at a wavelength of 785 nm and 800 nm exhibiting different signal contributions. The peak at 785 nm shows a positive signal translating to a photoinduced bleaching (PB) which is assumed to originate from ground state bleaching of the A-excitonic transition due to phase-space filling (or Pauli-blocking)[90, 89]. The observed peak position and signal contribution is in agreement with previous measurements on single-layer $MoSe_2$[82, 179, 180]. The dip on the longer wavelength side located at 800 nm translates to a pump induced increase of absorption (*photoinduced absorption*, PA). This is attributed to a shift of the excitonic binding energy

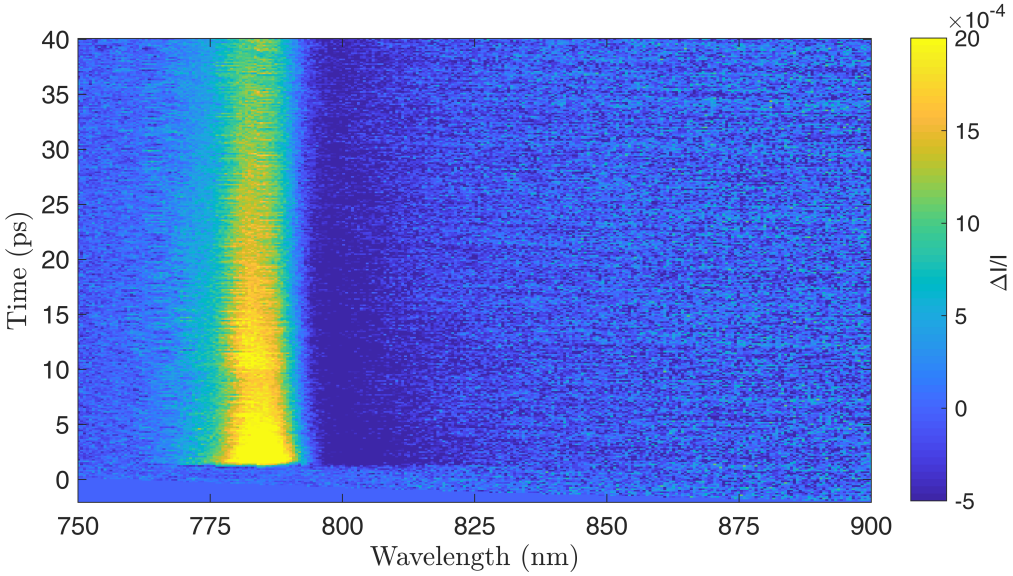

Figure 6.2: Chirp-corrected TiSCAT spectroscopy measurement on a single-layer of $MoSe_2$. Photoinduced bleaching (PB) is observed at 785 nm whereas photoinduced absorption (PA) occurs at 800 nm. The *Matlab*-script used for chirp-correction and data processing was written by Edoardo Amarotti and Lucas Lange.

due to the presence of excited carriers which lead to variations in the shielding of the fields, and thus, the binding energy of excitons. A pump induced shift of the band gap causes an increase of absorption at the probe wavelength and a decrease of absorption at the spectral position the unmodified band gap edge. This shift of the absorption is also called *band gap renormalization* (BGR) and was already observed for TMDCs like tungsten disulphide WS_2[90, 181, 182]. Additionaly, Coulomb scattering of the initially created charge carriers results in a spectral broadening of the excitonic peak. This effect is also known as *excitation-induced dephasing*[89].

Time-resolved TiSCAT measurements using the fiber laser system were carried out in order to further investigate the PA signal observed for wavelengths exceeding 800 nm. Starting at 810 nm transients were recorded up to 100 ps pulse delay. The measurements are summarized in Fig. 6.3a). At pulse overlap a photoinduced absorption signal is identified for all probe wavelengths up to 940 nm with an instantaneous signal rise within the IRF response. The signal is vanishing in the spectrally resolved TiSCAT measurement for wavelengths exceeding approximately 830 nm due to the limited signal to noise ratio of that experimental setup (see Fig. 6.2). In figure 6.3b) the same data is depicted normalized to the same amplitude indicating similar decay dynamics except the transient taken at a probe wavelength of 810 nm.

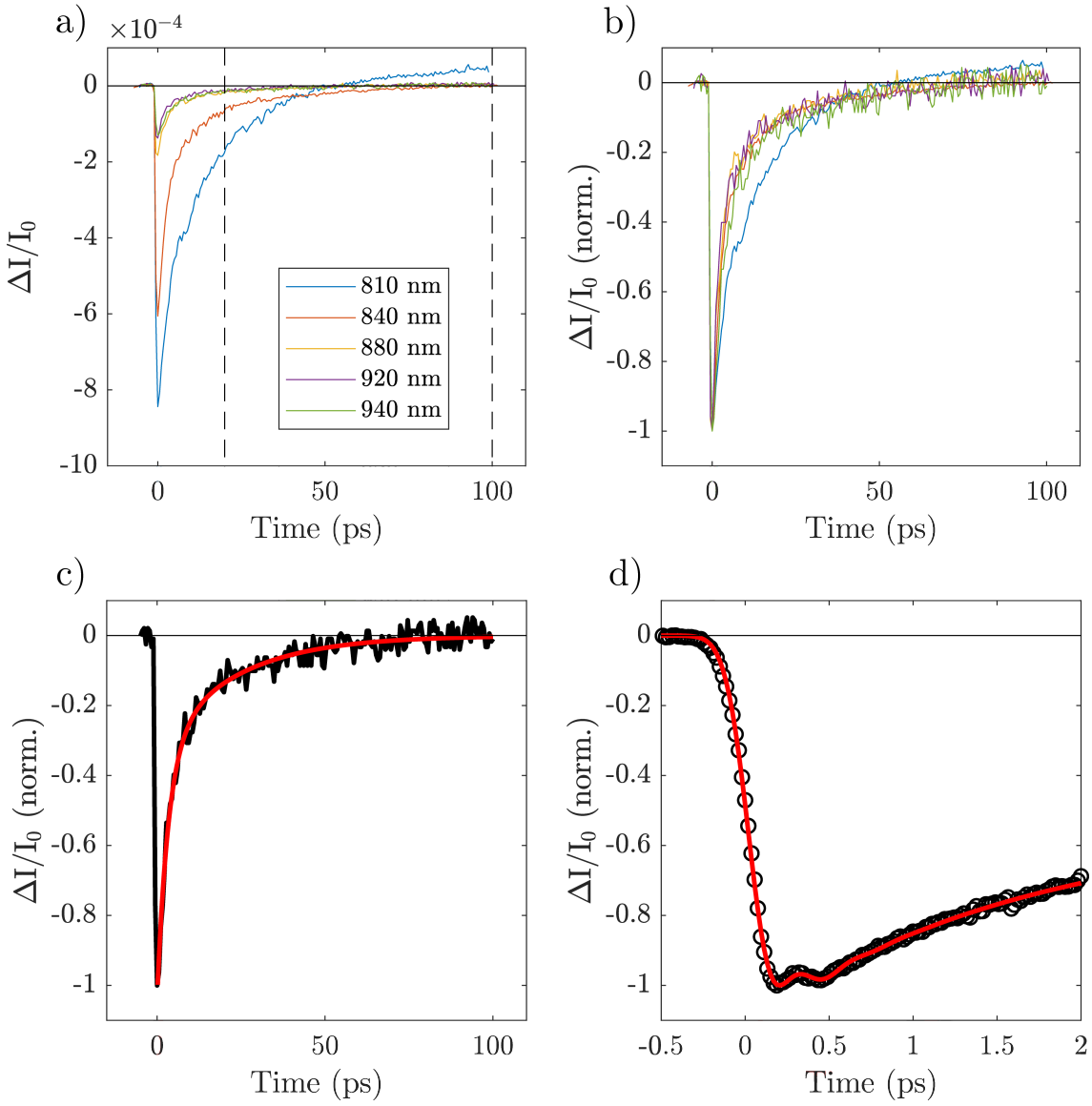

Figure 6.3: (a) Time-resolved TiSCAT measurements on single-layer $MoSe_2$ for different probe wavelengths between 810 nm and 940 nm. The dotted lines at 20 ps and 100 ps time delay denote the signal contribution at which the TiSCAT images in Fig. 6.4 were taken. (b) Same transients as in (a) normalized to the same amplitude for comparison. c) Transient detected at 940 nm together with fitted model function. d) Transient detected at 810 nm together with fitted model function including a damped oscillatory component for the initial dynamics. Adapted with permission from [151] © Optical Society of America.

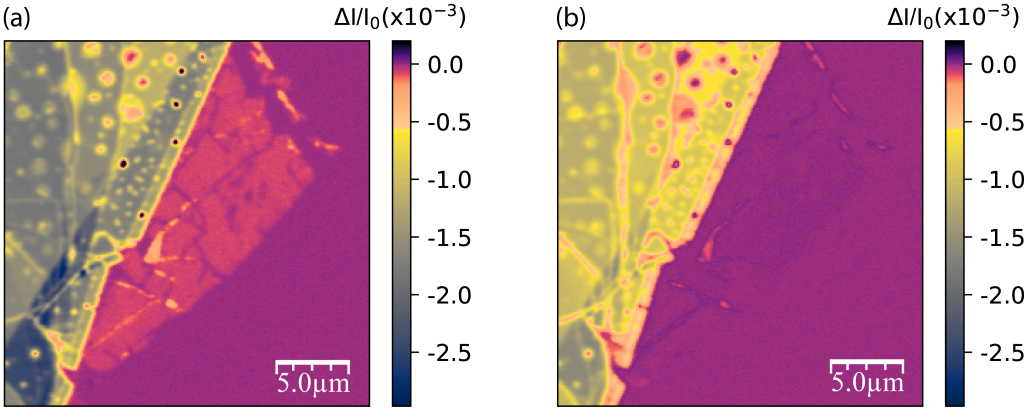

Figure 6.4: TiSCAT image probed at 810 nm at a time delay of a) 20 ps and b) 100 ps. A sign reversal can be observed from photoinduced bleaching to photoinduced absorption. Adapted with permission from [151] © Optical Society of America.

Indeed, all these decay curves can be fitted by the same model function describing a bi-exponential decay function with decay times of 3 ps and 22 ps, respectively. This is exemplary shown for the measurement taken at a probe wavelength of 940 nm in Fig. 6.3c) where the fitted model function is shown as red curve. These two decay times can be assigned to electronic and phononic relaxation after pulsed excitation, respectively[89]. An additional component of the decay dynamics in $MoSe_2$ is observable within the first 2 ps after excitation as exemplary shown in Fig.6.3c. Here a strongly damped oscillatory component is visible. This can be modelled by adding a strongly damped sinusoidal component with a period of about 300 fs to the bi-exponential fit already mentioned. This initial behaviour can be assigned to the excitation of a strongly damped coherent phonon mode[183, 88].

In contrast, the transient at a probe wavelength of 810 nm cannot be described by this model function as a transition from PA to PB occurs at a pulse delay of around 50 ps. An explanation for this behaviour could be an overlap of PA and PB signal contributions. As mentioned before, the excitation wavelength of the A-exciton is located at approximately 785 nm and was reported to show photobleaching in transient absorption experiments due to Pauli-blocking[90]. The small PB signal observed at 810 nm probing for longer delay times can thus be attributed to a small residual fraction of longer-lived excited states preventing complete ground state recovery. These states could be trions formed by environmental doping for example by polymer residues from flake transfer[184].

This is shown in Fig. 6.4 where the temporal delay between the pump and the probe arm was held constant at 20 ps (image a)) and 100 ps (image b)), respectively

where the change in sign of the TiSCAT signal can be observed. Additionally, small regions inside the flake can be identified which show higher signal amplitude. This is attributed to small residual pieces of multilayer $MoSe_2$ which exhibit longer exciton lifetimes than single-layer sheets. Indeed, this can also be seen in the PL image (Fig. 6.1a)) of the flake as it shows decreased emission intensity at these spots.

3 Signal assessment for different laser sources

Single-layers of $MoSe_2$ exhibit a high photostability and a spatially uniform TiSCAT response over large areas of the flake, as seen in the previous measurements (e.g. Fig. 6.1b). This makes this material ideally suited for investigations of the sensitivity of the whole experimental setup as well as comparison measurements of different laser sources and their noise characteristics. As stated earlier in section 3.1.2 the pump-probe scheme investigates changes of the reflected and scattered light $\Delta I/I$ at the modulation frequency f_{mod} detected by a fast photodiode. However, as the laser source introduces intensity noise (*relative intensity noise*, RIN, see section 4.3) temporal fluctuations of the emitted pulse train at f_{mod} lead to an increase of noise on the measured TiSCAT signal limiting the detection sensitivity of the experiment.

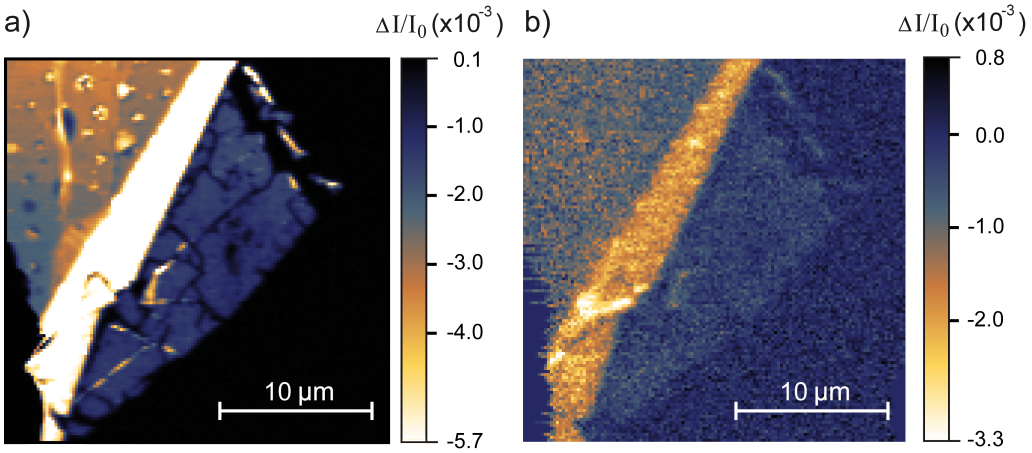

Figure 6.5: TiSCAT image of a single-layer of $MoSe_2$ at zero time delay for both utilized laser systems: (a) Fiber laser b) Ti:Sa setup). The material is excited at 780 nm and probed at 880 nm in both cases. The same experimental parameters for excitation and detection were chosen for both measurements.

Figure 6.5 shows two equivalent TiSCAT measurements of the single-layer $MoSe_2$ for both utilized laser sources comprising on the one hand the fiber laser which was introduced in chapter 4 and secondly the Ti:Sa laser based setup with the supercontinuum fiber as shown in section 3.2. For both measurements the same

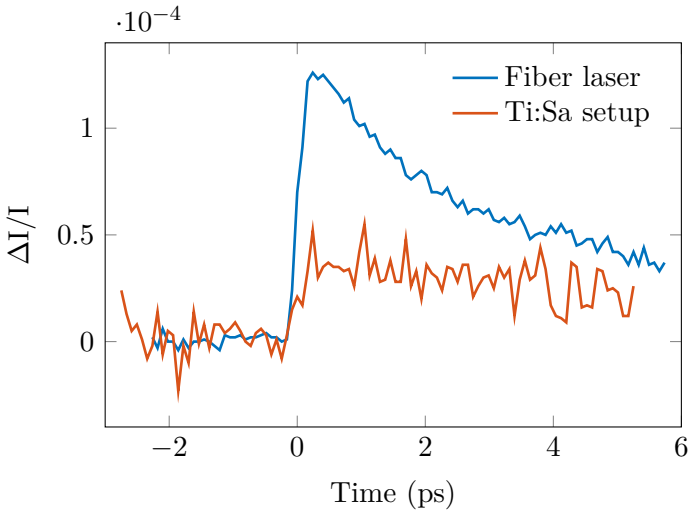

Figure 6.6: TiSCAT transients of both utilized laser sources measured on a single-layer of $MoSe_2$ at a probe wavelength of 880 nm and excited at 780 nm. The same power levels were used for both measurements.

conditions were established including the detection settings like lock-in parameters as well as the power levels focused onto the sample material. The excitation wavelength was set to 780 nm with an average power of 30 µW for both lasers. Probing was done at 880 nm with an average power of 8 µW. This wavelength which is addressing a non-resonant energy was chosen in order to investigate the detection limits of the TiSCAT contrast. In addition, semiconducting (6,4) SWCNTs exhibit their E_{11} transition at this wavelength which will be investigated in the next chapter.
The comparison of both images shows a significantly higher noise level of the Ti:Sa setup than the fiber laser setup. This is strongly emphasized by the signal detected on the glass substrate where no $MoSe_2$ is present and the signal amplitude is vanishing (right side in the images). In the case of the fiber laser this area appears evenly black whereas noise influences of the Ti:Sa setup lead to a coarse-grained appearance of the glass substrate. Small inhomogeneities as cracks or holes are invisible as the noise is dominating the signal variations of the sample.
The TiSCAT amplitude is different for both laser setups as seen in Fig. 6.6 for a corresponding transient measured on the same sample spot of single-layer $MoSe_2$. In principle, the signal amplitude should be comparable if the sample is excited with the same average power and similar pulse characteristics. This can have several reasons:

- **Pulse characteristics:** Even though the transform-limited pulse length of the pump-pulses of both the laser systems is initially of comparable value in the order of 90 fs to 150 fs, the pulse length after the propagation through

the dispersive media of AOM and objective changes this pulse characteristic strongly. The Ti:Sa setup does not contain an optical component compensating this issue utilizing a counteracting dispersive element. The fiber laser system, however, comprises an optical element introducing a pre-chirp of the pump pulses which leads to short pulses at the position of the sample and after propagation through the AOM and the microscope objective. This can be seen in the measurement of the IRF which was found to have a width of 285 fs (FWHM) for the fiber laser, whereas the IRF of the Ti:Sa setup was measured to have a width of approximately 800 fs (FWHM). This leads to peak intensity differences of both laser sources as there is a linear dependence of the peak power of an ideal Gaussian pulse of the temporal width. As shown in section 5.3 many-body effects as exciton-exciton annihilation lead to fast decay processes happening on sub-ps time scales. Thus, variations of the IRF width in this limit give rise to variations in the initial decay of the particles as their creation is not limited to a single, quasi instantaneous event.

- **Setup alignment:** The amplitude of the TiSCAT signal is strongly dependent on the spatial overlap of the pump and the probe arm. Small variations in the adjustment of both laser beams can not be completely excluded. Readjustment of the spatial overlap was repeatedly carried out before the measurement, so the difference in signal amplitude was not attributed to this reason only. Furthermore, the geometrical cross section of the laser beam is an important property of the laser source which limits the minimal possible spot size and so the peak amplitude of the intensity in focus. In principle, the pinhole implemented in the beam expansion should clean up the laser beam from unintended light components and yield a nearly perfect transverse mode of the lowest order (TEM_{00}). However, subsequently following optical components can impair this mode by cutting of the beam shape or introducing other optical aberrations.

Beside the variations of the signal amplitude there is a significant difference of both laser sources concerning the noise floor of the transients as can be observed in Fig. 6.6. The measurement utilizing the fiber laser has a lower average noise level leading to a higher sensitivity resolving small TiSCAT signals.
To determine the origin of the experimental noise properties the RIN of both laser sources was quantified. This was done by measuring the laser intensity at different positions of the optical setup with a fast photodiode. The average power on the detector was held constant for comparable results and to prevent it from saturation

effects. The signal from the photodiode was then passed on to a frequency analyzer for a frequency resolved measurement of the signal contributions.

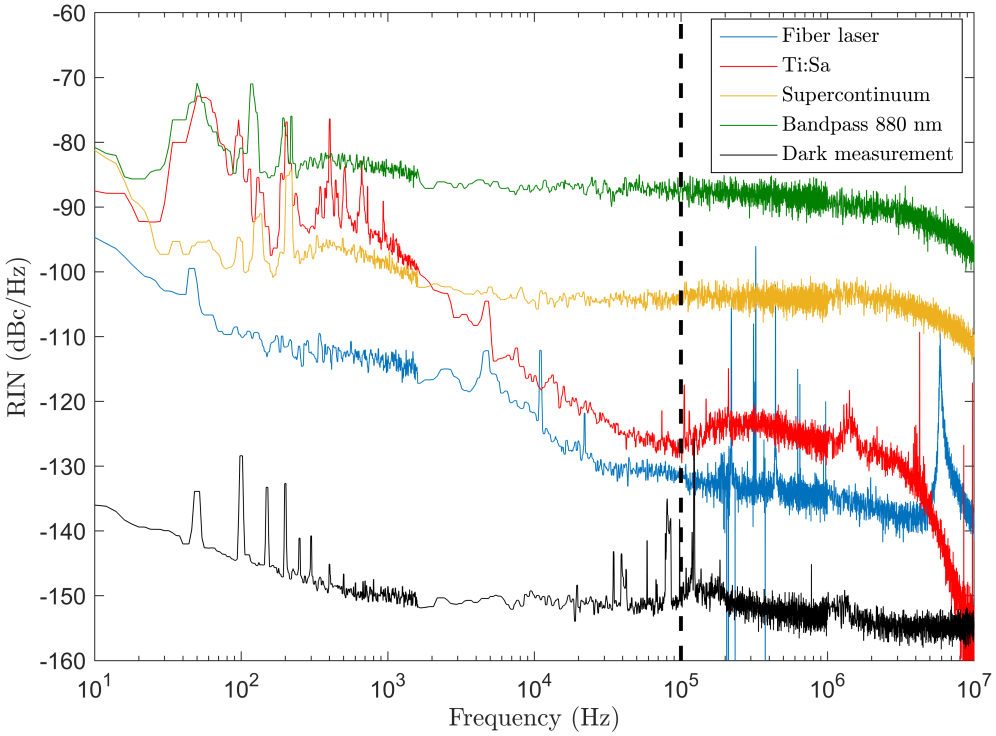

Figure 6.7: Measurement of the relative intensity noise (RIN) of the probe wavelengths of both laser sources. The Ti:Sa setup was measured before the supercontinuum generating fiber at 780 nm ('Ti:Sa'), after the fiber ('supercontinuum') and a bandpass filter ('Bandpass 880 nm'). The modulation frequency f_{mod} is depicted as dashed vertical line. Adapted with permission from [151, suppl.mat.] © Optical Society of America.

The measured data is depicted in figure 6.7. All recorded data were normalized to the average power of the carrier signal and to the measurement bandwidth of 1 Hz (see chapter 4.3) yielding the unit $\left[\frac{\mathrm{dBc}}{\mathrm{Hz}}\right]$. The noise floor of the RIN measurement is depicted in black. The data was smoothed via a moving average filter in order to emphasize differences of the laser sources. The modulation frequency f_{mod} used in the TiSCAT experiment is shown as dashed vertical line accentuating the most important signal contribution for this experiment. The RIN data of the Ti:Sa laser at 780 nm is drawn in red. The noise of the laser increases approximately by 20 $\frac{\mathrm{dBc}}{\mathrm{Hz}}$ at f_{mod} after propagation of the laser through the nonlinear fiber creating the supercontinuum necessary for the probe arm. This can be caused by the nonlinear effects broadening the spectrum of the laser which are highly sensitive to

variations of the pulse intensity.

After the supercontinuum generating fiber, sections of the spectrum are cut out by a bandpass filter in order to probe small spectral features of the sample. Thus, jitter of the spectral composition of the laser spectrum transfers to intensity noise of the light after the filter. This can be seen in Fig. 6.7 for a bandpass filters used in the experiment. The level of the relative intensity noise additionally increases by approximately 15 $\frac{\mathrm{dBc}}{\mathrm{Hz}}$ at f_{mod}. Taking these factors into account, the probe arm of the fiber laser (depicted in blue) has a RIN level at the modulation frequency which is roughly 45 $\frac{\mathrm{dBc}}{\mathrm{Hz}}$ below the noise level of the supercontinuum generating fiber. This is the main reason for the improved sensitivity of the fiber laser setup utilizing the SSFS as observed in Fig. 6.6.

The TiSCAT transients depicted in Fig. 6.6 were used to evaluate the noise characteristics and the sensitivity of the TiSCAT experiment. To exclude effects arising from adjustment issues, the signal before the temporal overlap was used for the calculations which is governed by the noise of the excitation source and the detection electronics.

The signal-to-noise ratio (SNR) of the experiment is calculated as the useful signal amplitude A divided by the standard deviation of the signal σ[185]. For this measurement the signal amplitude was assumed as the peak amplitude of the TiSCAT transient. The sensitivity of the measurement is given by the signal amplitude which is necessary to outweigh the noise of the experiment hence the standard deviation of the noise floor. From the measurements on single-layer $MoSe_2$ at a probe power of 8 µW (see Fig. 6.6) this was calculated for the fiber laser to be $\sigma = 2.4 \cdot 10^{-6}$ which is a lower limit for the detectable signal in this configuration.

The physical limitation of the sensitivity in this experiment is given by the optical shot noise which arises from the quantization of the photons detected by the photodiode. The corresponding rms value of the shot noise σ_{shot} can be calculated as[186, suppl.mat.]

$$\sigma_{\mathrm{shot}} = \sqrt{2h\nu BP} = \sqrt{2h\frac{c}{\lambda}BP}. \tag{6.2}$$

Here h denotes the Planck constant, ν the frequency of the probe light, B the measurement bandwidth and P the optical power received by the detector. The measurement bandwidth is determined by the integration time of the single measurement step t_{int} as $B = 1/t_{\mathrm{int}}$. Typical values of the experiment (as used for the transients in Fig. 6.6) are $\nu = \frac{c}{\lambda} = \frac{c}{880\,\mathrm{nm}}$, $B = \frac{1}{3\,s}$ and $P = 70$ nW. This yields $\sigma_{\mathrm{shot}} = 0.10$ pW.

The detection limit due to shot noise $\left(\frac{\Delta I}{I}\right)_{min,shot}$ is then given by [186, suppl.mat.]:

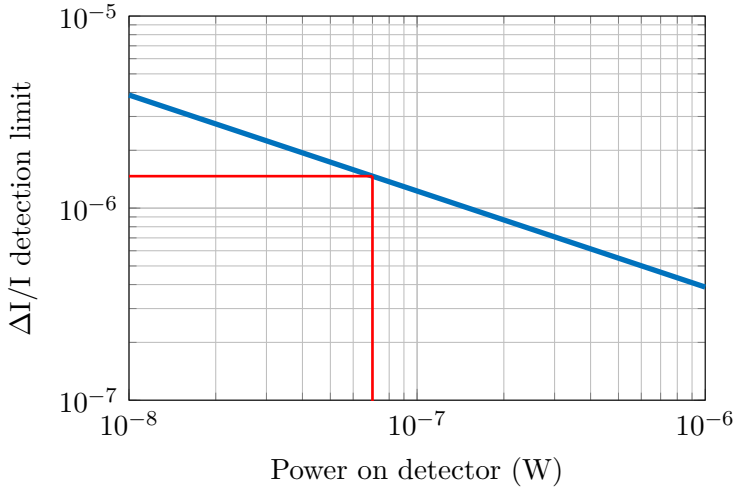

Figure 6.8: Theoretical calculation of the shot noise limitation of the detection sensitivity in the TiSCAT experiment for typical parameters as stated in the text. The red line shows the detection settings as used in the experiment.

$$\left(\frac{\Delta I}{I}\right)_{\text{min,shot}} = \frac{\sigma_{\text{shot}}}{P} = \frac{0.10\,\text{pW}}{70\,\text{nW}} = 1.4 \cdot 10^{-6}. \tag{6.3}$$

From Eq. 6.2 and Eq. 6.3 it is apparent that the detection sensitivity limitation due to shot noise scales with the probe power as $\left(\frac{\Delta I}{I}\right)_{\text{min,shot}} \sim 1/\sqrt{P}$, thus decreases with an increase of power. This is depicted in the calculation in Fig. 6.8 where typical parameters of the experiment were used for the calculation of the sensitivity. The red line shows the actual experimental parameters as used before. However, an increase of probe power carries the risk of photodamaging the sample material, and thus, was not an option to increase the SNR. Furthermore, additional noise components of the measurement signal can not be reduced by this way and limit the detection sensitivity as some probe power level.

Comparing the theoretically calculated shot noise limited detection sensitivity and the actual sensitivity measured with the fiber laser which was calculated via the standard deviation of the noise floor, it can be noted that there is roughly a factor 2 difference between both. Additional noise components beside the shot noise can originate from residual RIN of the laser source or electronic noise of the detection devices.

Comparing the sensitivity of both the fiber laser and the Ti:Sa setup as shown in Fig. 6.6 an improved sensitivity of roughly a factor 4 can be derived. This is important in the case of detecting small structures exhibiting small TiSCAT signal as will be shown in the next chapter.

4 Conclusion

In summary, time-resolved TiSCAT measurements were carried out on single-layer $MoSe_2$ to identify the decay dynamics of the excitonic states in the semiconductor. The layer number of the investigated flake was verified by PL microscopy as $MoSe_2$ shows photon emittance only for the case of a single-layer. The TiSCAT technique showed basically the same features of the material like PL imaging as wrinkles, holes or cracks but also gives the opportunity to investigate indirect semiconductors as it is not limited to photo emissive states.

The spectral position of the A-excitonic peak was determined by TiSCAT spectroscopy to be at 785 nm in form of a photoinduced bleaching signal in accordance to previous reports investigating $MoSe_2$. Additionally, on the red-shifted side of the excitonic feature a second signal contribution was found exhibiting photoinduced absorption.

By making use of the fiber laser system the detection sensitivity could be improved nearly to the limit of shot noise. With this, the photoinduced absorption feature in single-layer $MoSe_2$ starting at 810 nm was found to cover the whole spectral range up to over 940 nm exhibiting a decreasing signal amplitude to higher wavelengths. The temporal decay of theses excited states could be resolved in the range up to 100 ps revealing a bi-exponential decay attributed to electronic and phononic relaxation. The initial decay additionally showed a damped oscillatory component which is assigned to a coherent phonon mode.

The uniformity and photostability of $MoSe_2$ was utilized to determine the sensitivity of both laser systems. The fiber laser was found to be capable of carrying out nearly shot noise limited measurements of the pump induced changes in detected intensity down to $\Delta I/I = 2.4 \cdot 10^{-6}$ whereas the Ti:Sa laser exhibits a lower sensitivity by the factor of 4. This was found to mainly originate from differences in the relative intensity noise of both laser systems and the additional noise which is introduced by the supercontinuum generation of the Ti:Sa setup.

Chapter 7

Measurements on single (6,4) SWCNTs

The following chapter is based on the paper *"Wavelength-Tunable Ultrafast Two Arm Fiber Laser System for Transient Interferometric Scattering Microscopy on Nanoscopic Objects"* that has been published in the *Journal of the Optical Society of America B* 41.2 (2024)[151].

In this chapter TiSCAT measurements on single semiconducting (6,4) SWCNTs will be presented. With a diameter of 6.83 Å (see section 2.1) this type of nanotube is one of the thinnest SWCNT chiralities which are stable when free-standing as the thinnest possible diameter was reported to be approximately 4.4 Å[187, 188]. The absorption cross section of single-walled carbon nanotubes was empirically found to approximately scale inversely with the diameter[189] which makes it particularly challenging to observe thin nanotubes with the TiSCAT technique. In the following, PL and TiSCAT measurements on a single (6,4) carbon nanotube will be shown utilizing the fiber laser setup. The continuously wavelength-tunable probe arm shall be used to extract spectrally resolved absorption measurements of a single nanotube and the results will be discussed with respect to the emission spectrum.

1 TiSCAT microscopy

The sample material containing the separated (6,4) SWCNTs was prepared by aqueous two-phase separation as described in section 3.3 and applied to a glass cover slide by spincoating. Single nanotubes were identified by PL microscopy and their chiralitiy was determined by the emission spectrum which is depicted in Fig. 7.2 as orange data curve. The peak emission is located at 1.38 eV which translates to a

center wavelength of 900 nm in accordance to the reported emission wavelength of ATP separated (6,4) SWCNTs in solution[114].
An additional emission peak is located at 1.28 eV (≙ 970 nm) which is assigned to defect emission[190]. This could be a consequence of the separation process of the carbon nanotubes or due to the irradiation with the excitation pulses as already seen by Harutyunyan et al. for this type of nanotube[190]. The second point emphasizes the importance of minimizing the laser power utilized in the experiment. Over the measurement time no significant bleaching of the PL intensity was observed. The calculated PL quantum yield is roughly in the order of $1 \cdot 10^{-5}$ which is less than previously reported for this chirality[56]. Low quantum yield is mainly assigned to nonradiative decay of energetically favourable excitonic dark states[49]. Another reason could be due to nonradiative decay at defects as a strong defect emission is visible in the PL spectrum. Other nonradiative decay channels could also arise from PL quenching because of coupling of the excitons to the polar glass substrate [191].

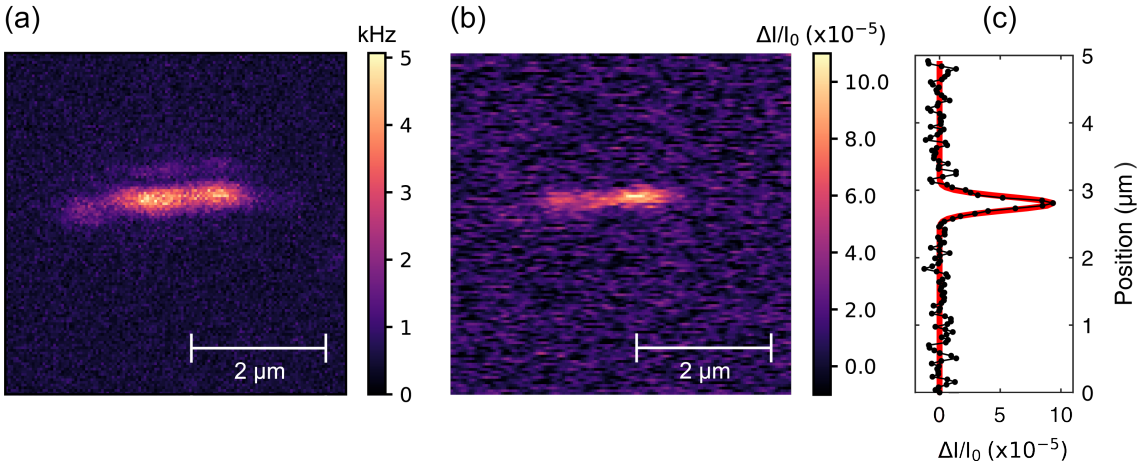

Figure 7.1: a) Confocal photoluminescence and b) transient interferometric scattering image of a single (6,4) SWCNT on glass. c) Cross section of the TiSCAT image shown in b). The fit of a Gaussian function (red line) to the cross section exhibits a FWHM of 234 nm. Reprinted with permission from [151] © Optical Society of America.

For TiSCAT imaging a single SWCNT with parallel orientation with respect to the laser polarization was chosen in order to get maximum absorption. The pump and probe power were set to approximately 1.4 µW to prevent the nanotube from photodamaging. The PL and TiSCAT images are depicted in Fig. 7.1 where the same single nanotube can be observed in both images. All pump-probe measurements on single (6,4) SWCNTs were done utilizing the fiber laser setup since the relative intensity noise of the Ti:Sa setup was not sufficient for an acceptable signal-to-noise

ratio at this probe wavelength.
The spatial resolution of the TiSCAT experiment can be determined from the cross-section taken perpendicular to the nanotube axis. Assuming a point-like thickness of the tube axis the resolution was determined by fitting a Gaussian function to the data (see Fig. 7.1c). Thereby, a spatial resolution of 234 nm was found, slightly higher than the theoretical prediction assuming optimum focusing conditions of 208 nm (see Eg. 6.1).
Figure 7.2a) shows a typical TiSCAT transient measured on the single nanotube shown in Fig. 7.1. Comparing the standard deviation of the noise floor with the highest signal amplitude, a signal-to-noise ratio of 23 was achieved with a sensitivity in the order of $3 \cdot 10^{-6}$. This is sufficient for further measurements which are slightly off-resonant of the transition energy and allow for spectrally resolved measurements of the E_{11} transition as shown in the next section.
The signal decay can be modeled by combining contributions from ultrafast EEA and non-radiative exponential decay and was found to be significantly shorter than the typical times observed for single (6,5) SWCNTs as shown in chapter 5. For the present transient a diffusional time of 140 fs contributed to EEA and an exponential decay time of 3.4 ps were determined. This comparatively fast signal decay could be due to a higher defect density caused by the separation process which leads to an increased non-radiative decay rate. Another reason could be the coupling of the nanotubes to the polar glass substrate leading to quenching of the excitons as already stated above[191]. The measurements on the (6,5) SWCNTs were carried out with a small layer of polystyrene between the glass substrate and the carbon nanotubes which was intended to decouple both and decrease the rate of non-radiative decay channels. This procedure was not successful in the case of the ATP separated (6,4) SWCNTs which could be due to the different solvent of the raw solution which prevented the nanotubes from adhesion to the substrate surface.

2 Transient absorption spectrum

The transient absorption spectra of single (6,4) carbon nanotubes were measured by step-by-step wavelength tuning of the center wavelength of the probe arm as shown in Fig. 7.2b) as blue data points. The absorption spectrum was extracted from the maximum amplitude of the corresponding TiSCAT signal at each probe wavelength. Additionally, the PL spectrum is shown in the figure as an orange curve. The PL data was smoothed via a moving average filter for a better visibility of the peak.
The data points are fitted with an Voigt function which is calculated as the con-

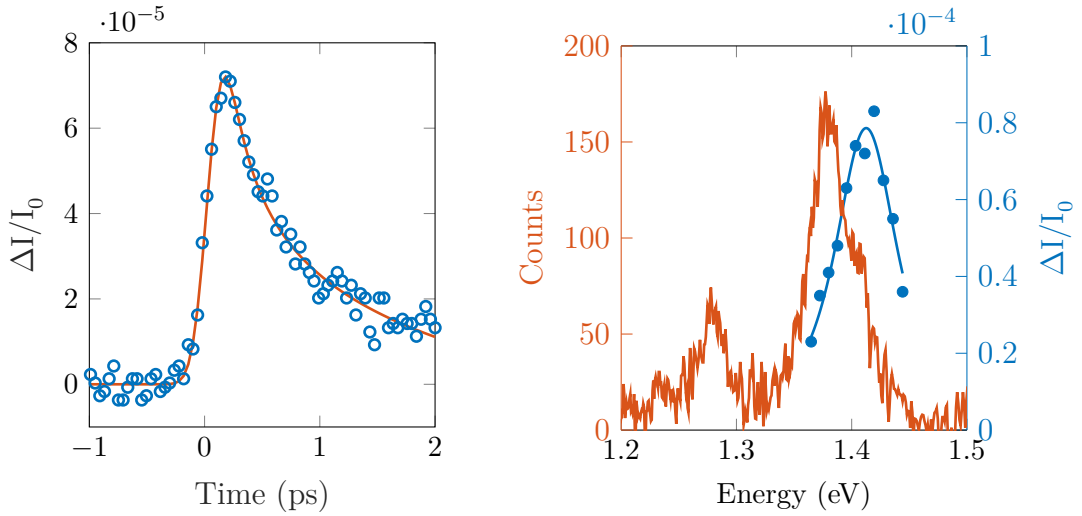

(a) TiSCAT transient of a single (6,4) SWCNT.

(b) PL- and TiSCAT-spectrum.

Figure 7.2: a) TiSCAT transient of a single (6,4) SWCNT probed at 880 nm (blue circles) together with the corresponding fit (orange curve). b) Photoluminescence spectrum (orange line) and absorption spectrum (blue data points) of a single (6,4) SWCNT. The absorption is fitted via a Voigt-fit (blue line). The PL spectrum was smoothed via a moving average filter for a better visibility of the peak. Adapted with permission from [151] © Optical Society of America.

volution of a Gaussian distribution function and a Lorentzian distribution function commonly used for the interpretation of spectroscopic measurements of Doppler-broadened spectra[192]. This model function is chosen because the measured signal results from a convolution of the tuned laser spectra which have a bandwidth of approximately 13 nm and the absorption spectrum which is assumed to exhibit a Lorentzian shape. The measured spectrum reveals a Stokes shift of 30 meV between the photoluminescence peak and the absorption peak which is in accordance with previously reported values up to 40 meV for nanotubes of comparable diameter[193] but large in comparison to reported values for SWCNTs in solution in the order of several meV [52] which can be assigned to defects or doping by different sorts of atoms like oxygen[194]. This assumption is supported by the detected emission peak of defects found in the PL spectrum of the single SWCNT shown in Fig.7.2b as mentioned before.

3 Conclusion

In this chapter time-resolved TiSCAT and PL measurements on single semiconducting (6,4) SWCNTs were shown. It has been demonstrated that the TiSCAT technique is capable of the detection of exceptionally thin nanotubes which is particularly challenging due to their small absorption cross section.
From a crosssection perpendicular to the nanotube axis the spatial resolution of the TiSCAT measurement setup was found to be 234 nm which is slightly higher than the theoretical prediction for optimal focusing conditions.
The pointing stability and a sufficient sensitivity of the fiber laser system was utilized for spectrally resolved TiSCAT measurements on a single (6,4) SWCNT revealing the shape of the absorption peak of the E_{11} transition. The corresponding PL spectrum of the same nanotube was determined revealing a Stokes shift of 30 meV between the absorption and the emission peak which is higher than reported for pristine SWCNTs in solution. This was attributed to an increased Stokes shift due to the influence of defects. This in agreement with the observed defect emission peak in the photoluminescence spectrum.

Chapter 8

Summary

In this work, the ultrafast dynamics of excited states of single nanostructures were investigated by transient interferometric scattering (TiSCAT) microscopy and time-resolved photoluminescence microscopy.
Due to their small scattering cross section and low damage threshold, small nanoparticles cannot be detected by common scattering light microscopy. Conventionally used techniques for time-resolved investigations on these particles predominantly make use of time-correlated single photon counting (TCSPC) which shows unrivaled sensitivity. However, it lacks of the temporal resolution necessary for investigations of the initial decay mechanisms right after excitation which thus remain hidden. Typically, less sensitive pump-probe experiments are carried out on ensembles unable to resolve spatial variations caused by defects or doping. However, the low photostability of most nanoscale objects limits the pump and probe fluences which can be applied.
For this reasons, the aim of this work was the combination of two measurement techniques bringing together the temporal resolution of a pump-probe scheme and the sensitivity of the detection method of interferometric scattering (iSCAT). Unifying these resulted in the *transient interferometric scattering* (TiSCAT) technique.
To do so, the experimental segment of this work is split into two separate parts: In the first section the **development and characterisation of a two-color fiber laser** is shown which acts as the laser source of the TiSCAT experiment additionally to the previously existing Ti:Sa setup. This was intended to improve the sensitivity of the measurement. The second part presents the **microscopic investigation of single nanoobjects** on the example of single SWCNTs and monolayer $MoSe_2$.

The development of the fiber laser had the aim of a continuously wavelength-tunable pulsed light source with low intensity noise level tailored for pump-probe measure-

ments in the NIR. For this purpose the nonlinear effect of soliton self-frequency shift was utilized to shift the laser pulses initially centered at 1560 nm to higher wavelengths up to 1920 nm. The subsequent frequency doubling creates pulses adjustable in the range of 810 nm to 960 nm which act as the probe arm. The pump arm is seeded by the same fiber oscillator at 1560 nm and frequency doubled to 780 nm. Both arms exhibit a temporal pulse width in the order of 90 fs (FWHM) in the unchirped case. The pump arm is pre-chirped in order to compensate for the chromatic dispersion of the optical components of the microscope and yields the shortest pulse width at the position of the sample. The temporal resolution of the measurement was investigated by cross-correlation of both arms and exhibited a temporal width of 285 fs (FWHM) suitable for the investigation of sub-ps decay processes.

Time-resolved microscopy was carried out on individual (6,5) SWCNTs utilizing TiSCAT and PL microscopy to investigate the exciton decay dynamics. Time traces of the excited state population were taken for the same nanotubes showing tube-to-tube variations in the decay dynamics. Whereas the PL transients could be described by mono-exponential decays with lifetimes in the range of 5 ps to 48 ps the TiSCAT transients showed a more complex behaviour. This could be attributed to early exciton-exciton annihilation (EEA) shortly after the excitation which is not observable in a PL measurement. The analytical model proposed by Srivastava and Kono[65] combining EEA and the exponential lifetime of the single excitons was utilized to describe the obtained data from the PL and TiSCAT measurement. This is the first report of a unified model describing the pump-probe and PL transients of individual SWCNTs.
The influence of EEA was further investigated by tuning of the excitation power and thus of the exciton density. The initial fast decay component was found to speed up with increasing exciton number from approximately 1 ps to 200 fs. This is in agreement with numerical calculations including the excitation geometry and previously reported values for the absorption cross section and diffusion coefficient of this type of nanotube.
Monte-Carlo simulations of the decay dynamics were carried out to investigate the origin of tube-to-tube variations and the influence of finite and quantized exciton numbers in the case of low excitation powers. The influence of spatial variations of the exciton energy along the nanotube was implemented representing local defects. A significant increase of the EEA rate was observed for local minima of the energetic landscape supporting the suggested concept.
Spectrally resolved TiSCAT measurements were performed on single-layer $MoSe_2$ on

glass covered with hBN to investigate different decay components of the excitons. At 785 nm a photobleaching signal has been observed arising from the A-exciton optical transition due to Pauli-blocking. Photoinduced absorption was found to take place at longer wavelengths covering the whole spectral range between 810 nm and 940 nm which could be assigned to bandgap renormalization and electronic and phononic relaxation upon pulsed excitation. For the latter two effects exponential decay times of 3 ps and 22 ps where found, respectively.
$MoSe_2$ was used to characterize the sensitivity of the TiSCAT setup for both utilized laser systems. By making use of the fiber laser system developed in the first part of the work, the sensitivity could be improved by a factor of 4 in contrast to the existing Ti:Sa setup. This was found to originate in the supercontinuum generation which introduces relative intensity noise 45 $\frac{\mathrm{dBc}}{\mathrm{Hz}}$ above the noise level of the fiber laser probe arm.
The calculation of the shot noise level which represents the fundamental limit in the sensitivity of this measurement was found to be in the order of the experimentally achieved sensitivity within a factor of 2. This could be due to residual noise of the detection electronics or the laser system.

The improved TiSCAT detection sensitivity was used to investigate (6,4) SWCNTs utilizing the fiber laser. Single nanotubes could be imaged in PL as well as in TiSCAT microscopy confirming the high detection sensitivity reported from the measurements on single-layer $MoSe_2$. A signal-to-noise ratio of 23 with a sensitivity of $3 \cdot 10^{-6}$ was achieved for the measurement on a single nanotube at its E_{11} transition. The tunability of the probe arm was used to extract the transient absorption spectrum of the single nanotube. The comparison with the PL emission spectrum showed a remarkably large Stokes shift of 30 meV which could be attributed to the influence of defects as their characteristic emission was visible in the PL emission spectrum.

To sum up, the TiSCAT setup containing the fiber laser has been shown to be capable of time-resolved measurements on single nanoobjects at nearly shot noise limited detection sensitivity. With this, fast decay dynamics could be investigated which were connected to the observed PL decay, combining both in a unified model. Further improvement of the spatial resolution of the microscope could be possible by including a near-field probe to the setup. This would allow for further investigations of spatial variations of the initial decay dynamics of single nanoobjects. In particular, this would enable further investigations of the suggested speed up of the exciton decay due to the presence of local defects in the performed Monte-Carlo simulations.

Appendix A

Dispersion correction of TA spectroscopy

The measurement data and analysis procedure presented in this section of the Appendix was provided by Lucas Lange and is shown with his kind permission.

For transient absorption spectroscopy as shown in chapter 6 a supercontinuum was generated (see chapter 3) which served as a probe pulse covering a broad spectral range. After transmission through the microscope optics, e.g. the objective, the laser pulses have accumulated chromatic dispersion which translates to a temporal delay between the spectral components of the probe pulse.

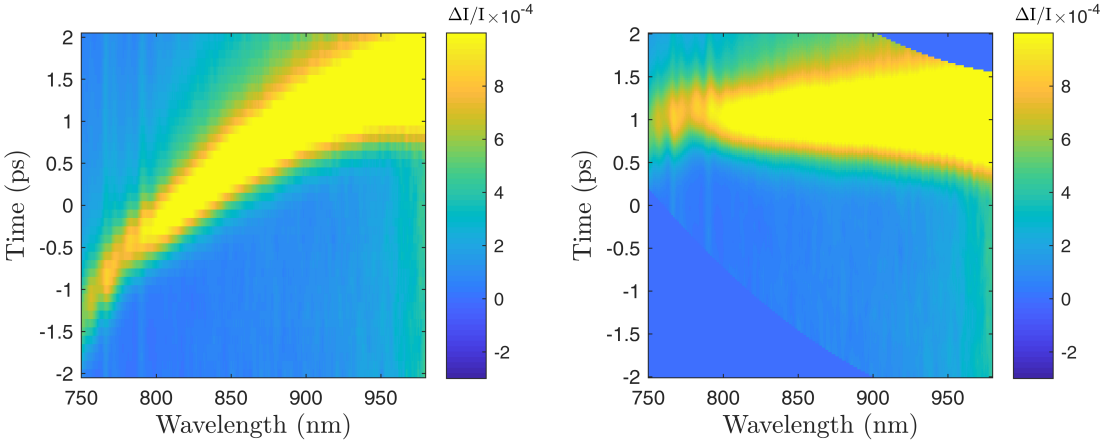

(a) Uncorrected TA spectrum.

(b) Corrected TA spectrum.

Figure A.1: TA spectroscopy on graphene used for dispersion correction. The uncorrected measurement data in a) was processed such that the peaks of all spectral components overlap in time (b).

To account for this additional temporal delay a transient absorption spectroscopy measurement on graphene was carried out. Due to its quasi instantaneous and spec-

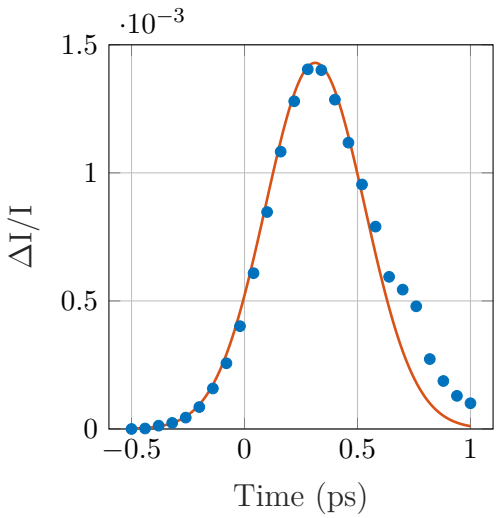

Figure A.2: TA transient on graphene for a probe wavelength of 880 nm extracted from the data shown in Fig. A.1b depicted in blue. The corresponding Gaussian fit function with a width of 582 fs (FWHM) is shown in orange.

trally broad absorption response upon pulsed excitation, it served as the chromatic dispersion measure of the setup for subsequent measurements and is depicted in figure A.1a.

As shown in Fig. A.1b, the temporal peak position of every wavelength component was determined and the corresponding data was subsequently shifted to the same temporal position. This method was applied for all transient absorption spectroscopy measurements preventing misinterpretation of decay dynamics due to the chromatic dispersion of the measurement setup.

Furthermore, the data shown in Fig. A.1 was used to extract TA transients for single wavelength components. Assuming a instantaneous response of graphene, the TA transient represents the cross-correlation trace of the pump and probe pulses and thus the IRF of the measurement system. The extracted width of the IRF was used for fitting of the model function to the measurement data as shown in chapter 5. In figure A.2 the transient corresponding to a probe wavelength of 880 nm is depicted in blue. Assuming a Gaussian pulse shape (depicted in orange) a FWHM of 582 fs was extracted which was used for the convolution with the model function in chapter 5.

Appendix B

Monte-Carlo simulation code

```
# -*- coding: utf-8 -*-
"""
Created on Fri May 24 21:10:35 2019

@author: Achim Hartschuh and Konrad Birkmeier
Monte-Carlo simulation of
population decay of CNTs including EEA and exponential decay
in the presence of localization centers
"""
import numpy as np
import random
import pylab as plt

#step size in nm
Dx = 1;
#time step in fs
dt=0.1;
#diffusion constant in cm^2/s
D=7;
#Total simulation time in fs
Time=5000;
#lifetime (1/e) of exciton in fs
lifetime=20000;
#Number of initially generated excitons
N=10;
#focus radius in nm
focus_width=721/2;
#Length of CNT in nm
LCNT=1000;
```

```
#number of experiments
pulses=500;
#distance for EEA in nm
EEA_distance=5;
#Exciton-exciton annihilation on / off
EEA=1;
#switch trap on/off
Trap=1;


#mean square displacement per dt in nm
msd=np.sqrt(2*D*dt*1E-19)*1E9;
#pixelnumber
L=int(LCNT/Dx);
#Probability for diffusive step per time-step in one direction
ps = (msd/Dx)*(1/2);
#number of iteration steps
ts=int(round((Time/dt)*(msd/Dx)));
#time_inteval of each step in fs
time_interval=Time/ts;
#Probability for decay per time-step
pd=1-np.exp(-(time_interval)/lifetime)
#localization at
xlocal = 1*L/2; #location of trap
trap=Trap*100; #depth of trap in meV
wtrap=25; #width of trap in nm
wtrap=wtrap/Dx;

#Index of excitons
nexc=np.linspace(1,N,N);
#Exciton coordinates
x=np.zeros((N),dtype=int);

pindex=0;
exctotal=np.zeros((ts),dtype=int);
local=0
```

```
#x-axis in nm
xaxis=np.linspace(0,LCNT,int(LCNT/Dx)+1);
pos=np.zeros((L+1),dtype=float)
init_pos=np.zeros((L+1),dtype=float)

#center of normal distribution for random exc. allocation
mu=L/2
#width of normal distribution
sigma=2*(focus_width/Dx)/6

E=np.zeros((L+1),dtype=float);
dE=np.zeros((L+1),dtype=float);
psr=np.zeros((L+1),dtype=float);
psl=np.zeros((L+1),dtype=float);
z=0;
while z < len(xaxis): #energy landscape along CNT
    E[z]=-trap*np.exp(-(xaxis[z]-xlocal*Dx)**2/(2.0*wtrap**2));
    z+=1

z=0;
while z < len(xaxis)-1: #derivative of E
    dE[z]=E[z+1]-E[z-1];
    z+=1

z=0;
while z < len(xaxis): #probability for step to the right/left
    psr[z]=((2*ps)/(1+np.exp(dE[z]/25)));
    psl[z]=((2*ps)/(1+np.exp(-dE[z]/25)));
    z+=1


while pindex < pulses:
    #Exciton state
    s=np.ones((N),dtype=int);
    #Initial exciton population
    xint=np.zeros((L),dtype=float)
```

```
m=0;
while m < N:
 #random allocation of exciton positions by normal distribution
    x[m]=int(np.random.normal(mu, sigma, 1)[0])
    if x[m]>L-1:#repeat step if exciton is out of CNT length
        m=m-1
    m+=1
l=0
#counting of excitons for every step at pos x
while l<N:
    init_pos[x[l]]=init_pos[x[l]]+1
    l=l+1
t=0;
exc=np.zeros((ts),dtype=int);
while t < ts:
    m=0;
    while m < N:
        if (s[m] > 0):
            branch=random.uniform(0,1);
            if (branch < psr[x[m]]):
                x[m]=x[m]+1;
            if (branch > 1-psl[x[m]]):
                x[m]=x[m]-1;
            decay=random.random();
            if (decay < pd):
                s[m]=0;
            if (x[m] == L):
                s[m]=0;
            if (x[m] == 0):
                s[m]=0;
        m+=1;
    m=0;
    if EEA == 1:
        while m < N:
            n=0;
            while n < N:
                if (m != n):
```

```
                    #check for distance between excitons
                        if ((abs(x[m]-x[n])*Dx)<EEA_distance):
                        #if (x[m]==x[n]):
                            if (s[m] == 1):
                                if (s[n] == 1):
                                    s[m]=0;
                                    s[n]=0;
                    n+=1;
                m+=1;
        exc[t]=np.sum(s)
        t+=1;

    l=0
    while l<N:
     #counting of excitons for every step at pos x
        pos[x[l]]=pos[x[l]]+1
        l=l+1
    pindex+=1;
    exctotal=exctotal+exc;
    print('Pulse:', pindex,'/',pulses)

plt.figure(1)
time=np.linspace(0,Time/1000,len(exctotal)); #time axis in ps
plt.plot(time,exctotal/pulses/N)
plt.xlabel("Time (ps)")
plt.ylabel("Norm. exciton number (a.u.)")
print('Ende')
```

Bibliography

[1] X. Li, W. Cai, J. An, S. Kim, J. Nah, D. Yang, R. Piner, A. Velamakanni, I. Jung, E. Tutuc, S. K. Banerjee, L. Colombo, and R. S. Ruoff. "Large-area synthesis of high-quality and uniform graphene films on copper foils". In: *Science* 324.5932 (2009), pp. 1312–1314.

[2] J. Gao, F. Liu, Y. Liu, N. Ma, Z. Wang, and X. Zhang. "Environment-Friendly Method To Produce Graphene That Employs Vitamin C and Amino Acid". In: *Chem. Mater.* 22.7 (2010), pp. 2213–2218.

[3] G. Fiori, F. Bonaccorso, G. Iannaccone, T. Palacios, D. Neumaier, A. Seabaugh, S. K. Banerjee, and L. Colombo. "Electronics based on two-dimensional materials". In: *Nat. Nanotechnol.* 9.10 (2014), pp. 768–779.

[4] Y.-M. Lin, C. Dimitrakopoulos, K. A. Jenkins, D. B. Farmer, H.-Y. Chiu, A. Grill, and P. Avouris. "100-GHz Transistors from Wafer-Scale Epitaxial Graphene". In: *Science* 327.5966 (2010), p. 662.

[5] G. E. Moore. "Cramming more components onto integrated circuits". In: *Electronics* 38.8 (1965), pp. 114–117.

[6] *The Nobel Prize in Physics 2010: Nobel Prize Outreach AB 2021.* URL: `https://www.nobelprize.org/prizes/physics/2010/summary/`.

[7] M. Kinoshita, M. Steiner, M. Engel, J. P. Small, A. A. Green, M. C. Hersam, R. Krupke, E. E. Mendez, and P. Avouris. "The polarized carbon nanotube thin film LED". In: *Opt. Express* 18.25 (2010), pp. 25738–25745.

[8] T. Dürkop, S. A. Getty, E. Cobas, and M. S. Fuhrer. "Extraordinary Mobility in Semiconducting Carbon Nanotubes". In: *Nano Lett.* 4.1 (2004), pp. 35–39.

[9] M. Meyyappan. "Carbon Nanotube-Based Chemical Sensors". In: *Small* 12.16 (2016), pp. 2118–2129.

[10] G. Gruner. "Carbon nanotube transistors for biosensing applications". In: *Anal. Bioanal. Chem* 384.2 (2006), pp. 322–335.

[11] E. A. Stepanov, S. V. Semin, C. R. Woods, M. Vandelli, A. V. Kimel, K. S. Novoselov, and M. I. Katsnelson. "Direct Observation of Incommensurate-Commensurate Transition in Graphene-hBN Heterostructures via Optical Second Harmonic Generation". In: *ACS Appl. Mater. Interfaces* 12.24 (2020), pp. 27758–27764.

[12] D. Oron, D. Yelin, E. Tal, S. Raz, R. Fachima, and Y. Silberberg. "Depth-resolved structural imaging by third-harmonic generation microscopy". In: *J. Struct. Biol.* 147.1 (2004), pp. 3–11.

[13] T. Gokus, A. Hartschuh, H. Harutyunyan, M. Allegrini, F. Hennrich, M. Kappes, A. A. Green, M. C. Hersam, P. T. Araújo, and A. Jorio. "Exciton decay dynamics in individual carbon nanotubes at room temperature". In: *Appl. Phys. Lett.* 92.15 (2008), p. 153116.

[14] C. W. Freudiger, W. Yang, G. R. Holtom, N. Peyghambarian, X. S. Xie, and K. Q. Kieu. "Stimulated Raman scattering microscopy with a robust fibre laser source". In: *Nat. Photonics* 8.2 (2014), pp. 153–159.

[15] J.-P. Yang, M. M. Kappes, H. Hippler, and A.-N. Unterreiner. "Femtosecond transient absorption spectroscopy of single-walled carbon nanotubes in aqueous surfactant suspensions: Determination of the lifetime of the lowest excited state". In: *Phys. Chem. Chem. Phys.* 7.3 (2005), pp. 512–517.

[16] D. Polli, L. Lüer, and G. Cerullo. "High-time-resolution pump-probe system with broadband detection for the study of time-domain vibrational dynamics". In: *Rev. Sci. Instrum.* 78.10 (2007), p. 103108.

[17] P. Kukura, H. Ewers, C. Müller, A. Renn, A. Helenius, and V. Sandoghdar. "High-speed nanoscopic tracking of the position and orientation of a single virus". In: *Nat. Methods* 6.12 (2009), pp. 923–927.

[18] V. Jacobsen, P. Stoller, C. Brunner, V. Vogel, and V. Sandoghdar. "Interferometric optical detection and tracking of very small gold nanoparticles at a water-glass interface". In: *Opt. Express* 14.1 (2006), pp. 405–414.

[19] T. D. Gokus. "Time-Resolved Photoluminescence and Elastic White Light Scattering Studies of Individual Carbon Nanotubes and Optical Characterization of Oxygen Plasma Treated Graphene". Doctoral dissertation. München: Ludwig-Maximilians-Universität München, 2011.

[20] S. Iijima. "Helical microtubules of graphitic carbon". In: *Nature* 354.6348 (1991), pp. 56–58.

[21] Z. P. Huang, J. W. Xu, Z. F. Ren, J. H. Wang, M. P. Siegal, and P. N. Provencio. "Growth of highly oriented carbon nanotubes by plasma-enhanced hot filament chemical vapor deposition". In: *Appl. Phys. Lett.* 73.26 (1998), pp. 3845–3847.

[22] L. Delzeit, C. V. Nguyen, R. M. Stevens, J. Han, and M. Meyyappan. "Growth of carbon nanotubes by thermal and plasma chemical vapour deposition processes and applications in microscopy". In: *Nanotechnology* 13.3 (2002), pp. 280–284.

[23] Y. Zhang and S. Iijima. "Formation of single-wall carbon nanotubes by laser ablation of fullerenes at low temperature". In: *Appl. Phys. Lett.* 75.20 (1999), pp. 3087–3089.

[24] S. Reich, C. Thomsen, and J. Maultzsch. *Carbon Nanotubes: Basic Concepts and Physical Properties*. 1st ed. Berlin: Wiley-VCH, 2004.

[25] A. Takakura, K. Beppu, T. Nishihara, A. Fukui, T. Kozeki, T. Namazu, Y. Miyauchi, and K. Itami. "Strength of carbon nanotubes depends on their chemical structures". In: *Nat. Commun.* 10.1 (2019), p. 3040.

[26] R. Saito, G. Dresselhaus, and M. S. Dresselhaus. *Physical Properties Of Carbon Nanotubes*. London: Imperial College Press, 1998.

[27] F. Ducastelle, X. Blase, J.-M. Bonard, J.-C. Charlier, and P. Petit. "Electronic Structure". In: *Understanding Carbon Nanotubes*. Ed. by R. Beig, W. Beiglböck, W. Domcke, B.-G. Englert, U. Frisch, P. Hänggi, G. Hasinger, K. Hepp, W. Hillebrandt, D. Imboden, R. L. Jaffe, R. Lipowsky, H. v. Löhneysen, I. Ojima, D. Sornette, S. Theisen, W. Weise, J. Wess, J. Zittartz, A. Loiseau, P. Launois, P. Petit, S. Roche, and J.-P. Salvetat. Lect. Notes Phys. Berlin, Heidelberg: Springer Berlin Heidelberg, 2006, pp. 199–276.

[28] S. Reich, J. Maultzsch, C. Thomsen, and P. Ordejón. "Tight-binding description of graphene". In: *Phys. Rev. B* 66.3 (2002), p. 035412.

[29] R. Balog, B. Jørgensen, L. Nilsson, M. Andersen, E. Rienks, M. Bianchi, M. Fanetti, E. Laegsgaard, A. Baraldi, S. Lizzit, Z. Sljivancanin, F. Besenbacher, B. Hammer, T. G. Pedersen, P. Hofmann, and L. Hornekaer. "Bandgap opening in graphene induced by patterned hydrogen adsorption". In: *Nat. Mater.* 9.4 (2010), pp. 315–319.

[30] K. S. Novoselov, A. K. Geim, S. V. Morozov, D. Jiang, M. I. Katsnelson, I. V. Grigorieva, S. V. Dubonos, and A. A. Firsov. "Two-dimensional gas of massless Dirac fermions in graphene". In: *Nature* 438.7065 (2005), pp. 197–200.

[31] J. W. Mintmire and C. T. White. "Universal Density of States for Carbon Nanotubes". In: *Phys. Rev. Lett.* 81.12 (1998), pp. 2506–2509.

[32] C. Kittel. *Einführung in die Festkörperphysik*. 14th ed. München: Oldenbourg, 2006.

[33] C. T. White and J. W. Mintmire. "Density of states reflects diameter in nanotubes". In: *Nature* 394.6688 (1998), pp. 29–30.

[34] G. Seol, Y. Yoon, J. Fodor, J. Guo, A. Matsudaira, D. Kienle, G. Liang, G. Klimeck, M. Lundstrom, and A. Saeed. *CNTbands*. 2019. URL: `https://nanohub.org/resources/cntbands-ext`.

[35] H. Kataura, Y. Kumazawa, Y. Maniwa, I. Umezu, S. Suzuki, Y. Ohtsuka, and Y. Achiba. "Optical Properties of Single-Wall Carbon Nanotubes". In: *Synth. Met.* 103.1-3 (1999), pp. 2555–2558.

[36] H. Ajiki. "Magneto-optical spectra of carbon nanotubes: effect of Aharonov–Bohm flux on depolarization effect". In: *Phys. B: Condens. Matter* 323.1-4 (2002), pp. 206–208.

[37] H. Ajiki and T. Ando. "Aharonov-Bohm effect in carbon nanotubes". In: *Phys. B: Condens. Matter* 201 (1994), pp. 349–352.

[38] F. Wang, G. Dukovic, L. E. Brus, and T. F. Heinz. "The Optical Resonances in Carbon Nanotubes Arise from Excitons". In: *Science* 308.5723 (2005), pp. 838–841.

[39] E. Malić, M. Hirtschulz, F. Milde, M. Richter, J. Maultzsch, S. Reich, and A. Knorr. "Coulomb effects in single-walled carbon nanotubes". In: *Phys. Status Solidi* 245.10 (2008), pp. 2155–2158.

[40] M. S. Dresselhaus, G. Dresselhaus, R. Saito, and A. Jorio. "Exciton Photophysics of Carbon Nanotubes". In: *Annu. Rev. Phys. Chem.* 58 (2007), pp. 719–747.

[41] J. Maultzsch, R. Pomraenke, S. Reich, E. Chang, D. Prezzi, A. Ruini, E. Molinari, M. S. Strano, C. Thomsen, and C. Lienau. "Exciton binding energies in carbon nanotubes from two-photon photoluminescence". In: *Phys. Rev. B* 72.24 (2005), p. 241402.

[42] C. L. Kane and E. J. Mele. "Ratio Problem in Single Carbon Nanotube Fluorescence Spectroscopy". In: *Phys. Rev. Lett.* 90.20 (2003), p. 207401.

[43] R. Matsunaga, K. Matsuda, and Y. Kanemitsu. "Origin of low-energy photoluminescence peaks in single carbon nanotubes: K -momentum dark excitons and triplet dark excitons". In: *Phys. Rev. B* 81.3 (2010).

[44] C. Manzoni, A. Gambetta, E. Menna, M. Meneghetti, G. Lanzani, and G. Cerullo. "Intersubband Exciton Relaxation Dynamics in Single-Walled Carbon Nanotubes". In: *Phys. Rev. Lett.* 94.20 (2005), p. 207401.

[45] M. Kasha. "Characterization of electronic transitions in complex molecules". In: *Discuss. Faraday Soc.* 9 (1950), pp. 14–19.

[46] J. Crochet, M. Clemens, and T. Hertel. "Quantum Yield Heterogeneities of Aqueous Single-Wall Carbon Nanotube Suspensions". In: *J. Am. Chem. Soc.* 129.26 (2007), pp. 8058–8059.

[47] M. J. O'Connell, S. M. Bachilo, C. B. Huffman, V. C. Moore, M. S. Strano, E. H. Haroz, K. L. Rialon, P. J. Boul, W. H. Noon, C. Kittrell, J. Ma, R. H. Hauge, R. B. Weisman, and R. E. Smalley. "Band Gap Fluorescence from Individual Single-Walled Carbon Nanotubes". In: *Science* 297.5581 (2002), pp. 593–596.

[48] J. Lefebvre, D. G. Austing, J. Bond, and P. Finnie. "Photoluminescence Imaging of Suspended Single-Walled Carbon Nanotubes". In: *Nano Lett.* 6.8 (2006), pp. 1603–1608.

[49] A. Srivastava, H. Htoon, V. I. Klimov, and J. Kono. "Direct Observation of Dark Excitons in Individual Carbon Nanotubes: Inhomogeneity in the Exchange Splitting". In: *Phys. Rev. Lett.* 101.8 (2008), p. 087402.

[50] F. Wang, G. Dukovic, L. E. Brus, and T. F. Heinz. "Time-Resolved Fluorescence of Carbon Nanotubes and Its Implication for Radiative Lifetimes". In: *Phys. Rev. Lett.* 92.17 (2004), p. 177401.

[51] A. Hagen, G. Moos, V. Talalaev, and T. Hertel. "Electronic structure and dynamics of optically excited single-wall carbon nanotubes". In: *Appl. Phys. A* 78.8 (2004), pp. 1137–1145.

[52] M. Jones, C. Engtrakul, W. K. Metzger, R. J. Ellingson, A. J. Nozik, M. J. Heben, and G. Rumbles. "Analysis of photoluminescence from solubilized single-walled carbon nanotubes". In: *Phys. Rev. B* 71.11 (2005), p. 115426.

[53] M. Zheng, A. Jagota, E. D. Semke, B. A. Diner, R. S. McLean, S. R. Lustig, R. E. Richardson, and N. G. Tassi. "DNA-assisted dispersion and separation of carbon nanotubes". In: *Nat. Mater.* 2.5 (2003), pp. 338–342.

[54] B. Zheng, C. Lu, G. Gu, A. Makarovski, G. Finkelstein, and J. Liu. "Efficient CVD Growth of Single-Walled Carbon Nanotubes on Surfaces Using Carbon Monoxide Precursor". In: *Nano Lett.* 2.8 (2002), pp. 895–898.

[55] J. Lefebvre and P. Finnie. "Photoluminescence and Förster Resonance Energy Transfer in Elemental Bundles of Single-Walled Carbon Nanotubes". In: *J. Phys. Chem. C* 113.18 (2009), pp. 7536–7540.

[56] A. Hagen, M. Steiner, M. B. Raschke, C. Lienau, T. Hertel, H. Qian, A. J. Meixner, and A. Hartschuh. "Exponential Decay Lifetimes of Excitons in Individual Single-Walled Carbon Nanotubes". In: *Phys. Rev. Lett.* 95.19 (2005), p. 197401.

[57] T. Gokus, L. Cognet, J. G. Duque, M. Pasquali, A. Hartschuh, and B. Lounis. "Mono- and Biexponential Luminescence Decays of Individual Single-Walled Carbon Nanotubes". In: *J. Phys. Chem. C* 114.33 (2010), pp. 14025–14028.

[58] V. Perebeinos and P. Avouris. "Phonon and electronic nonradiative decay mechanisms of excitons in carbon nanotubes". In: *Phys. Rev. Lett.* 101.5 (2008), p. 057401.

[59] P. Avouris, J. Chen, M. Freitag, V. Perebeinos, and J. C. Tsang. "Carbon nanotube optoelectronics". In: *Phys. Status Solidi* 243.13 (2006), pp. 3197–3203.

[60] A. A. Tonkikh, V. A. Eremina, E. A. Obraztsova, D. A. Musatov, A. Y. Pereyaslavtsev, E. I. Kauppinen, and E. D. Obraztsova. "Tunable Doping and Characterization of Single-Wall Carbon Nanotube Macrosystems for Electrode Material Applications". In: *ACS Appl. Nano Mater.* 4.3 (2021), pp. 3220–3231.

[61] T. Hertel, S. Himmelein, T. Ackermann, D. Stich, and J. Crochet. "Diffusion Limited Photoluminescence Quantum Yields in 1-D Semiconductors: Single-Wall Carbon Nanotubes". In: *ACS nano* 4.12 (2010), pp. 7161–7168.

[62] J. Chmeliov, J. Narkeliunas, M. W. Graham, G. R. Fleming, and L. Valkunas. "Exciton-exciton annihilation and relaxation pathways in semiconducting carbon nanotubes". In: *Nanoscale* 8.3 (2016), pp. 1618–1626.

[63] Y. Murakami and J. Kono. "Nonlinear Photoluminescence Excitation Spectroscopy of Carbon Nanotubes: Exploring the Upper Density Limit of One-Dimensional Excitons". In: *Phys. Rev. Lett.* 102.3 (2009), p. 037401.

[64] Y.-Z. Ma, L. Valkunas, S. L. Dexheimer, S. M. Bachilo, and G. R. Fleming. "Femtosecond Spectroscopy of Optical Excitations in Single-Walled Carbon Nanotubes: Evidence for Exciton-Exciton Annihilation". In: *Phys. Rev. Lett.* 94.15 (2005), p. 157402.

[65] A. Srivastava and J. Kono. "Diffusion-limited exciton-exciton annihilation in single-walled carbon nanotubes: A time-dependent analysis". In: *Phys. Rev. B* 79.20 (2009), p. 205407.

[66] L. Lüer, S. Hoseinkhani, D. Polli, J. Crochet, T. Hertel, and G. Lanzani. "Size and mobility of excitons in (6, 5) carbon nanotubes". In: *Nat. Phys.* 5.1 (2009), pp. 54–58.

[67] B. Langlois, R. Parret, F. Vialla, Y. Chassagneux, P. Roussignol, C. Diederichs, G. Cassabois, J.-S. Lauret, and C. Voisin. "Intraband and intersubband many-body effects in the nonlinear optical response of single-wall carbon nanotubes". In: *Phys. Rev. B* 92.15 (2015).

[68] Z. Zhu, J. Crochet, M. S. Arnold, M. C. Hersam, H. Ulbricht, D. Resasco, and T. Hertel. "Pump-Probe Spectroscopy of Exciton Dynamics in (6,5) Carbon Nanotubes". In: *The Journal of Physical Chemistry C* 111.10 (2007), pp. 3831–3835.

[69] A. Ishii, H. Machiya, and Y. K. Kato. "High Efficiency Dark-to-Bright Exciton Conversion in Carbon Nanotubes". In: *Phys. Rev. X* 9.4 (2019), p. 041048.

[70] C. Ataca, H. Şahin, and S. Ciraci. "Stable, Single-Layer MX_2 Transition-Metal Oxides and Dichalcogenides in a Honeycomb-Like Structure". In: *J. Phys. Chem. C* 116.16 (2012), pp. 8983–8999.

[71] K. S. Novoselov, D. Jiang, F. Schedin, T. J. Booth, V. V. Khotkevich, S. V. Morozov, and A. K. Geim. "Two-dimensional atomic crystals". In: *Proc. Natl. Acad. Sci. U.S.A.* 102.30 (2005), pp. 10451–10453.

[72] K.-K. Liu, W. Zhang, Y.-H. Lee, Y.-C. Lin, M.-T. Chang, C.-Y. Su, C.-S. Chang, H. Li, Y. Shi, H. Zhang, C.-S. Lai, and L.-J. Li. "Growth of Large-Area and Highly Crystalline MoS_2 Thin Layers on Insulating Substrates". In: *Nano Lett.* 12.3 (2012), pp. 1538–1544.

[73] A. Splendiani, L. Sun, Y. Zhang, T. Li, J. Kim, C.-Y. Chim, G. Galli, and F. Wang. "Emerging Photoluminescence in Monolayer MoS_2". In: *Nano Lett.* 10.4 (2010), pp. 1271–1275.

[74] O. Lopez-Sanchez, D. Lembke, M. Kayci, A. Radenovic, and A. Kis. "Ultrasensitive photodetectors based on monolayer MoS_2". In: *Nat. Nanotechnol.* 8.7 (2013), pp. 497–501.

[75] A. V. Kolobov and J. Tominaga. *Two-Dimensional Transition-Metal Dichalcogenides*. 1st ed. Vol. 239. Springer Series in Materials Science. Cham: Springer International Publishing, 2016.

[76] C. Hsu, R. Frisenda, R. Schmidt, A. Arora, S. M. Vasconcellos, R. Bratschitsch, H. S. J. Zant, and A. Castellanos–Gomez. "Thickness–Dependent Refractive Index of 1L, 2L, and 3L MoS_2, $MoSe_2$, WS_2, and WSe_2". In: *Adv. Optical Mater.* 7.13 (2019), p. 1900239.

[77] K. F. Mak, C. Lee, J. Hone, J. Shan, and T. F. Heinz. "Atomically Thin MoS_2: A New Direct-Gap Semiconductor". In: *Phys. Rev. Lett.* 105.13 (2010), p. 136805.

[78] A. Kuc, N. Zibouche, and T. Heine. "Influence of quantum confinement on the electronic structure of the transition metal sulfide TS_2". In: *Phys. Rev. B* 83.24 (2011), p. 245213.

[79] Z. Y. Zhu, Y. C. Cheng, and U. Schwingenschlögl. "Giant spin-orbit-induced spin splitting in two-dimensional transition-metal dichalcogenide semiconductors". In: *Phys. Rev. B* 84.15 (2011), p. 153402.

[80] W. Yao, Di Xiao, and Q. Niu. "Valley-dependent optoelectronics from inversion symmetry breaking". In: *Phys. Rev. B* 77.23 (2008), p. 235406.

[81] H. Zeng, J. Dai, W. Yao, Di Xiao, and X. Cui. "Valley polarization in MoS_2 monolayers by optical pumping". In: *Nat. Nanotechnol.* 7.8 (2012), pp. 490–493.

[82] Y. Li, A. Chernikov, X. Zhang, A. Rigosi, H. M. Hill, A. M. van der Zande, D. A. Chenet, E.-M. Shih, J. Hone, and T. F. Heinz. "Measurement of the optical dielectric function of monolayer transition-metal dichalcogenides: MoS_2, $MoSe_2$, WS_2, and WSe_2". In: *Phys. Rev. B* 90.20 (2014), p. 205422.

[83] M. Bernardi, M. Palummo, and J. C. Grossman. "Extraordinary Sunlight Absorption and One Nanometer Thick Photovoltaics Using Two-Dimensional Monolayer Materials". In: *Nano Lett.* 13.8 (2013), pp. 3664–3670.

[84] K. F. Mak, K. He, C. Lee, G. H. Lee, J. Hone, T. F. Heinz, and J. Shan. "Tightly bound trions in monolayer MoS_2". In: *Nat. Mater.* 12.3 (2013), pp. 207–211.

[85] A. Steinhoff, M. Florian, A. Singh, K. Tran, M. Kolarczik, S. Helmrich, A. W. Achtstein, U. Woggon, N. Owschimikow, F. Jahnke, and X. Li. "Biexciton fine structure in monolayer transition metal dichalcogenides". In: *Nat. Phys.* 14.12 (2018), pp. 1199–1204.

[86] P. Nagler, G. Plechinger, M. V. Ballottin, A. Mitioglu, S. Meier, N. Paradiso, C. Strunk, A. Chernikov, P. C. M. Christianen, C. Schüller, and T. Korn. "Interlayer exciton dynamics in a dichalcogenide monolayer heterostructure". In: *2D Mater.* 4.2 (2017), p. 025112.

[87] N. Kumar, Q. Cui, F. Ceballos, D. He, Y. Wang, and H. Zhao. "Exciton-exciton annihilation in MoSe 2 monolayers". In: *Physical Review B* 89.12 (2014).

[88] S. Bae, T. Y. Jeong, H. Raebiger, K.-J. Yee, and Y.-H. Kim. "Localized coherent phonon generation in monolayer MoSe 2 from ultrafast exciton trapping at shallow traps". In: *Nanoscale Horizons* 8.9 (2023), pp. 1282–1287.

[89] C. Ruppert, A. Chernikov, H. M. Hill, A. F. Rigosi, and T. F. Heinz. "The Role of Electronic and Phononic Excitation in the Optical Response of Monolayer WS2 after Ultrafast Excitation". In: *Nano Letters* 17.2 (2017), pp. 644–651.

[90] E. A. A. Pogna, M. Marsili, D. de Fazio, S. Dal Conte, C. Manzoni, D. Sangalli, D. Yoon, A. Lombardo, A. C. Ferrari, A. Marini, G. Cerullo, and D. Prezzi. "Photo-Induced Bandgap Renormalization Governs the Ultrafast Response of Single-Layer MoS_2". In: *ACS nano* 10.1 (2016), pp. 1182–1188.

[91] K. Chen, R. Ghosh, X. Meng, A. Roy, J.-S. Kim, F. He, S. C. Mason, X. Xu, J.-F. Lin, D. Akinwande, S. K. Banerjee, and Y. Wang. "Experimental evidence of exciton capture by mid-gap defects in CVD grown monolayer MoSe2". In: *npj 2D Materials and Applications* 1.1 (2017).

[92] T. Hellerer. "CARS-Mikroskopie: Entwicklung und Anwendung". Doctoral dissertation. München: Ludwig-Maximilians-Universität München, 2004.

[93] A. Biewald, N. Giesbrecht, T. Bein, P. Docampo, A. Hartschuh, and R. Ciesielski. "Temperature-Dependent Ambipolar Charge Carrier Mobility in Large-Crystal Hybrid Halide Perovskite Thin Films". In: *ACS Appl. Mater. Interfaces* 11.23 (2019), pp. 20838–20844.

[94] G. McConnell, W. Amos, and T. Wilson. "Confocal microscopy". In: *Comprehensive Biophysics*. Ed. by E. H. Egelman. Amsterdam: Elsevier, 2012.

[95] N. Naredi-Rainer, J. Prescher, A. Hartschuh, and D. C. Lamb. "Confocal Microscopy". In: *Fluorescence microscopy*. Ed. by U. Kubitscheck. Weinheim: Wiley-Blackwell, 2013, pp. 175–213.

[96] C. Daly, A. McGee, E. Vila, A. Briones, J. Giraldo, S. Arribas, C. González, J. M. González, B. Somoza, S. N. Pagakis, et al. "Analysing the 3D structure of blood vessels using confocal microscopy". In: *Microscopy and Analysis* (2002), pp. 5–10.

[97] W. Becker. *Advanced Time-Correlated Single Photon Counting Techniques*. Vol. 81. Springer series in chemical physics. Berlin: Springer, 2005.

[98] D. V. O'Connor and D. Phillips. *Time-correlated Single Photon Counting*. London: Academic Press Inc., 1984.

[99] K. Lindfors, T. Kalkbrenner, P. Stoller, and V. Sandoghdar. "Detection and Spectroscopy of Gold Nanoparticles Using Supercontinuum White Light Confocal Microscopy". In: *Phys. Rev. Lett.* 93.3 (2004), p. 037401.

[100] J. Ortega Arroyo, J. Andrecka, K. M. Spillane, N. Billington, Y. Takagi, J. R. Sellers, and P. Kukura. "Label-Free, All-Optical Detection, Imaging, and Tracking of a Single Protein". In: *Nano Lett.* 14.4 (2014), pp. 2065–2070.

[101] Y.-H. Lin, W.-L. Chang, and C.-L. Hsieh. "Shot-noise limited localization of single 20 nm gold particles with nanometer spatial precision within microseconds". In: *Opt. Express* 22.8 (2014), pp. 9159–9170.

[102] J. Ortega Arroyo, D. Cole, and P. Kukura. "Interferometric scattering microscopy and its combination with single-molecule fluorescence imaging". In: *Nat. Protoc.* 11.4 (2016), pp. 617–633.

[103] R. W. Taylor and V. Sandoghdar. "Interferometric Scattering (iSCAT) Microscopy and Related Techniques". In: *Label-Free Super-Resolution Microscopy*. Ed. by V. Astratov. Cham: Springer International Publishing, 2019, pp. 25–65.

[104] J. Hwang and W. E. Moerner. "Interferometry of a single nanoparticle using the Gouy phase of a focused laser beam". In: *Opt. Commun.* 280.2 (2007), pp. 487–491.

[105] C. F. Bohren and D. R. Huffman. *Absorption and Scattering of Light by Small Particles*. Wiley science paperback series. Weinheim: Wiley-VCH, 2004.

[106] R. W. Taylor and V. Sandoghdar. "Interferometric Scattering Microscopy: Seeing Single Nanoparticles and Molecules via Rayleigh Scattering". In: *Nano Lett.* 19.8 (2019), pp. 4827–4835.

[107] Y. Li and T. F. Heinz. "Two-dimensional models for the optical response of thin films". In: *2D Materials* 5.2 (2018), p. 025021.

[108] A. Das and M. Pradhan. "Exploring the optical beam shifts in monolayers of transition metal dichalcogenides using Gaussian beams". In: *Optics Communications* 437 (2019), pp. 312–320.

[109] R. Berera, R. van Grondelle, and J. T. M. Kennis. "Ultrafast transient absorption spectroscopy: principles and application to photosynthetic systems". In: *Photosynth. Res.* 101.2-3 (2009), pp. 105–118.

[110] D. Davydova, A. de La Cadena, D. Akimov, and B. Dietzek. "Transient absorption microscopy: advances in chemical imaging of photoinduced dynamics". In: *Laser Photonics Rev.* 10.1 (2016), pp. 62–81.

[111] C. Zhu, Y. Liu, J. Xu, Z. Nie, Y. Li, Y. Xu, R. Zhang, and F. Wang. "Bandgap renormalization in single-wall carbon nanotubes". In: *Scientific reports* 7.1 (2017), p. 11221.

[112] P. Nikolaev, M. J. Bronikowski, R. Bradley, F. Rohmund, D. T. Colbert, K. Smith, and R. E. Smalley. "Gas-phase catalytic growth of single-walled carbon nanotubes from carbon monoxide". In: *Chem. Phys. Lett.* 313.1-2 (1999), pp. 91–97.

[113] A. Kukovecz, C. Kramberger, V. Georgakilas, M. Prato, and H. Kuzmany. "A detailed Raman study on thin single-wall carbon nanotubes prepared by the HiPCO process". In: *Eur. Phys. J. B* 28.2 (2002), pp. 223–230.

[114] N. K. Subbaiyan, S. Cambré, A. N. G. Parra-Vasquez, E. H. Hároz, S. K. Doorn, and J. G. Duque. "Role of Surfactants and Salt in Aqueous Two-Phase Separation of Carbon Nanotubes toward Simple Chirality Isolation". In: *ACS nano* 8.2 (2014), pp. 1619–1628.

[115] A. Jain, P. Bharadwaj, S. Heeg, M. Parzefall, T. Taniguchi, K. Watanabe, and L. Novotny. "Minimizing residues and strain in 2D materials transferred from PDMS". In: *Nanotechnology* 29.26 (2018), p. 265203.

[116] Z. Guo, J. S. Manser, Y. Wan, P. V. Kamat, and L. Huang. "Spatial and temporal imaging of long-range charge transport in perovskite thin films by ultrafast microscopy". In: *Nat. Commun.* 6.1 (2015), p. 7471.

[117] Y. Bai, J.-H. Olivier, G. Bullard, C. Liu, and M. J. Therien. "Dynamics of charged excitons in electronically and morphologically homogeneous single-walled carbon nanotubes". In: *Proc. Natl. Acad. Sci. U.S.A.* 115.4 (2018), pp. 674–679.

[118] G. Soavi, F. Scotognella, D. Brida, T. Hefner, F. Späth, M. R. Antognazza, T. Hertel, G. Lanzani, and G. Cerullo. "Ultrafast Charge Photogeneration in Semiconducting Carbon Nanotubes". In: *J. Phys. Chem. C* 117.20 (2013), pp. 10849–10855.

[119] E. R. Andresen, V. Birkedal, J. Thøgersen, and S. R. Keiding. "Tunable light source for coherent anti-Stokes Raman scattering microspectroscopy based on the soliton self-frequency shift". In: *Opt. Lett.* 31.9 (2006), pp. 1328–1330.

[120] B. Li, C. Wu, M. Wang, K. Charan, and C. Xu. "An adaptive excitation source for high-speed multiphoton microscopy". In: *Nat. Methods* 17.2 (2020), pp. 163–166.

[121] W. Becker, A. Bergmann, A. Jelzow, A. Neubauer, A. C. Rueck, K. Birkmeier, and P. Leisching. "Metabolic imaging by simultaneous 2-photon FLIM of NAD(P)H and FAD". In: *Multiphoton Microscopy in the Biomedical Sciences XX*. Ed. by A. Periasamy, P. T. So, and K. König. Progress in biomedical optics and imaging. Bellingham, Washington: SPIE, 2020, p. 20.

[122] Lee, Jennifer H. and van Howe, James and Xu, Chris and Liu, Xiang. "Soliton Self-Frequency Shift: Experimental Demonstrations and Applications". In: *IEEE J. Sel. Top. Quantum Electron.* 14.3 (2008), pp. 713–723.

[123] W. Zinth and U. Zinth. *Optik: Lichtstrahlen - Wellen - Photonen*. 3rd ed. München: Oldenbourg, 2011.

[124] B. Yang, J. Duan, Z. Xie, and H. Xiao. "Evaluation of Mode Field Diameter of Step-Index Fibers and Comparison Analysis". In: *Res. J. Appl. Sci.* 6.3 (2013), pp. 382–386.

[125] D. Marcuse. "Interdependence of waveguide and material dispersion". In: *Appl. Opt.* 18.17 (1979), pp. 2930–2932.

[126] Y. Yamamoto, Y. Tamura, and T. Hasegawa. "Silica-Based Highly Nonlinear Fibers and Their Applications". In: *SEI Tech. Rev.* 83 (2016), pp. 15–20.

[127] F. M. Cox, A. Argyros, and M. C. J. Large. "Liquid-filled hollow core microstructured polymer optical fiber". In: *Opt. Express* 14.9 (2006), pp. 4135–4140.

[128] K. O. Hill, F. Bilodeau, B. Malo, T. Kitagawa, S. Thériault, D. C. Johnson, J. Albert, and K. Takiguchi. "Chirped in-fiber Bragg gratings for compensation of optical-fiber dispersion". In: *Opt. Lett.* 19.17 (1994), pp. 1314–1316.

[129] R. W. Boyd. *Nonlinear Optics*. 3rd ed. USA: Academic Press, Inc., 2008.

[130] P. A. Franken, A. E. Hill, C. W. Peters, and G. Weinreich. "Generation of Optical Harmonics". In: *Phys. Rev. Lett.* 7.4 (1961), pp. 118–119.

[131] E. Constant and E. Mével. "Attosecond Pulses". In: *Femtosecond laser pulses*. Ed. by C. Rullière. Advanced texts in physics. New York: Springer, 2005, pp. 395–422.

[132] G. P. Agrawal. *Nonlinear Fiber Optics*. 3rd ed. Optics and photonics. San Diego: Academic Press, 2001.

[133] D. Marcuse. "Pulse distortion in single-mode fibers". In: *Appl. Opt.* 19.10 (1980), pp. 1653–1660.

[134] J. S. Russell. *Report on Waves: Made to the Meetings of the British Association in 1842-43*. 1845.

[135] A. Shabat and V. Zakharov. "Exact theory of two-dimensional self-focusing and one-dimensional self-modulation of waves in nonlinear media". In: *J. Exp. Theor. Phys.* 34.1 (1972), pp. 62–69.

[136] T. R. Taha and M. J. Ablowitz. "Analytical and numerical aspects of certain nonlinear evolution equations. II. Numerical, nonlinear Schrödinger equation". In: *Journal of Computational Physics* 55.2 (1984), pp. 203–230.

[137] P. Kabaciński, T. M. Kardaś, Y. Stepanenko, and C. Radzewicz. "Nonlinear refractive index measurement by SPM-induced phase regression". In: *Opt. Express* 27.8 (2019), pp. 11018–11028.

[138] M. Klaus and J. K. Shaw. "Influence of pulse shape and frequency chirp on stability of optical solitons". In: *Opt. Commun.* 197.4-6 (2001), pp. 491–500.

[139] G. P. Agrawal. "Nonlinear Fiber Optics". In: *Nonlinear Science at the Dawn of the 21st Century*. Ed. by P. L. Christiansen, M. P. Sorensen, and A. C. Scott. Lecture notes in physics. Berlin, Heidelberg: Springer Berlin Heidelberg, 2000, pp. 195–211.

[140] F. M. Mitschke and L. F. Mollenauer. "Discovery of the soliton self-frequency shift". In: *Opt. Lett.* 11.10 (1986), pp. 659–661.

[141] G. P. Agrawal. “Fiber Optic Raman Amplifiers”. In: *Guided Wave Optical Components and Devices*. Ed. by B. P. Pal. Burlington: Elsevier Acad. Press, 2006, pp. 131–153.

[142] J. P. Gordon. “Theory of the soliton self-frequency shift”. In: *Opt. Lett.* 11.10 (1986), pp. 662–664.

[143] X. Audier, S. Heuke, P. Volz, I. Rimke, and H. Rigneault. “Noise in stimulated Raman scattering measurement: From basics to practice”. In: *APL Photonics* 5.1 (2020), p. 011101.

[144] X. Cheng, W. Pan, X. Zeng, J. Dong, S. Cui, and Y. Feng. “Relative intensity noise comparison of fiber laser and amplified spontaneous emission sources”. In: *Opt. Fiber Technol.* 54 (2020), p. 102119.

[145] K. Wu, J. H. Wong, P. Shum, S. Fu, C. Ouyang, H. Wang, E. J. R. Kelleher, A. I. Chernov, E. D. Obraztsova, and J. Chen. “Nonlinear coupling of relative intensity noise from pump to a fiber ring laser mode-locked with carbon nanotubes”. In: *Opt. Express* 18.16 (2010), pp. 16663–16670.

[146] B. Gouhier, S. Rota-Rodrigo, G. Guiraud, N. Traynor, and G. Santarelli. “Low-noise single-frequency 50 W fiber laser operating at 1013 nm”. In: *Laser Phys. Lett.* 16.4 (2019), p. 045103.

[147] S. Foster. “Fundamental limits on 1/f frequency noise in rare-earth-metal-doped fiber lasers due to spontaneous emission”. In: *Phys. Rev. A* 78.1 (2008), p. 013820.

[148] S. M. Vaezi-Nejad, M. Cox, and N. Cooper. “Novel instrumentation for measurement of relative intensity noise”. In: *Trans. Inst. Meas. Control* 34.4 (2012), pp. 477–486.

[149] U. Masud, M. Ali, and M. Ikram. “Calibration and stability of highly sensitive fibre based laser through relative intensity noise”. In: *Phys. Scr.* 95.5 (2020), p. 055505.

[150] U. Keller, K. J. Weingarten, F. X. Kartner, D. Kopf, B. Braun, I. D. Jung, R. Fluck, C. Honninger, N. Matuschek, and J. aus der Au. “Semiconductor saturable absorber mirrors (SESAM’s) for femtosecond to nanosecond pulse generation in solid-state lasers”. In: *IEEE J. Sel. Top. Quantum Electron.* 2.3 (1996), pp. 435–453.

[151] K. Birkmeier and A. Hartschuh. “Wavelength-Tunable Ultrafast Two Arm Fiber Laser System for Transient Interferometric Scattering Microscopy on Nanoscopic Objects”. In: *J. Opt. Soc. Am. B* 41.2 (2024), pp. 493–499.

[152] D. Strickland and G. Mourou. "Compression of Amplified Chirped Optical Pulses". In: *Opt. Commun.* 55.6 (1985), pp. 447–449.

[153] *The Nobel Price in Physics 2018: Nobel Prize Outreach AB 2021.* URL: `https://www.nobelprize.org/prizes/physics/2018/summary/`.

[154] M. Pessot, P. Maine, and G. Mourou. "1000 Times Expansion/Compression of Optical Pulses for Chirped Pulse Amplification". In: *Opt. Commun.* 62.6 (1987), pp. 419–421.

[155] I. Walmsley, L. Waxer, and C. Dorrer. "The role of dispersion in ultrafast optics". In: *Rev. Sci. Instrum.* 72.1 (2001), pp. 1–29.

[156] J. Extermann, P. Béjot, L. Bonacina, Y. Mugnier, R. Le Dantec, T. Mazingue, C. Galez, and J.-P. Wolf. "An inexpensive nonlinear medium for intense ultrabroadband pulse characterization". In: *Appl. Phys. B* 97.3 (2009), pp. 537–540.

[157] S. Vinga and J. S. Almeida. "Rényi continuous entropy of DNA sequences". In: *Journal of theoretical biology* 231.3 (2004), pp. 377–388.

[158] B. Li, M. Wang, K. Charan, M.-J. Li, and C. Xu. "Investigation of the long wavelength limit of soliton self-frequency shift in a silica fiber". In: *Opt. Express* 26.15 (2018), pp. 19637–19647.

[159] R. Herda. *SSFTProp: Pulse propagation simulation software developed at TOPTICA Photonics AG.* 2019.

[160] K. Birkmeier, T. Hertel, and A. Hartschuh. "Probing the ultrafast dynamics of excitons in single semiconducting carbon nanotubes". In: *Nature communications* 13.1 (2022), pp. 1–8.

[161] B. Gao, G. V. Hartland, and L. Huang. "Transient Absorption Spectroscopy and Imaging of Individual Chirality-Assigned Single-Walled Carbon Nanotubes". In: *ACS nano* 6.6 (2012), pp. 5083–5090.

[162] H. Ozawa, N. Ide, T. Fujigaya, Y. Niidome, and N. Nakashima. "One-pot Separation of Highly Enriched (6,5)-Single-walled Carbon Nanotubes Using a Fluorene-based Copolymer". In: *Chem. Lett.* 40.3 (2011), pp. 239–241.

[163] C. Georgi, A. A. Green, M. C. Hersam, and A. Hartschuh. "Probing Exciton Localization in Single-Walled Carbon Nanotubes Using High-Resolution Near-Field Microscopy". In: *ACS nano* 4.10 (2010), pp. 5914–5920.

[164] J. J. Crochet, J. G. Duque, J. H. Werner, B. Lounis, L. Cognet, and S. K. Doorn. "Disorder Limited Exciton Transport in Colloidal Single-Wall Carbon Nanotubes". In: *Nano Lett.* 12.10 (2012), pp. 5091–5096.

[165] L. Piatkowski, N. Accanto, G. Calbris, S. Christodoulou, I. Moreels, and N. F. van Hulst. "Ultrafast stimulated emission microscopy of single nanocrystals". In: *Science* 366.6470 (2019), pp. 1240–1243.

[166] M. Liebel, C. Toninelli, and N. F. van Hulst. "Room-temperature ultrafast nonlinear spectroscopy of a single molecule". In: *Nat. Photonics* 12.1 (2018), pp. 45–49.

[167] W. Zhou, D. Nakamura, H. Liu, H. Kataura, and S. Takeyama. "Relative ordering between bright and dark excitons in single-walled carbon nanotubes". In: *Scientific reports* (2014), p. 6999.

[168] J. G. Duque, M. Pasquali, L. Cognet, and B. Lounis. "Environmental and Synthesis-Dependent Luminescence Properties of Individual Single-Walled Carbon Nanotubes". In: *ACS nano* 3.8 (2009), pp. 2153–2156.

[169] C. Mann and T. Hertel. "13 nm Exciton Size in (6,5) Single-Wall Carbon Nanotubes". In: *J. Phys. Chem. Lett.* 7.12 (2016), pp. 2276–2280.

[170] L. Huang, G. V. Hartland, L.-Q. Chu, Luxmi, R. M. Feenstra, C. Lian, K. Tahy, and H. Xing. "Ultrafast transient absorption microscopy studies of carrier dynamics in epitaxial graphene". In: *Nano Letters* 10.4 (2010), pp. 1308–1313.

[171] J. Allam, M. T. Sajjad, R. Sutton, K. Litvinenko, Z. Wang, S. Siddique, Q.-H. Yang, W. H. Loh, and T. Brown. "Measurement of a reaction-diffusion crossover in exciton-exciton recombination inside carbon nanotubes using femtosecond optical absorption". In: *Phys. Rev. Lett.* 111.19 (2013), p. 197401.

[172] L. Oudjedi, A. N. G. Parra-Vasquez, A. G. Godin, L. Cognet, and B. Lounis. "Metrological Investigation of the (6,5) Carbon Nanotube Absorption Cross Section". In: *J. Phys. Chem. Lett.* 4.9 (2013), pp. 1460–1464.

[173] L. Cognet, D. A. Tsyboulski, J.-D. R. Rocha, C. D. Doyle, J. M. Tour, and R. B. Weisman. "Stepwise quenching of exciton fluorescence in carbon nanotubes by single-molecule reactions". In: *Science* 316.5830 (2007), pp. 1465–1468.

[174] H. Qian, P. T. Araujo, C. Georgi, T. Gokus, N. Hartmann, A. A. Green, A. Jorio, M. C. Hersam, L. Novotny, and A. Hartschuh. "Visualizing the Local Optical Response of Semiconducting Carbon Nanotubes to DNA-Wrapping". In: *Nano Lett.* 8.9 (2008), pp. 2706–2711.

[175] G. E. Uhlenbeck and L. S. Ornstein. "On the Theory of the Brownian Motion". In: *Phys. Rev.* 36.5 (1930), pp. 823–841.

[176] R. B. Capaz, C. D. Spataru, S. Ismail-Beigi, and S. G. Louie. "Diameter and chirality dependence of exciton properties in carbon nanotubes". In: *Phys. Rev. B* 74.12 (2006).

[177] A. Kumar and P. K. Ahluwalia. "Electronic structure of transition metal dichalcogenides monolayers 1H-MX_2 (M = Mo, W; X = S, Se, Te) from ab-initio theory: new direct band gap semiconductors". In: *Eur. Phys. J. B* 85.6 (2012).

[178] P. Wang, M. N. Slipchenko, J. Mitchell, C. Yang, E. O. Potma, X. Xu, and J.-X. Cheng. "Far-field Imaging of Non-fluorescent Species with Sub-diffraction Resolution". In: *Nat. Photonics* 7.6 (2013), pp. 449–453.

[179] P. Valencia-Acuna, P. Zereshki, M. M. Tavakoli, J.-H. Park, J. Kong, and H. Zhao. "Transient absorption of transition metal dichalcogenide monolayers studied by a photodope-pump-probe technique". In: *Phys. Rev. B* 102.3 (2020).

[180] Z. Nie, C. Trovatello, E. A. A. Pogna, S. Dal Conte, P. B. Miranda, E. Kelleher, C. Zhu, I. C. E. Turcu, Y. Xu, K. Liu, G. Cerullo, and F. Wang. "Broadband nonlinear optical response of monolayer $MoSe_2$ under ultrafast excitation". In: *Appl. Phys. Lett.* 112.3 (2018), p. 031108.

[181] A. Chernikov, A. M. van der Zande, H. M. Hill, A. F. Rigosi, A. Velauthapillai, J. Hone, and T. F. Heinz. "Electrical Tuning of Exciton Binding Energies in Monolayer WS_2". In: *Phys. Rev. Lett.* 115.12 (2015), p. 126802.

[182] T. Jiang, R. Chen, X. Zheng, Z. Xu, and Y. Tang. "Photo-induced excitonic structure renormalization and broadband absorption in monolayer tungsten disulphide". In: *Opt. Express* 26.2 (2018), pp. 859–869.

[183] C. Trovatello, H. P. C. Miranda, A. Molina-Sánchez, R. Borrego-Varillas, C. Manzoni, L. Moretti, L. Ganzer, M. Maiuri, J. Wang, D. Dumcenco, A. Kis, L. Wirtz, A. Marini, G. Soavi, A. C. Ferrari, G. Cerullo, D. Sangalli, and S. D. Conte. "Strongly Coupled Coherent Phonons in Single-Layer MoS2". In: *ACS nano* 14.5 (2020), pp. 5700–5710.

[184] J. Ye, T. Yan, B. Niu, Y. Li, and X. Zhang. "Nonlinear dynamics of trions under strong optical excitation in monolayer MoSe2". In: *Scientific reports* 8.1 (2018), p. 2389.

[185] C. Bentz, L. Baudzus, and P. Krummrich. "Signal to Noise Ratio (SNR) Enhancement Comparison of Impulse-, Coding- and Novel Linear-Frequency-Chirp-Based Optical Time Domain Reflectometry (OTDR) for Passive Optical Network (PON) Monitoring Based on Unique Combinations of Wavelength Selective Mirrors". In: *Photonics* 1.1 (2014), pp. 33–46.

[186] B. Gao, G. V. Hartland, and L. Huang. "Transient Absorption Spectroscopy of Excitons in an Individual Suspended Metallic Carbon Nanotube". In: *J. Phys. Chem. Lett.* 4.18 (2013), pp. 3050–3055.

[187] T. Hayashi, Y. A. Kim, T. Matoba, M. Esaka, K. Nishimura, T. Tsukada, M. Endo, and M. S. Dresselhaus. "Smallest Freestanding Single-Walled Carbon Nanotube". In: *Nano Lett.* 3.7 (2003), pp. 887–889.

[188] A. C. Torres-Dias, T. F. Cerqueira, W. Cui, M. A. Marques, S. Botti, D. Machon, M. A. Hartmann, Y. Sun, D. J. Dunstan, and A. San-Miguel. "From mesoscale to nanoscale mechanics in single-wall carbon nanotubes". In: *Carbon* 123 (2017), pp. 145–150.

[189] K. Liu, X. Hong, S. Choi, C. Jin, R. B. Capaz, J. Kim, W. Wang, X. Bai, S. G. Louie, E. Wang, and F. Wang. "Systematic determination of absolute absorption cross-section of individual carbon nanotubes". In: *Proc. Natl. Acad. Sci. U.S.A.* 111.21 (2014), pp. 7564–7569.

[190] H. Harutyunyan, T. Gokus, A. A. Green, M. C. Hersam, M. Allegrini, and A. Hartschuh. "Defect-Induced Photoluminescence from Dark Excitonic States in Individual Single-Walled Carbon Nanotubes". In: *Nano Lett.* 9.5 (2009), pp. 2010–2014.

[191] M. Schweiger, Y. Zakharko, F. Gannott, S. B. Grimm, and J. Zaumseil. "Photoluminescence enhancement of aligned arrays of single-walled carbon nanotubes by polymer transfer". In: *Nanoscale* 7.40 (2015), pp. 16715–16720.

[192] W. Demtröder. *Molekülphysik: Theoretische Grundlagen und experimentelle Methoden*. 2nd ed. München: Oldenbourg, 2012.

[193] S. Berciaud, L. Cognet, P. Poulin, R. B. Weisman, and B. Lounis. "Absorption Spectroscopy of Individual Single-Walled Carbon Nanotubes". In: *Nano Lett.* 7.5 (2007), pp. 1203–1207.

[194] J. Mu, Y. Ma, H. Yin, C. Liu, and M. Rohlfing. "Photoluminescence of Single-Walled Carbon Nanotubes: The Role of Stokes Shift and Impurity Levels". In: *Phys. Rev. Lett.* 111.13 (2013), p. 137401.

List of Abbreviations

AOM	acousto-optic modulator
APD	avalanche photodiode
ATP	aqueous two-phase separation
AU	Airy unit
BGR	band gap renormalization
BZ	Brillouin zone
CARS	coherent anti-Stokes Raman scattering
CNT	carbon nanotube
CPA	chirped pulse amplification
CVD	chemical vapour deposition
DC	direct current
DFG	difference frequency generation
DNA	deoxyribonucleic acid
DOC	sodium deoxycholate
DOS	density of states
EEA	exciton-exciton annihilation
FRET	Förster resonance energy transfer
FWHM	full width at half maximum
GDD	group delay dispersion

GSB ground state bleaching

GVD group velocity dispersion

HiPCO high-pressure catalytic decomposition of CO

HNLF highly nonlinear fiber

IAC interferometric autocorrelation

IR infra-red

IRF instrument response function

iSCAT interferometric scattering

LIA lock-in amplifier

MFD mode field diameter

MPD multiphonon decay

MSD mean square displacement

NA numerical aperture

NSE nonlinear Schrödinger equation

OPA optical parametric amplifier

OPO optical parametric oscillator

OR optical rectification

PA photoinduced absorption

PAIEI phonon-assisted indirect exciton ionization

PB photoinduced bleaching

PD photodiode

PFO-BPy 9,9-dioctylfluorenyl-2,7-diyl (PFO) and bipyridine (BPy)

PL photoluminescence

PM polarization maintaining

PPLN periodically-poled lithium niobate

PSD power spectral density

PSF point-spread function

QPM quasi phase matching

QY quantum yield

RIN relative intensity noise

rms root-mean-square

SAM saturable absorber mirror

SC supercontinuum

SC sodium cholate

SDS sodium dodecylsulfate

SESAM semiconducting saturable absorber mirror

SHG second harmonic generation

SM single mode

SNR signal-to-noise ratio

SPM self-phase modulation

SRS stimulated Raman scattering

SSFS soliton self-frequency shift

STE stimulated emission

SWCNT single-walled carbon nanotube

TA transient absorption

TCSPC time correlated single photon counting

TE transverse electric

TEM transverse electromagnetic mode

THG third harmonic generation

Ti:Sa titanium:sapphire

TiSCAT transient interferometric scattering

TMDC transition-metal dichalcogenide

vHs van-Hove singularity

List of Figures

List of Publications

During the course of my PhD research, the following peer-reviewed papers have been published or are accepted for publication:

- K. Birkmeier, T. Hertel, and A. Hartschuh. “Probing the ultrafast dynamics of excitons in single semiconducting carbon nanotubes”. In: Nature communications 13.1 (2022), pp. 1–8.
- K. Birkmeier, A. Hartschuh. “Wavelength-Tunable Ultrafast Two Arm Fiber Laser System for Transient Interferometric Scattering Microscopy on Nanoscopic Objects”. In: Journal of the Optical Society of America B 41.2 (2024), pp 493-499.

The following conference contributions have been published:

- K. Birkmeier, A. Brodschelm, F. Tauser, R. Häring, B. Wolfring, and A. Hartschuh. “Transient interferometric scattering microscopy on nanoscale objects with high sensitivity”. In: Nanoscale and Quantum Materials: From Synthesis and Laser Processing to Applications 2023 (2023), pp. 46-51.
- K. Birkmeier, A. Brodschelm, and A. Hartschuh. “Frequency-Tunable Two-Colour Ultrafast Fiber Laser for Nonlinear Microscopy in the Fingerprint Regime Emitting at Central Frequencies 780 nm and 810 nm to 950 nm”. In: 2019 Conference on Lasers and Electro-Optics Europe & European Quantum Electronics Conference (CLEO/Europe-EQEC) (2019), pp. 1-1.

Acknowledgement

In the last years I had the great pleasure to work with many nice people who made this time really enjoyable.
In particular, I want to thank:
Prof. Achim Hartschuh for the opportunity to do my research in his group and his willingness for this kind of special PhD study which was carried out half in a company.
Prof. Alexander Högele for his support as being the second reviewer of my thesis.
The colleagues in my group at the university while I did my research there: **Veit Giegold, Angelika Jahn, Lucas Lange, Alexander Biewald, Rachid Houssaini, Meltem Aygüler and David Tóth**. Working with you was always a pleasure and I enjoyed the time at the university very much.
All people at TOPTICA photonics AG who supported me in the last years and gave me the opportunity to do my research at the university and let me develop the laser perfectly suited for my experiments.
Special thanks goes the present and former people of the TOPTICA fiber laser group: **Christoph Skrobol, Andreas Brodschelm, Robert Herda, Axel Friedenauer, Fabian Röser, Alexei Ivanov, Lorena Renkl, Steffen Falkenstein**.
A special thanks to **Andreas Brodschelm** for being my supervisor at TOPTICA, his helpful advice and support throughout the whole time of my research and for introducing me to Git which saved me more than once while writing my thesis.
Christoph Skrobol for the support and covering by back so I was able to focus on my research.
The **Bundesministerium für Bildung und Forschung (BMBF)** for the financial support within the scope of the project OMOXI which paved the way for the fiber laser developed in this work.
My family and friends for their continual support and encouragement at any time.
And finally **Emi** for her tireless support, encouragement and patience, especially in the final part of my work. I am deeply grateful that we have met.